Inaugural Dissertation zur Erlangung des
Doktorgrades der Naturwissenschaften
der Justus-Liebig Universität Gießen
(Fachbereich Physik)

Unambiguous Identification and Investigation of Uranium Projectile Fragments.

&

Discovery of 63 New Neutron-rich Isotopes in the Element Range 61≤Z≤78 at the FRS

vorgelegt von
Fabio Farinon

Gießen, im October 2011

Gutachter: Prof Dr. Hans Geissel
Prof Dr. Volker Metag

Contents

Zusammenfassung **3**

1 Production, Separation and Identification of Exotic Nuclei **7**
1.1 The high energy rare isotope facility at GSI 7
1.2 Production of heavy neutron rich nuclei via projectile fragmentation 8
1.3 Spatial separation with the in-flight separator FRS 12
1.3.1 The particle identification detectors of FRS 14
1.4 Particle identification 21
1.4.1 Energy loss, energy deposition and Z determination 22
1.4.2 Time of flight measurement 30
1.4.3 Position measurement 31
1.4.4 A/q measurement 32
1.5 Detector setup for decay measurements 33
1.5.1 Germanium detectors 33
1.5.2 The Active Stopper 36

2 The New Isomer Tagging System **45**
2.1 Setup of ITAG 45
2.1.1 Construction 45
2.1.2 Electronics 47
2.2 Measurements with ITAG 49
2.2.1 Efficiency 49
2.2.2 Commissioning experiment 49

3 Discovery of 63 New Isotopes **55**
3.1 Experimental Setup 56

3.2 Identification of New Isotopes 58
3.3 Determination of the Production Cross-sections for the Discovered Isotopes 67

4 Investigation and Decay Measurements of Neutral and H-like ^{213}Fr Ions **75**
4.1 Experiment for half-life determination of α-decaying neutral atoms 77
4.1.1 Setup and measurements 79
4.1.2 Data analysis and results 79
4.2 Experiment for half-life determination of α-decaying H-like ions . 88
4.2.1 Setup and measurements 88
4.2.2 Data analysis and results 91

Summary **97**

Bibliography **101**

Acknowledgments **105**

Zusammenfassung

Experimente mit exotischen, kurzlebigen Kernen tragen zum besseren Verstndnis der starken Wechselwirkung und der Elementsynthese in den Sternen bei. Im astrophysikalischen r-Prozess werden sehr neutronen-reiche Kerne gebildet, die nur schwer oder noch gar nicht im Labor herzustellen sind. Um sehr neutronen-reiche Kerne im Labor erzeugen zu knnen, werden moderne leistungsstarke Beschleuniger und neuartige Experimentiertechniken gebraucht. Eine besondere Herausforderung ist die eindeutige Identifikation von sehr schweren neutronen-reichen neuen Kernen.

In dieser Arbeit wurde eine spezielle Implantationsapparatur entwickelt und eingesetzt, die eine eindeutige Identifikation der separierten Projektilfragmente aufgrund von bekannter Isomerenstrahlung erlaubt.

Diese Arbeit besteht aus verschiedenen Experimenten, die alle von einer Produktion von exotischen Kernen mit einem Uran-Projektilstrahl bei relativistischen Energien am FRS ausgehen.

Im ersten Teil wurden mit einem 1000 MeV/u ^{238}U Strahl (2×10^9 Ionen pro Beschleunigerpuls) in einem 1.6 g/cm^2 dicken Be Target am Eingang des FRS neutronen-reiche Kerne im Elementebereich oberhalb von 60 erzeugt. Der FRS wurde in einem achromatischen Modus mit 2 Energieabsorbern in den ersten beiden Fokalebenen betrieben. Es wurden dabei besondere Anstrengungen bei der Separation und Identifikation mit neuen Detektorsystemen gemacht. Die eindeutige Isotopen-Identifikation im Fluge mit wurde mit der neuentwickelten Isomeren-Implantationsmethode verifiziert. Insgesamt konnten mit diesem Experiment 63 neue Isotope im Elementebereich $61 \leq Z \leq 78$ entdeckt werden.

Als erste Eigenschaft dieser neuen Kernen wurde ihre Produktionsquerschnitte bestimmt. Dies ist nicht einfach, da trotz den hohen Energien die Projektilfrag-

mente noch einige gebundene Elektronen im Durchflug durch den FRS haben knnen. Ionen in verschiedenen Ladungszustnden erschweren die Interpretation der Z-Bestimmung und auch die Energieverlustmessung nach den dicken Absorbern. Erst die Anwendung von mehrfachen Separations- und Kollerationskriterien machten eine przise Reaktionsquerschnittsmessung mglich.

Ein weiterer Teil dieser Doktorarbeit beschftigte sich mit den Zerfallseigenschaften von reinen Alpha-Emittern im neutralen und wasserstoffhnlichen Zustand. Diese Messungen sind ebenfalls astrophysikalisch relevant, weil radioaktive Ionen auch in heissen stellaren Medien zerfallen und die Lebensdauer stark von der Anzahl der gebundenen Elektronen abhngen kann. Solche Untersuchungen sind erstmals im Labor durch die Kombination des FRS mit dem ESR mglich.

Zunchst wurde die Halbwertszeit von neutralen ^{213}Fr und ^{214}Ra Atomen am FRS gemessen. Die separierten Fragmente wurden in der letzten Fokalebene in einen ortsempfindlichen Halbleiterdetektor implantiert. Die volle Teilchenidentifikation und die zugehrige Ortskorrelation ermglichten eine saubere Aufnahme der zugehrigen Zerfallskurven. Die Ergebnisse fr die Halbwertszeiten waren in diesem Experiment fr neutrale ^{213}Fr Atome 34.03 ± 0.27 s und fr ^{214}Ra 2.441 ± 0.021 s. Das Experiment mit ^{213}Fr Atomen wurde unter vllig vernderten Bedingungen in Catania wiederholt, weil unser Ergebnis nicht mit den Resultaten in der Literatur bereinstimmte. Das Ergebnis in Catania fr die gemessene Halbwertszeit von ^{213}Fr Atomen war 34.126 ± 0.056 s welches ausgezeichnet mit dem GSI Experiment bereinstimmt.

Im zweiten Teil des Zerfallsexperimentes wurde die Halbwertszeit von gespeicherten wasserstoffhnlichen ^{213}Fr Ionen im ESR auf zwei Arten gemessen. Die wasserstoffhnlichen ^{213}Fr Ionen wurden vom FRS separiert und in den ESR bei etwa 400 MeV/u injiziert. Der Alpha-Zerfall wurde mit Schottky Spektrometrie fr viele und einzelne Teilchen gemessen. Der Vergleich der Resultate mit den entsprechenden Messungen mit neutralen Atomen zeigt, dass innerhalb der Messfehler kein Unterschied beobachtet wurde. Damit sind alte theoretische Vorhersagen von Erma [Erm57] klar widerlegt, diese sagten einen Unterschied von 40% voraus. Neuere Theorien [Pat08] erwarten einen Unterschied fr neutrale und Hhnliche ^{213}Fr Atome von etwa 0.35 %. Fr eine solch geringe Differenz ist das hier beschriebene Pilotexperiment mit gespeicherten Alpha-Emittern nicht aus-

gelegt gewesen. Erst mit weit hherer Statistik und Verbesserungen in der Datenaufnahme knnen signifikante Ergebnisse mit Fehlern im Promillebereich erzielt werden.

Chapter 1

Production, Separation and Identification of Exotic Nuclei

The experimental technique used for the production of exotic nuclei in the current work is the projectile fragmentation and fission of relativistic heavy projectiles. The experiments required the use of a heavy-ion accelerator to provide the relativistic primary beams combined with a high-resolution magnetic spectrometer with different detectors for identification and separation of projectile fragments produced in these reactions. The SIS18/FRS facility of the Gesellschaft für Schwerionenforschung (GSI) is one of the best suited for these kinds of experiments.

1.1 The high energy rare isotope facility at GSI

The GSI accelerator complex facility located in Darmstadt, Germany, is a leading facilities for relativistic heavy-ion nuclear research. A schematic view of the GSI accelerator system is shown in figure 1.1. It consists of the Universal Linear Accelerator (UNILAC) coupled to the heavy-ion synchrotron (SIS-18). The SIS18 can accelerate all ions from protons to uranium to a maximum magnetic rigidity of 18 Tm, which corresponds to an energy 4.5 GeV in the case of proton and 1 GeV per nucleon in the case of $^{238}U^{73+}$. The accelerated primary beam from SIS-18 is transported to the production target at the entrance of the Fragment Separator (FRS) [Gei92]. The FRS provides a spatial separation of the secondary fragments and can be combined with different experimental facilities, like the Experimental

Storage Ring (ESR) [Fra87, Gei97].

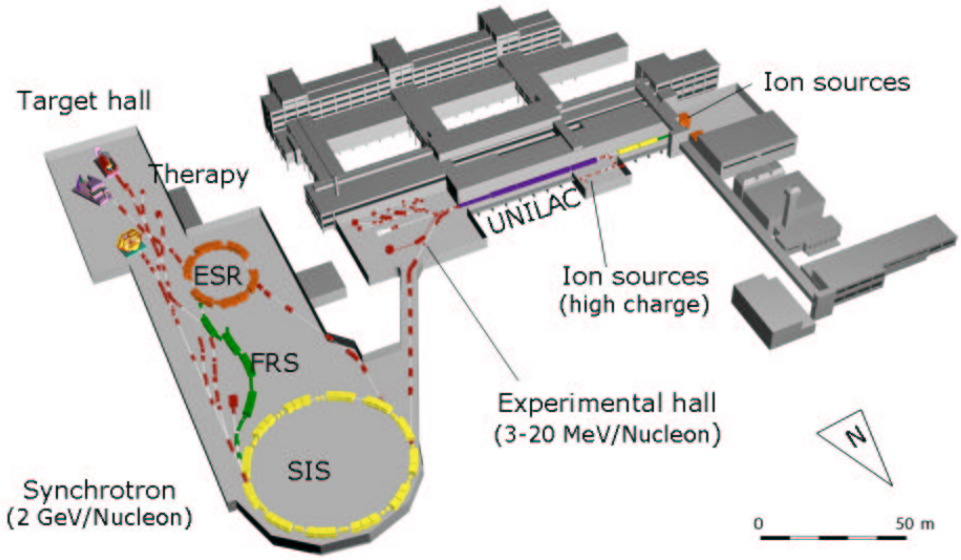

Figure 1.1: Schematic view of the GSI accelerator facility. The beam is accelerated in the UNILAC and then injected into the synchrotron SIS-18 for further acceleration to relativistic energies. At the entrance of the fragment separator (FRS) the primary beam interacts with the production target. The produced fragments are separated in flight with the FRS and the secondary beam of exotic ions can be delivered to the final focal planes of the FRS or to the experimental storage ring (ESR) or to the Target Hall.

1.2 Production of heavy neutron rich nuclei via projectile fragmentation

When heavy ions penetrate a target different reaction mechanisms can occur, depending on the beam velocity. The energy region below 20 A MeV is dominated by Coulomb scatterings, transfer reactions, and fusion evaporation. For high energies, however, the reactions are projectile and target fragmentation. The fragmentation process consists of two steps, which occur on two distinctly

different time scales. Fig. 1.2 shows a schematic view of the two-step process that is well described by the abrasion-ablation model [Gai91].

In the first step, which has a time scale of several 10^{-23} s, the beam collides with the target nuclei and abrades nucleons. These nucleons, called participants, belong to the geometrically overlapping zones between projectile and target nuclei. The nucleons outside of the interacting zone, called the spectators, continue their travel but gain an excitation energy that is in first approximation proportional to the number of abraded nucleons. This excitation energy stems from the excess of surface energy due to the shape change of the abraded fragment. In a second step, the ablation phase, the prefragment de-excites by evaporating neutrons, protons, or light particles or by fissioning, and finally by the emission of γ-rays. The characteristic time scale for the emission of particles varies between $\sim 10^{-16}$ s for an excitation energy of 10 MeV and $\sim 10^{-21}$ s at 200 MeV.

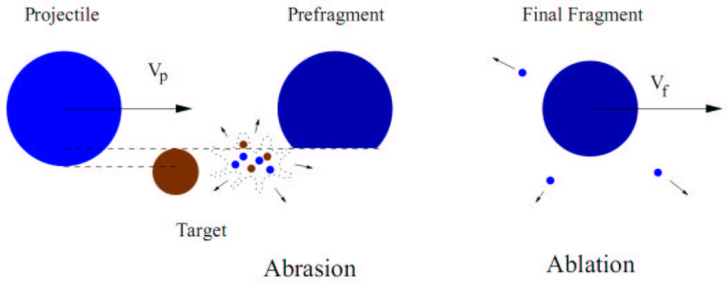

Figure 1.2: Schematic view of the projectile fragmentation mechanism. The peripheral reaction is a two-stage process where first nucleons are abraded (Abrasion) and secondly the exited pre-fragment emits nucleons (Ablation) before the final fragment is created.

With the fragmentation process a momentum spread is inevitably introduced. the root-mean-squared momentum of the fragments can be calculated using the approach by Goldhaber [Gol74], based on the Fermi momentum of the removed nucleons:

$$P_{rms} = P_{Fermi}\sqrt{\frac{3A_F(A_P - A_F)}{5(A_P - 1)}}. \tag{1.1}$$

In this equation A_P and A_F denote the mass of projectile and fragment, respectively and P_{Fermi} the Fermi momentum equal to 221 MeV/c. At high energies, an improvement of the Goldhaber formula is given by the semi-empirical formula

from Morrisey [Mor89] :

$$P_{rms} = 175\sqrt{A_P - A_F} \quad MeV/c. \tag{1.2}$$

For small mass difference ($\Delta A = A_P - A_F$), the two formulas give approximately the same result.

Along with the momentum spread goes a reduction of the longitudinal momentum $< P_{||} >$, which is proportional to ΔA and can calculated with [Mor89]:

$$< P_{||} >= 8\,\frac{A_F}{A_P}\,\frac{\gamma+1}{\beta\gamma}\,\Delta A \quad \frac{MeV}{c}, \tag{1.3}$$

where β and γ are considered in the laboratory frame.

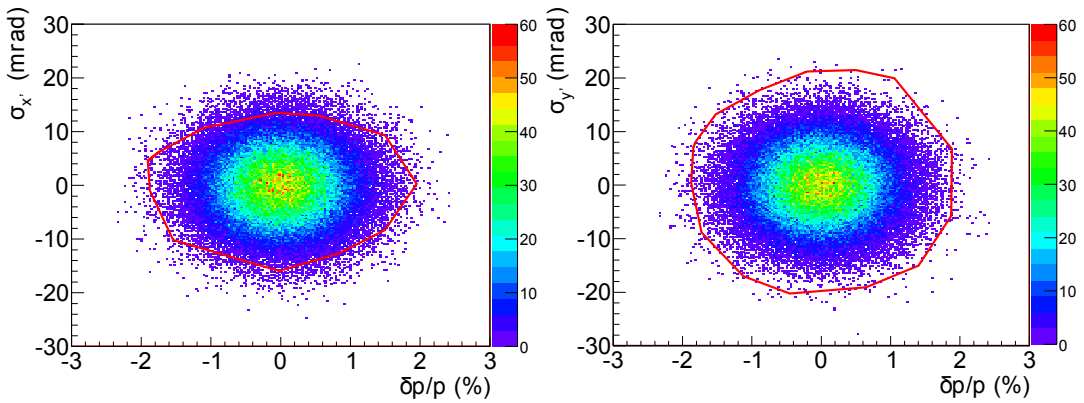

Figure 1.3: Calculated [Iwa97] phase-space distribution (transverse and longitudinal momentum distribution) of ^{213}Fr projectile fragments produced with a ^{238}U beam impinging on a Be target at 1000 MeV/u. $\sigma_{x'}$ and $\sigma_{y'}$ are the angular distributions of ^{213}Fr projectile fragments in the x and y direction respectively. The acceptance window of the FRS is approximated by the polygons.

The widening momentum due to the fragmentation reaction causes directly a broadening of the angular distribution:

$$\sigma_\alpha = \frac{P_{rms}}{\sqrt{3}\,P_F}, \tag{1.4}$$

where P_F is the momentum of the fragments in the laboratory frame. As a consequence of the angular straggling in the reaction, the fragments produced may not match the acceptance window of the FRS, therefore they are not transmitted to the final focal plane. Figure 1.3 show the calculated phase space distribution

(transverse and longitudinal momentum distribution) of ^{213}Fr projectile fragments produced with a ^{238}U beam impinging on a Be target at 1000 MeV/u. All the fragments outside the acceptance window of the FRS (shown approximated by a polygon), are not transmitted to the final focal plane.

For any given projectile target combination a vast number of different fragments is produced depending on the cross-section. An example of ^{238}U calculated production cross-section in the element range of 70 to 92 is given in Figure 1.4. The heavy ions of interest must be separated from the primary beam and un-

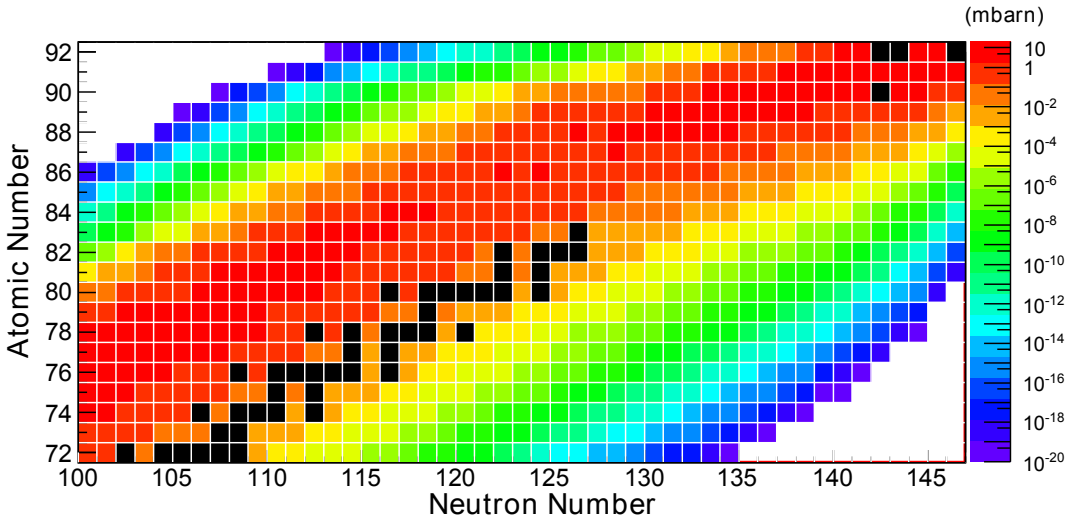

Figure 1.4: Calculated [Gai91] production cross-sections for projectile fragments created with a ^{238}U beam interacting with a Be target at 1000 MeV/u. The stable nuclei are marked by black boxes.

wanted reaction fragments with the FRS, before they can be investigated or used for secondary reaction experiments. In general, due to the finite ion-optical acceptance of the separator, not all fragments are transmitted to the final focal plane. As an example, Figure 1.3 shows the phase-space population and the acceptance of the FRS for ^{213}Fr produced via fragmentation of ^{238}U beam in beryllium target at 1000 MeV/u.

1.3 Spatial separation with the in-flight separator FRS

The GSI FRagment Separator (FRS) is a high resolution magnetic spectrometer designed for research studies using relativistic heavy ions [Gei92]. Heavy-ion beams with magnetic rigidities ranging from 5 to 18 Tm can be analyzed using this spectrometer.

The main branch of the FRS consists of four sections. Each of them consists of one 30° dipole magnet, five quadrupole magnets and two sextupole magnets. Consequently there are four focal planes (F1-F4). The resolving power of the FRS ($B\rho/\Delta B\rho$) is 1500 at an emittance of 20π mm $mrad$, the longitudinal-momentum acceptance ($\Delta p/p$) is $\pm 1\%$ and the angular acceptance ($\Delta\theta$) is ± 10 mrad. The total orbital length of the FRS is approximately 72 m.

The first two dipole stages of the FRS serve as a first filter of the projectile fragments. In the central focal plane a specially shaped degrader is placed which allows a second filter with the remaining two dipole stages. This B$\rho-\Delta$E$-$Bρ method allows an ideal spatial separation of the nucleus of interest.

The B$\rho-\Delta$E$-$Bρ separation

The motion of heavy ions with the charge q and the momentum $p = mv$ in a homogeneous magnetic field B is described by the Lorentz force:

$$\vec{F}_{Lorentz} = \frac{d}{dt}(m \cdot \vec{v}) = q\vec{v} \times \vec{B}. \tag{1.5}$$

For the FRS, the magnetic field is perpendicular to the heavy ions momenta and the Lorentz force is set to compensate the centrifugal force:

$$F_{Lorentz} = \frac{mv^2}{\rho}, \tag{1.6}$$

with ρ being the bending radius of the trajectory. Furthermore, the energies are relativistic, so the momentum transforms to $p = \beta\,\gamma\,m\,c$ with the velocity $\beta = v/c$ where c is the speed of light, the Lorentz-factor $\gamma = \sqrt{\frac{1}{1-\beta^2}}$, u is the atomic mass unit, q is the ionic charge state of the fragment and e is the electron charge (1.6×10^{-19} C). If the heavy ions are fully stripped (q = Z), this leads to:

$$B\rho = \gamma\,\beta\,c\frac{m}{Ze}. \tag{1.7}$$

The FRS separates the fragmentation products in three stages. In the first stage, the first pair of dipole magnets selects heavy ions according to their magnetic rigidity. As the bending radius for the dipole magnets is fixed to 11.25 m and the velocity β is approximately the same for all fragments at the output of the target, the B-field applied to the magnets determines the selected A/Z range within the acceptance of the magnets.

The central image plane of the FRS (middle focus) is dispersive. This means that heavy ions with different magnetic rigidity Bρ pass the middle focus at different X-positions. The distance ΔX between two individual heavy ions is proportional to their relative difference in magnetic rigidity ΔBρ /Bρ:

$$\Delta X = D \cdot \frac{\Delta(B\rho)}{B\rho}, \tag{1.8}$$

where D is the ion-optical dispersion. From the primary target to the central focus the dispersion is -6.47 cm/%. Thus, the accepted Bρ range can be reduced if X-position slits are inserted.

The fragments that reach the central focus have to penetrate through a scintillator detector and a degrader system [Fol91]. The corresponding energy loss represents the second separation criterion together with the magnetic rigidity measurement. The degrader system consists of three different parts: a set of homogeneous plates, a pair of wedge-shaped discs and a homogeneous variable degrader, see Figure 1.5. The ladder and the wedges present the homogeneous parts of the degrader, i.e. their thickness is independent of the X-position. With the wedges any thickness between 270 and 6750 mg/cm^2 of aluminium can be set up, while the ladder consists of several aluminium blocks of a fixed thickness. If the degrader disc is used, another 737 mg/cm^2 of aluminium are inserted into the beam line. By changing its slope, that is by rotating it along the beam axis, different ion optical modes can be achieved. In the monoenergetic mode, the degrader system is set to reduce the momentum spread of the selected fragment. In this case the monoenergetic degrader as to be placed in the dispersive focal plane. The achromatic degrader preserves the overall ion-optical achromatism at

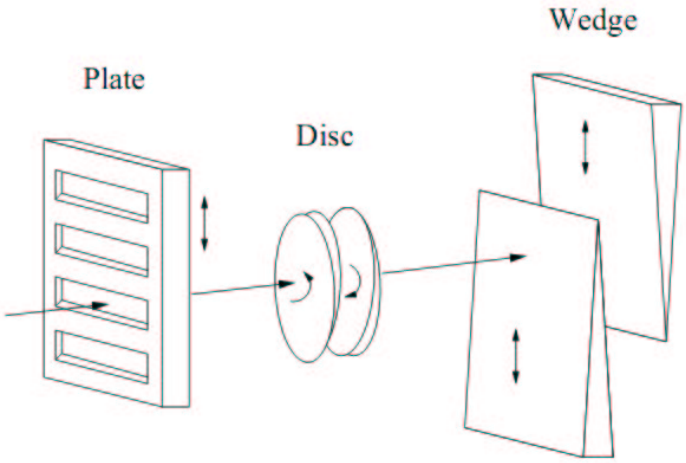

Figure 1.5: Schematic view of the FRS degrader system [Fol91].

the final focal plane, i.e. the size of the fragment spot has a minimum. The monoenergetic degrader is preferably used in implantation experiments to reduce the range straggling in the stopper material.

The simulation for the settings of the Fragment Separator and the optimization for the beam production was done with the MOCADI program [Iwa97]. The program calculates the transport of particles through ion optical systems and layers of matter. For each fragment of interest, simulations with different degrader thicknesses were done in order to have the best values for the intensity of the selected fragment and the lowest contribution from contamination. The separation performance for the case of ^{213}Fr, as calculated with the MOCADI program, is shown in Figure 1.6.

1.3.1 The particle identification detectors of FRS

All of the multiple species of reaction products from fragmentation can in principle be transmitted to the final focal plane of the FRS. Therefore, it is necessary to achieve unambiguous particle identification of the ions on event by event basis. In the present experiment the identification in-flight was achieved by measurements with three different types of detectors: (i) plastic scintillators for the time of flight determination (TOF); (ii) ionization chambers for the atomic number measurements; and (iii) time projection chambers for position measurements. By

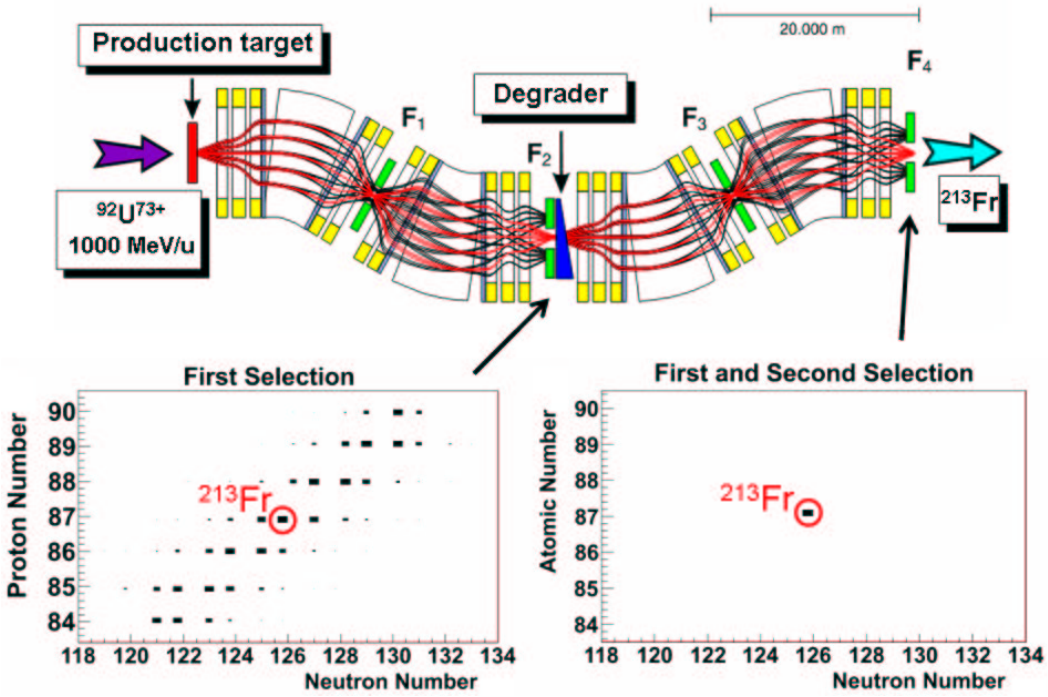

Figure 1.6: Ion-optical scheme of the FRS. The calculated [Iwa97] path of the projectiles fragments with different A/Z ratios is shown and the separation is marked (red: path of the selected ions, black: fragments which are separated with the Bρ selection). On the bottom, the plots show the calculated isotopic composition of the secondary beam after the separation in the first half, TA-F2, (left panel) and after the full Bρ−ΔE−Bρ separation (right panel). The size of the squares represents the corresponding intensity of the isotope (logarithmic scale).

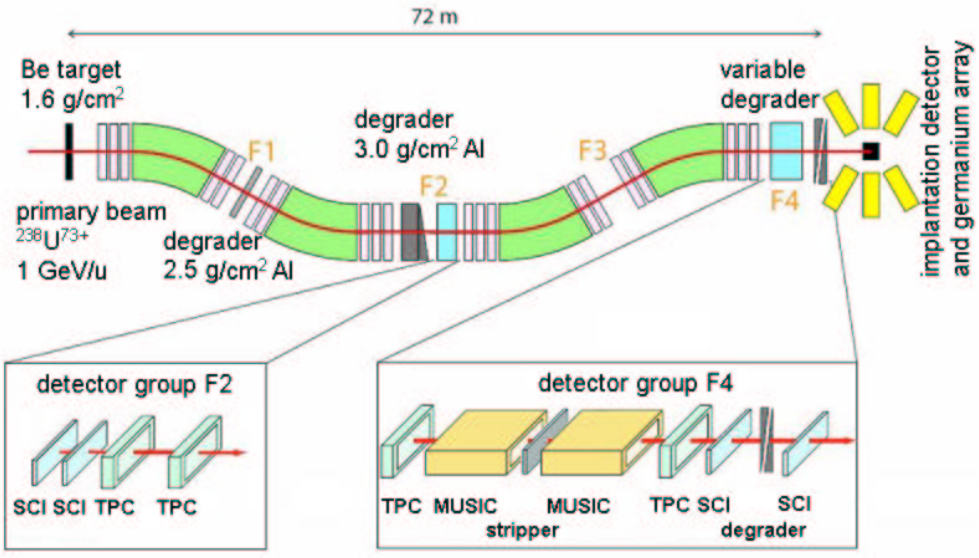

Figure 1.7: Schematic view of the experimental setup of the FRS used for the production and identification of new isotopes, described in Chapter 3. The Time Projection Chambers (TPC) are used to measure the positions thus providing the angles and the magnetic rigidities, MUltiple Sampling Ionizing Chambers (MUSIC) are used to record the energy deposition providing in this way the determination of the atomic number and scintillation detectors provide the time-of-flight measurement between the focal planes F2-F4.

combining the data recorded with these detectors and the measured magnetic rigidity (Bρ) of the dipole magnets, the mass to charge ratio (A/Q) and the atomic number (Z) can be evaluated and used to identify the nuclear species which arrived at the final focal plane. Figure 1.7 shows a schematic view of the detector configuration applied at the FRS.

Plastic Scintillator

The plastic scintillators were used for measuring the time of flight (TOF) of the particles passing through the FRS. Two plastic scintillators were used at the central (SCI1) and final focal plane (SCI2) of the FRS. The sensitive area of the scintillators was around 200 mm $\times$ 80 mm with a variable thickness between 0.5 mm and 3.5 mm [FRS11]. In addition, two scintillator were mounted up- and

downstream the implantation setup (see Section 1.5), to optimize the degrader thickness. The scintillators are made of Bicron BC-420 [Bic11], a plastic material characterized by a high efficiency in the production of light and has a fast time response of about 1.5 ns.

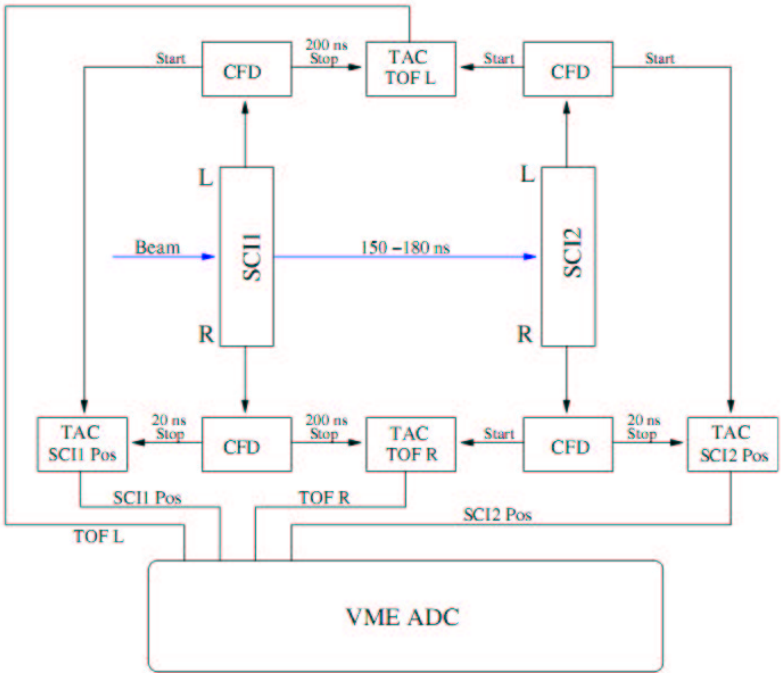

Figure 1.8: Schematic view of the electronics used for time-of-flight measurement between F2-F4. SCI1 is used as the stop detector and is placed at F2 and SCI2 is the corresponding start detector placed at F4. The sequence of signal processing is based on the aim to reduce the dead-time. (CFD: constant fraction discriminator, DL: delay, TAC: time to amplitude converter, ADC: amplitude to digital converter).

Each side of the plastic scintillator was connected to a photo-multiplier (PM), where the light was converted to an electronic signal. The output from the PM was connected to a constant-fraction discriminator (CFD), where the analog signals were converted to digital time signals independent of their amplitude and rise time. The time signals of the two CFDs provide the start and stop for a time-to-amplitude converter (TAC). The output analog signal of the TAC corresponding to the time difference was sent to an amplitude-to-digital converter (ADC) and processed by the data acquisition. A high time resolution is achieved by correcting

the time-of-flight variation due to the different positions the ions impinge on the scintillators. This is taken into account by left-right coincidence at each detector (see Figure 1.8).

Multi Sampling Ionization Chamber

At the final focal plane of the FRS, we placed the Multi Sampling Ionization Chamber(MUSIC) [Schn00] for the charge measurement of the fragments. The MUSIC is an ionization chamber filled with CF_4 gas or Ar + 10% CH_4 gas (P10) at normal pressure and room temperature. The active area of the detector is (200×80) mm^2 and the length is 400 mm. A schematic view of the MUSIC detector with the readout electronics is shown in Fig.1.9. The charged particles

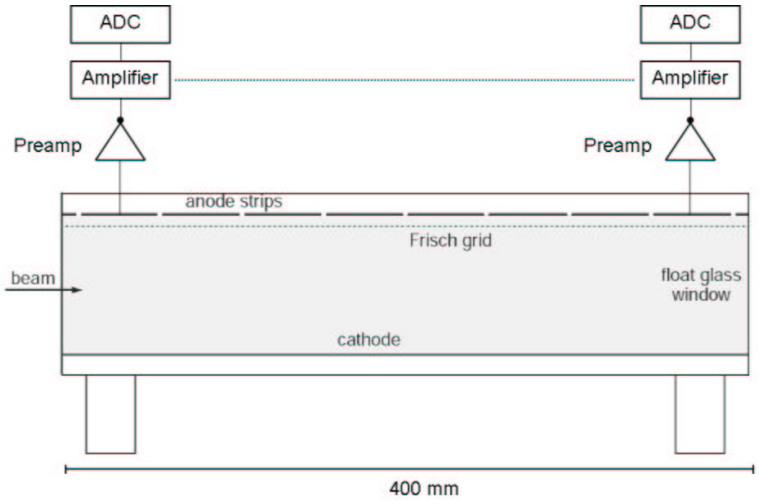

Figure 1.9: Schematic view of the MUSIC detector and its readout electronics as used in the experiment [Schn00]. The charged particles passing through the active volume create clouds of ions and free electrons by ionization. In the presence of an electric field the electrons drift toward the 8-fold segmented anode. Each anode segment is connected to the charge-sensitive preamplifier. The signal is further amplified and is digitalized using a peak-sensing ADC (two electronic branches of an anode are shown, as an example, in the figure).

passing through the active volume create clouds of ions and free electrons by ionization. In the presence of an electric field the electrons drift toward the 8-fold segmented anode. Each anode segment is connected to the charge-sensitive

preamplifier. The signal is further amplified and is digitalized using a peak-sensing ADC.

The energy deposition of charged particle in the MUSIC is in first approximation proportional to the square of the ionic charge of the projectile.

Time Projection Chamber

The Time Projection Chamber (TPC) [Jan11, Pro11] were used for the position determination and tracking of the fragments. Two chambers were placed at the central focal plane (F2) and two were placed at the final focal plane (F4). These detectors consist of vertical drift space inside a field cage terminated on the lower part by a gating grid. Underneath the grid there are placed four proportional counters with C-pad cathodes (Fig. 1.10).

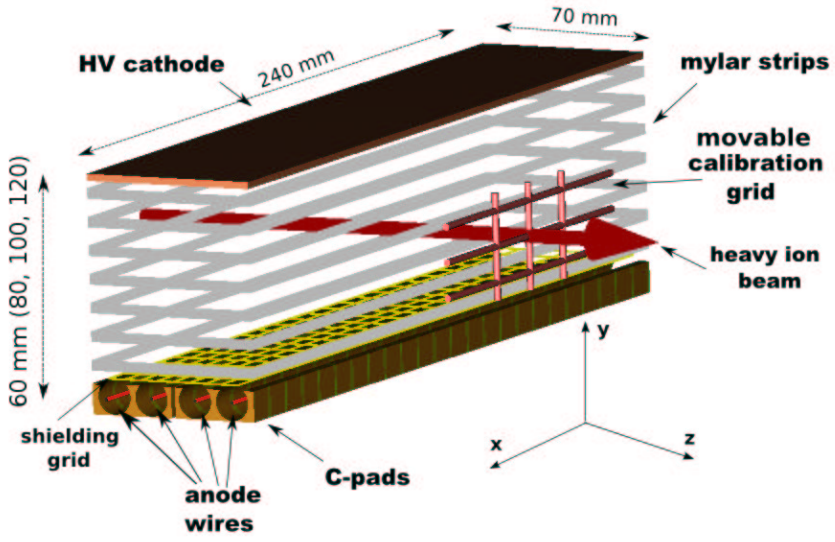

Figure 1.10: Schematic view of the Time Projection Chamber [Jan11]. X is in the direction of the dispersive ion-optical coordinate, Y is perpendicular and Z is along the optical axis. There are several detector modules, which differ in the dimension in the vertical direction, e.g. 60, 80, 100, 120 mm.

The drift volume is filled with 90% Ar + 10% CH_4 gas (P10) or Ar + 10% CO_2 at atmospheric pressure and room temperature. A voltage up to 400 V/cm is

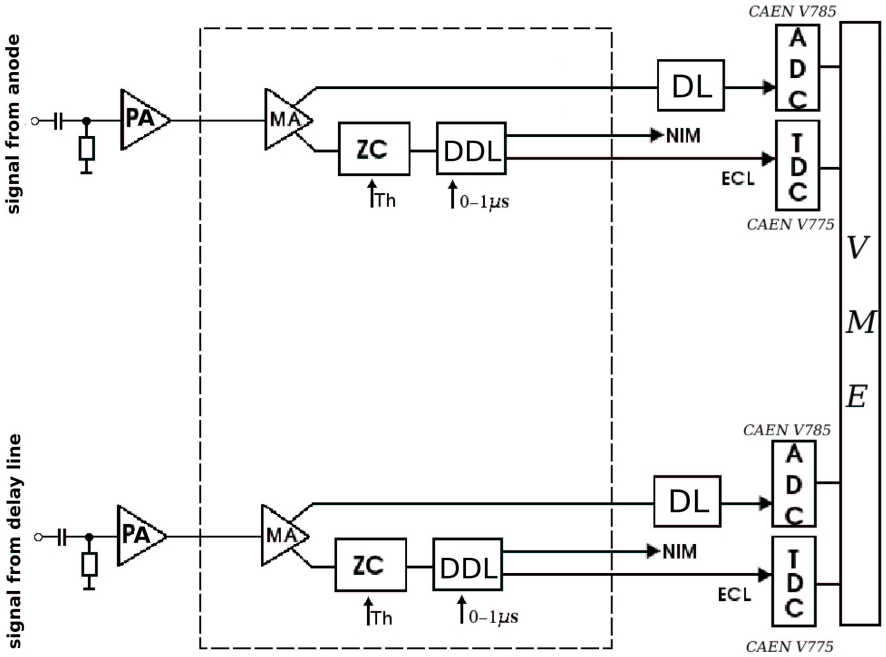

Figure 1.11: Block diagram of the TPC electronics [Jan11]. The upper part represents an example for the position measurement in the Y-direction using the TDC. The other branch after the main amplifier (MA) provides the information on the energy deposition. The total energy deposition inside the chamber can be derived from the geometrical mean of the energy deposition in each anode. The lower part is the corresponding electronic branch for the X coordinate. (PA: preamplifier, MA: main amplifier, DL: passive delay, ADC: analog to digital converter, ZC: zero crossing discriminator, Th: threshold, DDL: logic delay up to 1 μs, TDC: time to digital converter.)

applied and forms a uniform electric field inside the drift volume. The proportional part is placed under the drift space and consists of four anode wires (20 μm in diameter) placed inside C-pad formed cathodes. Each C-pad is connected to an integrated passive delay line chip. Each TPC has two independent delay lines.

The electron drift time is used for the measurement of the y-coordinate. The x-coordinate is determined by measurement of the time difference between the arrival of the induced signal from the left and the right side of the delay line. Each TPC provides two independent x-position measurements and four y-position measurements.

The signals from the delay lines and the anodes are sent to the preamplifiers and main amplifiers. Each signal is then split into analog and digital signal. The analog branch provides an energy-loss measurement. In the digital branch a zero-crosser provides a logical pulse for the stop (start) signal for a time-to-digital converter (TDC). The zero-crosser gives considerably better timing especially for heavy ions than the usual leading edge or constant fraction discriminator (see Fig. 1.11). A common start (stop) is provided by the FRS trigger.

The Isomer Tagging Array

This detector, its commissioning and the first contributions to FRS experiments are described in detail in Chapter 2. ITAG (Isomer TAGging detector) [Far10] is a detector developed for isotope identification by isomer tagging at the FRS. It is placed at the final focal plane of the FRS and detects γ-rays emitted from μs-isomers implanted into its catcher. The rapid on-line analysis of the gamma lines from known isomers unambiguously determines the corresponding isotope in the in-flight identification matrix (Z vs A/Z, see Fig. 1.20). In this way, the whole matrix is determined. The development and application of ITAG and its performance were a major experimental part of this doctoral work.

1.4 Particle identification

The identification of the fragments in-flight by nuclear charge (Z) and mass number (A) is routinely done at the FRS. It is based on measurements of time of flight, energy deposition and magnetic rigidity (Fig. 1.12). A verification is done

by detecting γ-rays from known μs-isomers in coincidence with the incoming fragments.

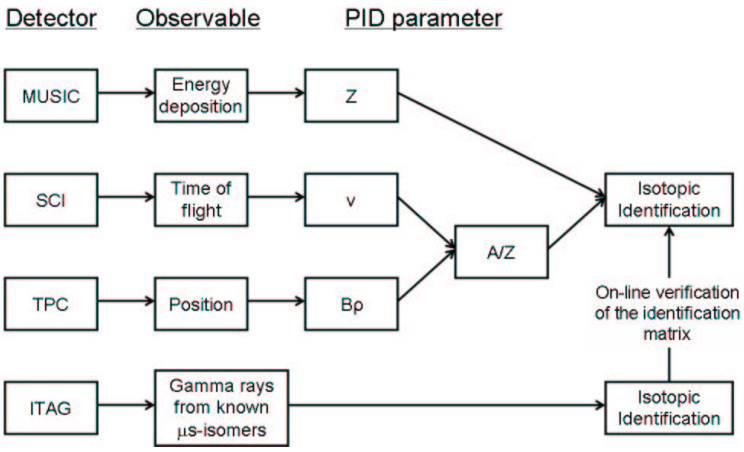

Figure 1.12: Schematic view of the FRS detector setup and their physical identification contribution. The fragments are identified by their nuclear charge Z ($q = Z$) and mass number A. The Z is determined by the MUSIC detectors measuring the energy deposition, the mass is determined from the A/Z ratio obtained from the magnetic rigidity ($B\rho$) and velocity (v) measurements provided by the TPC detectors and plastic scintillators (SCI), respectively. An independent identification can be done via detecting γ-rays from known μs-isomers with the ITAG detector.

1.4.1 Energy loss, energy deposition and Z determination

The energy deposition of swift heavy ions penetrating the active volume of the detectors (e.g. MUSICs, scintillators, TPCs and silicon detectors) is used to derive the Z identification of the fragment beams in the FRS. In addition, applying the Bρ−ΔE−Bρ separation method (see Chapter 1.3), the energy loss of the fragments traveling through thick degraders is applied to achieve isotopic spacial separation at the final focal plane of the separator. The thickness of the degrader material (d) is typically of the order of half of the atomic range (R) of the reference fragment ($d/R = 0.5$). Therefore, a precise knowledge of the atomic interaction is required to achieve an unambiguous isotopic separation of all fragments up to uranium [Gei92, Sch94, Sch96, Lin96, Wei00, Gei02]. For example, a wrong

momentum prediction of about 1% behind a thick F2 degrader would result in an unwanted position shift at F4 of more than 7 cm which easily would cause a wrong spacial isotopic separation.

The energy loss of relativistic heavy ions is dominated by the energy transfer to the atomic electrons (inelastic stopping power) of the target/degrader material. Under the assumption of fully stripped ions, the stopping power can be described by [Lin96]:

$$\frac{dE}{dx} = \frac{4\pi}{m_e c^2} \frac{(Ze^2)^2}{\beta^2} N Z_2 L, \tag{1.9}$$

where $N \cdot Z_2$ is the average density of electrons per unit volume in the absorbing material, m_e and e are the electron rest mass and unit charge, respectively, β is the velocity of particles relative to the speed of light c and L is the dimensionless stopping number.

At relativistic energies L can be expanded according to:

$$L = L_0 + \Delta L_{LS}, \tag{1.10}$$

where

$$L_0 = ln\left(\frac{2m_e c^2 \beta^2}{I}\right) - ln(1-\beta^2) - \beta^2 - \delta/2, \tag{1.11}$$

where I is the mean excitation energy and the Fermi density effect, $-\delta/2$, accounts for the dielectric polarization of the stopping medium at relativistic velocities. L_0 is usually referred as the Bethe stopping power formula [Bet32]. ΔL_{LS} represents the contribution of relativistic collisions in the Lindhard-Soerensen model [Lin96] which includes the Mott scattering and the deviation from the first Born approximation.

The energy loss in thick material has to be considered in terms of the corresponding atomic ranges. The range is defined as:

$$R = \int_0^E \frac{1}{\frac{dE'}{dx}}\, dE'. \tag{1.12}$$

The total energy loss in the thickness d of the stopping material can then be calculated as:

$$\Delta E(d) = E_1 - E_2, \tag{1.13}$$

where E_1 is the incident energy and E_2 is the outgoing energy of the projectiles, which are related by the corresponding ranges:

$$d = R(E_1) - R(E_2). \tag{1.14}$$

In this way the magnetic rigidities are routinely calculated for the FRS experiments with the MOCADI program [Iwa97]. In the MOCADI program the Lindhard-Soerensen theory [Lin96] is included. In most experiments, the reference fragment is selected as a bare ion. However, even at 1000 MeV/u the fragments emerge from the target and degraders to small fractions also with bound electrons (H-like and He-like). The total energy loss in the degrader allows for an additional separation criterion with fragments emerging in different charge states. The energy loss in the target/degrader system can be accurately measured with two-fold Bρ analysis at the FRS.

The energy deposition (ΔE*) is defined as a restricted energy-loss in the active volume of an ionization detector, like the MUSICs. The fragments penetrating through the detector volume primarily create electron-ion pairs which are electrically recorded during the experiment. However, there are also high energy δ-rays produced, which may leave the detector volume without contributing completely to the ionization process inside. Therefore, the energy deposition is in principle smaller than the energy-loss of the fragments. Furthermore, the missing contribution of high energy δ-rays results in a smaller tail of the energy-loss distribution, thus providing a higher resolution for Z determination in a gaseous ionization chamber [Pfü94]. The energy deposition scales in a very good approximation with the square of the ionic charge state of the projectiles. This relation is the base of the Z determination in our MUSIC detectors.

The measured energy deposition from the ^{238}U primary beam at three different velocities in the two MUSICs is presented in Figure 1.13. All the produced projectile fragments of the present experiment are thus covered in the velocity range of this calibration.

For particles being slowed down in the same absorber material the stopping power can be expressed as:

$$-\frac{dE}{dx} = Z^2 f(\beta), \tag{1.15}$$

where $f(\beta)$ depends only on the velocity. As a consequence, $f(\beta)$ can be measured

for the primary beam with the atomic number Z_p and then scaled to the energy loss values of fragments (dE_f/dx) with atomic number Z_f if the $f(\beta)$ value is the same:

$$-\frac{dE_f}{dx}(\beta) = -\frac{Z_f^2}{Z_p^2}\frac{dE_p}{dx}(\beta). \tag{1.16}$$

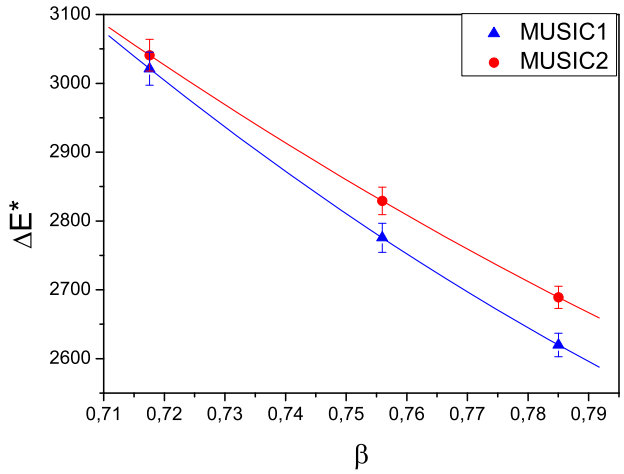

Figure 1.13: Calibration of the energy deposition (ΔE^*) from the primary beam in the two MUSIC detectors as a function of the velocity β. The different β values are obtained by inserting different well known material layers in the beam axis at the central focal plane. The measured magnetic rigidity of the primary beam directly provides the velocity values. The line represents the second order polynomial fit of the data to relate fragments and primary beam to the same velocity in the identification procedure.

A monoisotopic beam penetrating the gas volume with different trajectories deposit slightly different energy in the MUSIC, which results in a position dependence, shown in Figure 1.14. In this example, the primary beam of ^{238}U projectiles is dispersed in X direction by defocussing with the quadrupole magnets of the last dipole stage before the beam is entering the MUSIC. This measured position dependence has been taken into account by a fourth-order polynomial fit in order to improve the experimental resolution of the ionization chambers because a cocktail beam of fragments illuminates the MUSIC as well. The overall energy

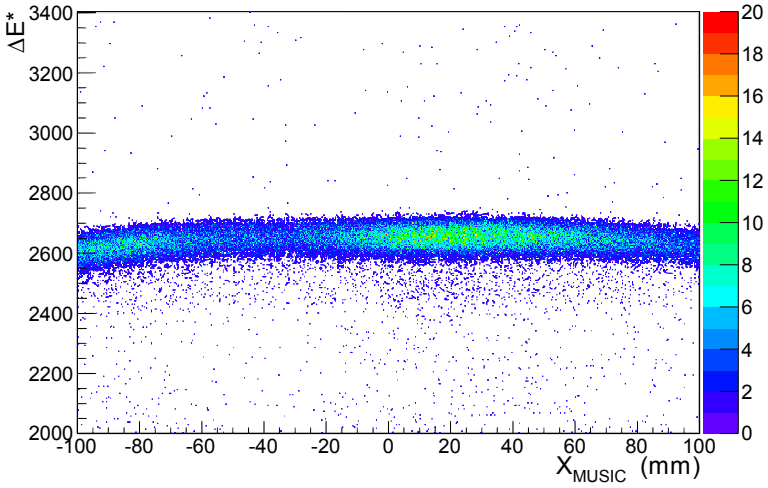

Figure 1.14: Measured energy deposition in the first MUSIC as a function of the position in X direction (X_{MUSIC}) for a calibration run of the ^{238}U primary beam. The position dependence is approximated by a forth order polynomial fit.

deposition in the MUSIC was calculated by the geometrical mean of the 8 anodes according to the equation:

$$\Delta E^* = \sqrt[8]{\prod_{i=1}^{8} \Delta E_i^*} \tag{1.17}$$

where ΔE_i^* is the measured energy deposition from a single anode.

The atomic number of the bare fragments Z_f can be determined from the energy deposition calibration measured with the primary beam at different velocities. For identification purposes, a simple scaling can be applied:

$$Z_f = Z_p \sqrt{\frac{\Delta E_f^*(\beta_f)}{\Delta E_p^*(\beta_f)}}. \tag{1.18}$$

The charge state distribution spectra measured with the MUSIC detectors at the F4 focal plane after the velocity and position corrections are shown in the Figure 1.15. The spectra were both measured with projectile fragments at a magnetic field setting of the FRS for the reference ion ^{205}Pb with an incident charge state of q=82+. The measurements clearly show a strong dependence of the charge resolution on the gaseous medium in the detector. The spectrum on the left-hand side was measured using as a medium P-10 gas, which is a mixture composed of 90% Ar and 10% methane. The corresponding spectra on the right-hand side shows the charge resolution for a CF_4 medium. Both gases were applied

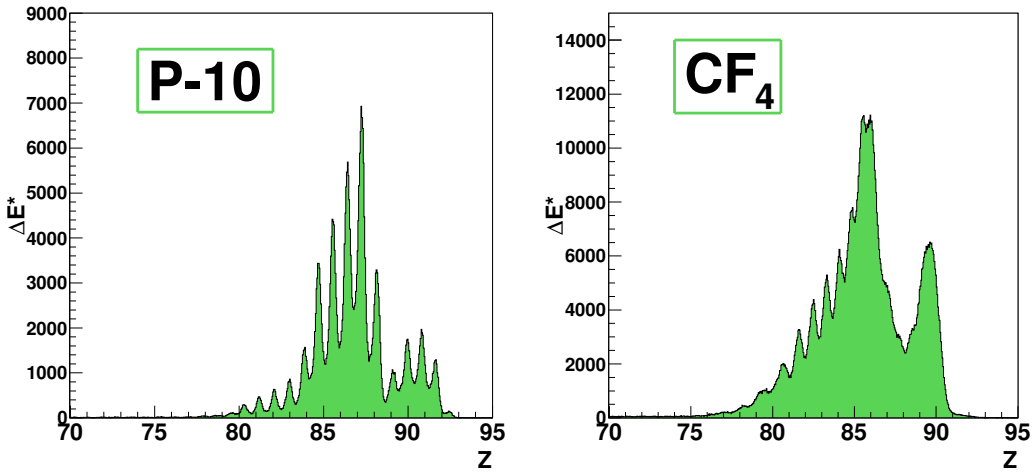

Figure 1.15: Nuclear charge distribution from energy-deposition measurements in the MUSIC at F4. The observed resolution strongly depends on the detector gas, which is illustrated for fragments between $80 < Z < 92$ at about 500 MeV/u (^{205}Pb setting). On the left panel, the detector gas was P-10 (90% Ar + 10% CH_4 gas); on the right panel, the detector gas was CF_4. The measured charge resolution was $\sigma_Z \sim 0.24$ with P-10 gas and $\sigma_Z \sim 0.87$ with CF_4 gas. Both presented distributions were corrected for the velocity and position dependence of the energy deposition inside the MUSIC.

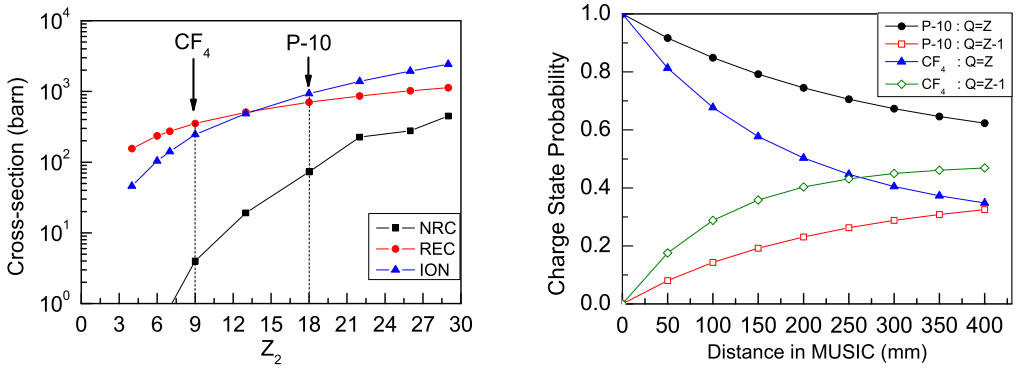

Figure 1.16: Left panel: Calculated [Sch98] electron-capture and ionization cross section of 500 MeV/u ^{238}U projectiles in different media characterized by the atomic number Z_2. Right panel: Calculated [Sch98] charge-state evolution for 500 MeV/u ^{238}U projectiles with an incident charge state of q=92+, penetrating the MUSIC filled with Ar gas or CF_4 gas at 1 atmosphere at room temperature. The data points are calculated at the exit of the 50 mm long anodes.

at atmospheric pressure and room temperature. The obtained charge resolution at F4 was $\sigma_q \approx 0.24e$ with P-10 gas and $\sigma_q \approx 0.87e$ with CF_4 gas. The physical reason for the observed difference is the due to the different charge-changing cross-sections of the two gaseous media. At these relativistic energies, for the considered projectile-medium combination, the dominant cross-sections are the radiative electron capture (REC) and the ionization (ION). The non-radiative electron capture (NRC) is significantly smaller, see Fig. 1.16 Left Panel. The effect of the difference in the ionization ($\sigma_{ion}(CF_4)/\sigma_{ion}(P-10) \approx 0.26$) and the radiative electron capture ($\sigma_{REC}(CF_4)/\sigma_{REC}(P-10) \approx 0.5$) cross-sections is also reflected in the charge state evolution shown in Figure 1.16 Right Panel. In our case, the considered projectiles have a smaller charge-changing straggling in P-10 gas, reflected in the narrower energy deposition spectra 1.15.

In figure 1.17 we plot the measured energy loss in the F2 degrader, versus the charge states in the MUSIC deduced from energy deposition measurement. The field setting of the FRS was tuned for the reference fragment $^{212}_{86}$Rn. Combining the information from the energy deposition in the MUSICs, the energy loss in the thick F2 degrader and the Bρ measurement, we are able to disentangle different

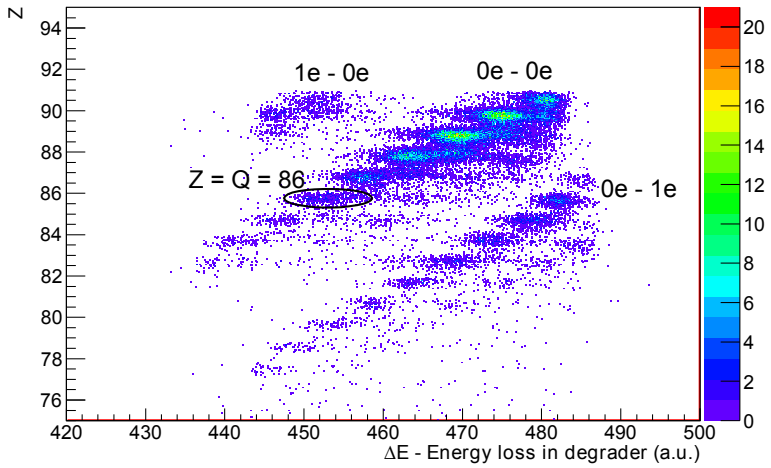

Figure 1.17: Scatter plot of the energy loss in the intermediate degrader in relation to the energy loss measured with the two ionization chambers q_{eff} corresponding to an FRS setting optimized to transmit ^{212}Rn. The number of bound electrons of the fragments transported through the TA-F2 and F2-F4 FRS stages are indicated in the measured spectrum. As an example, the label $0e - 1e$ means that the fragments were bare in the first two stages (TA-F2) and H-like in the second two stages (F2-F4).

charge states for the same element and also different Z in the same ionic charge state.

1.4.2 Time of flight measurement

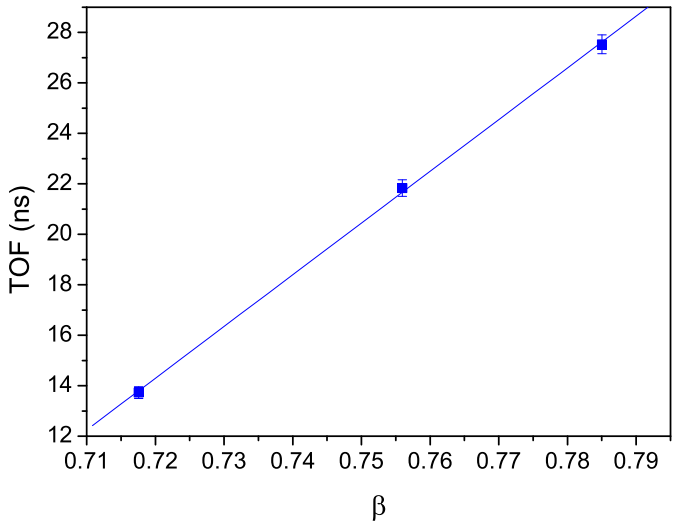

Figure 1.18: TOF calibration with three well known velocities (β) of the ^{238}U primary beam.

The time of flight (TOF) of the fragments in the FRS is obtained by measuring the time differences between a plastic scintillator placed at F2 (SCI1) and one placed at F4 (SCI2). The measured TOF resolution with these plastic detectors was in the range of $\sigma_{TOF} \approx 30$ ps. The flight time of the fragments between F2 and F4 with an energy of around 500 MeV/u is in the range of 160 ns. Due to the B$\rho-\Delta$E$-$Bρ separation method, the total rate of the incoming ions at F2 is usually much larger than the corresponding rate at F4. Therefore, it is advantageous to use the signal from the F4 TOF detector as a *start* of the Time-to-amplitude converter (TAC) and the corresponding signal from F2 provides the *stop*, as shown in Figure 1.8. In this way, we can avoid an unnecessary high dead-time in our data acquisition. Since the fragments in our experiment have almost the same velocity, it is practical to use the most sensitive range of the TAC which can be established by adding suitable delays to the electronic circuits. The

absolute calibration of the time-of-flight measurement has been performed with three well known velocities of the primary beam as shown in Figure 1.18.

1.4.3 Position measurement

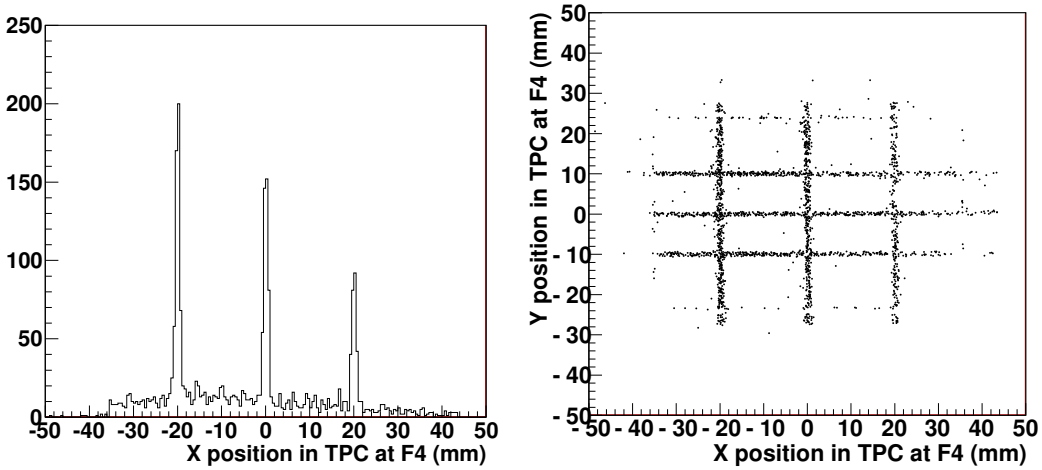

Figure 1.19: A typical TPC calibration spectrum for the x-position (left panel) and the corresponding 2-dimensional position spectrum showing the structure of the scintillator grid(right panel). The presented spectra were recorded for a defocused ^{238}U beam at around 750 MeV/u.

The position calibration of the TPCs [Jan11] is performed via coincidence measurement with a scintillator grid of well known dimensions. This goal is achieved by illuminating the active volume of the TPCs with a defocused primary beam at the central and final focal plane. The active scintillator grid consists of thin scintillator fibers of 1 mm thickness. The rectangular scintillator grid consists of 3 fibers in the vertical direction with a distance of 20 mm and 3 fibers placed horizontally with a distance of 10 mm. In this way, only ions which pass through the scintillator grid are recorded as shown in Figure 1.19.

1.4.4 A/q measurement

The mass-over-charge ratio can be determined from the combination of Bρ and time-of-flight measurements according to the equation:

$$\frac{A}{q} \approx \frac{B\rho\, e}{\beta\, \gamma\, c\, u} \tag{1.19}$$

where β is the particle velocity, γ is Lorentz factor, u is the atomic mass unit and $B\rho$ is the magnetic rigidity. The relative magnetic rigidity of the ions transported

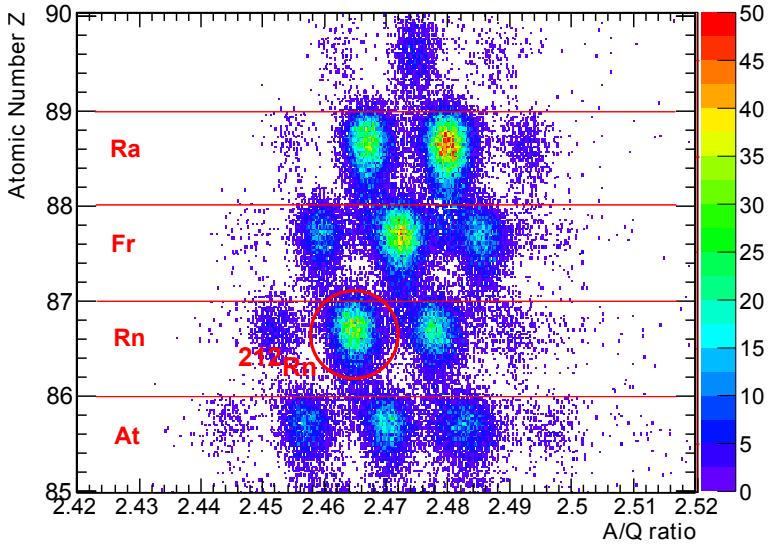

Figure 1.20: Z versus A/q particle identification plot for the FRS setting optimized for the transmission of fully stripped ^{212}Rn.

through the FRS is determined by the actual position measurement relative to the optical axis and the magnetic field measurement. Furthermore, the ion-optical dispersion and magnification at the focal planes are required for this determination. The Bρ of the fragments was reconstructed by applying the formula:

$$B\rho(x_{F2}, x_{F4}) = B\rho_{F2-F4} \left(1 - \frac{x_{F4} - M_{F2-F4} \cdot x_{F2}}{D_{F2-F4}}\right), \tag{1.20}$$

where Bρ_{F2-F4} corresponds to the magnetic rigidity of trajectories on the optical axis from F2 to F4, D$_{F2-F4}$ and M$_{F2-F4}$ are the dispersion and the magnification at the final focal plane, respectively.

Combining equation 1.19 and 1.20 the mass-to-charge ratio can be deduced. An example of the resulting particle identification plot is shown in Fig. 1.20.

1.5 Detector setup for decay measurements

In order to study the decay properties of the projectile fragments and to confirm the identification matrix using known μs-isomers, an appropriate detector system for γ radiation and α particles was used at the final focal plane of the FRS. The setup for α-decay investigations consisted of a closely packed stack of double sided silicon strip detectors (DSSD) arranged in two layers (Si1 and Si2), each of 1 mm thickness. The α-emitting fragments were implanted in the first silicon layer. For the verification of the identification matrix using known μs-isomers, a layer of matter (passive catcher) replaced the silicon detector. The passive catcher was surrounded by Germanium detectors (ITAG or RISING) for recording γ-rays. In both cases, it was necessary to stop the 450-500 MeV/u projectile fragments in a thin volume of matter. Therefore, a variable homogeneous degrader was installed in front to slow down the fragments to match the range distribution to the catcher thickness. Two plastic scintillators were placed in front and behind the catcher. The first one served to remove in the analysis the secondary fragments which have changed the atomic number due to reactions in the degrader. The second one acted as a veto counter for the implantation (Fig. 1.21). To assure that the maximum number of selected ions was stopped inside the catcher, the thickness of the variable degrader was calibrated with the primary beam. As an example, Figure 1.22 shows the normalized count rate, the ratio of the number of implanted ions over the incident ones, for the two silicon detectors (Si1 and Si2) as a function of the degrader thickness. Differentiating the measured two number distance curves, yields directly the corresponding range distributions, which are shifted just by ~ 250 mg/cm^2 equivalent to a measured thickness of Si1 of 1.08 mm. An similar calibration procedure was done with the passive catcher. In this case, the degrader thickness was varied until no counts were observed in the veto counter (SCI3 in Fig. 1.21).

1.5.1 Germanium detectors

For the detection of isomeric γ-rays emitted after an implantation event, germanium detectors (ITAG or RISING) were used. The procedure to perform measurements with germanium detectors, as well as a complete description of the

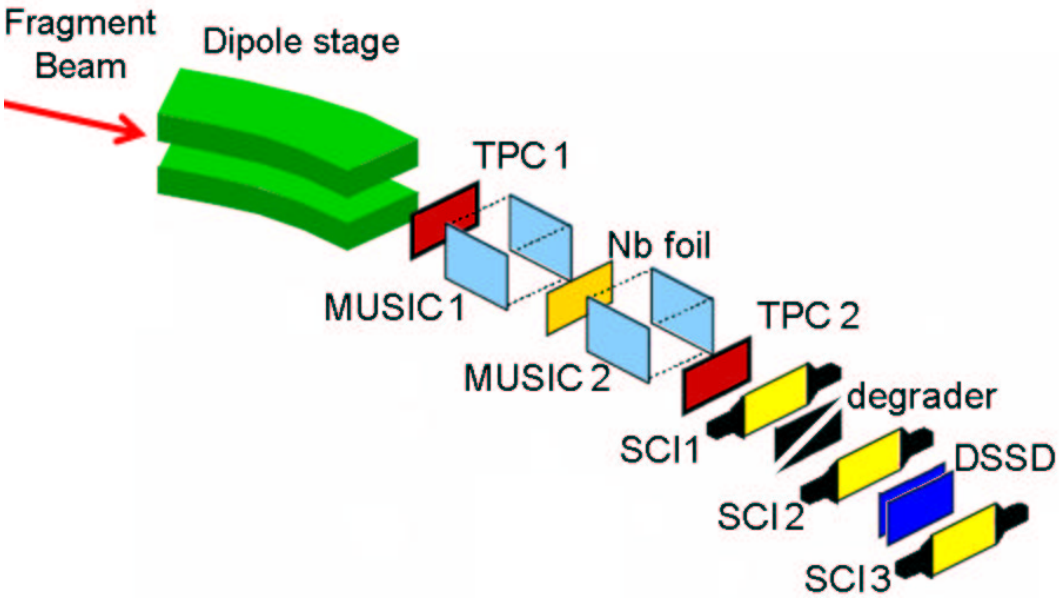

Figure 1.21: Schematic view of the implantation setup at the final focal plane of the FRS during the α-decay experiment described in Chapter 4. Behind the final dipole stage (quadrupole lenses plus a 30° dipole magnet) of the FRS TPCs, MUSICs (with a Niobium stripper in between) and the first scintillator (SCI1) provided the identification in-flight of the separated fragments. The variable homogeneous degrader was installed to slow down the fragments for the implantation in the DSSDs. The second scintillator (SCI2) was used in the analysis to discriminate the secondary fragments from charge-changing reactions in the degrader. The third scintillator (SCI3) served as a veto counter.

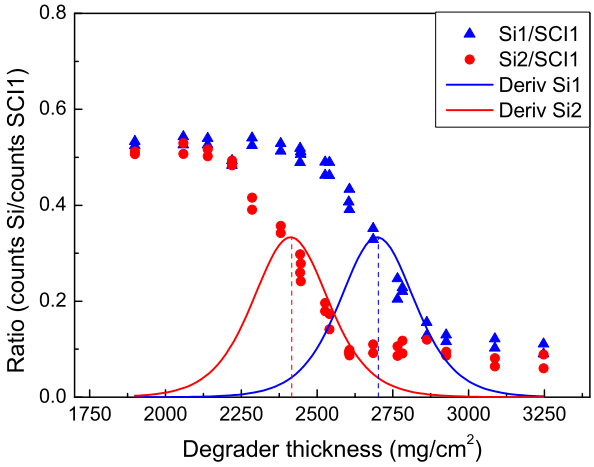

Figure 1.22: The normalized implantation rate (number distance curves) for the two DSSD detectors as a function of the degrader thickness. The silicon detector Si1 is upstream compared to detector Si2. Differentiating the measured two number distance curves, yields directly the corresponding range distributions, which are shifted just by the thickness of Si1.

ITAG setup will be discussed in Chapter 2.

RISING Array

The RISING array [Pie07] (Figure 1.23) is composed of 15 Euroball Germanium detector clusters [Wil96] mounted in the so called Stopped Beam configuration. Each of the 15 clusters houses 7 separate Germanium crystals, amounting to a total of 105 independent Germanium detectors. In the Stopped Beam configuration the detectors are mounted in three rings each containing 5 detector clusters with angles of 51°, 90° and 129° relative to the beam axis. The distance of the detectors to the center on the beam axis was approximately 22 cm. The measured γ-photopeak efficiency is 15% at 661 keV and the energy resolution is about 3 keV FWHM at 1.3 MeV [Pie07].

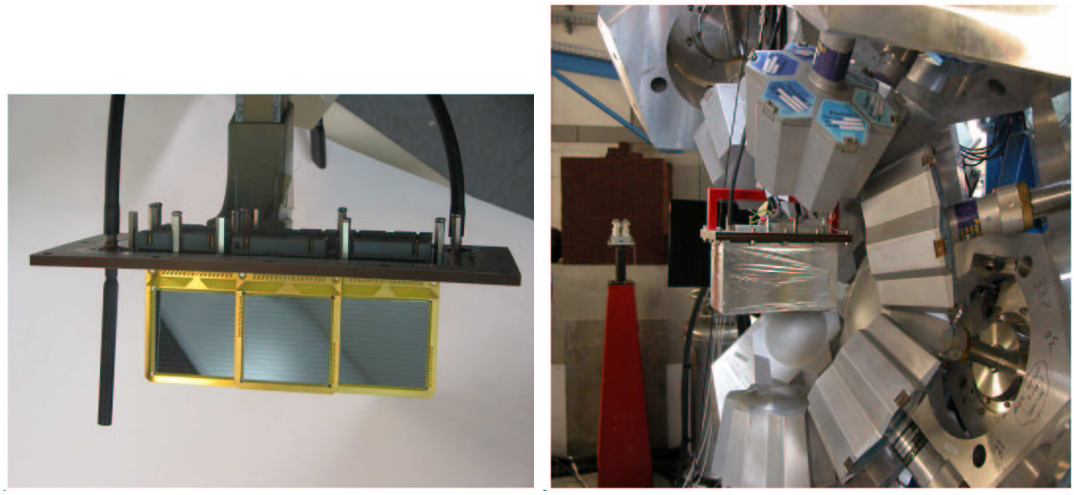

Figure 1.23: A photograph showing the first row of three DSSSD detectors positioned inside the detector holder to ensure a maximum area covered at the final focal plane of the FRS (left) and a photograph of the active stopper box surrounded by the RISING germanium detectors (right).

1.5.2 The Active Stopper

The active stopper [Kum09] used during the α decay experiment consisted of a stack of 6 Micron Semiconductor Ltd [Mic11] W(DS)-1000 5 cm $\times$ 5 cm double-sided silicon strip detectors, each of 1 mm thickness (Fig. 1.23 left). The thickness guaranteed a detection efficiency for α particles of $\sim$ 100%, since the range of an emitted α with an energy between 5 and 7 MeV varies between 20 and 25 μm in silicon. The active stopper box (Fig. 1.23 right) was made up of Pertinax (Phenolic-formaldehyde cellulose-paper) 2 mm thick, with two windows covered by a 20 μm black Polacon C foil [Kum09]. During the experiment the housing of the detector was flushed with cooled nitrogen with a temperature of about 283 K in order to keep the surfaces of the detectors clean and dry and to reduce the thermal excitation of charge carriers across the band gap between valence and conduction band. This action prevented an increase of leakage currents due to the growing defects in the detector lattice caused by heavy ion implantations and helped to keep the detectors fully depleted. The full depletion is mandatory otherwise the energy loss of charged particles in the silicon detector would not be completely detected leading to a systematic error of the measurement.

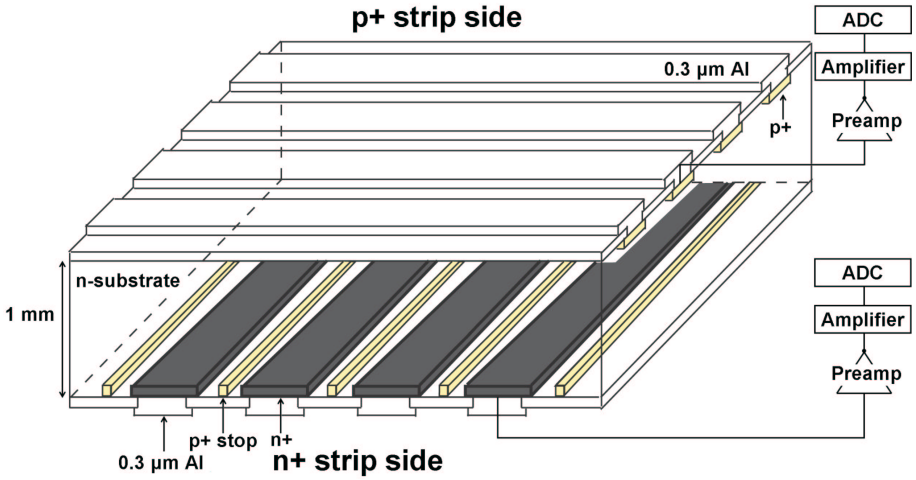

Figure 1.24: Cross-sectional view of a DSSD. The highly doped positively charged or p-type silicon strips and the negatively charged or n-type silicon strips are implanted orthogonally to provide two-dimensional coordinate measurements. Each n+ strip is surrounded by a floating p+ doped implantation to be isolated from any adjacent strips. Aluminium (Al) electrodes are directly coupled on each strip with ohmic contact and are connected to the charge-sensitive preamplifier. The signal is further amplified and is digitalized using a peak-sensing ADC (two electronic branches for p+ and n+ strips are shown, as an example, in the figure).

The DSSDs have been used to determine the energy, position and time for both the implanted secondary fragment and the α-particles following the subsequent radioactive decay and to perform event-by-event position and time correlations. Each detector is divided in 16 front strips and 16 back strips, which provided the x and y coordinates, respectively. Combining the information from the front and the rear strips, it was possible to consider the detector made of 256 pixels, with a sensitive surface of 3.12 mm $\times$ 3.12 mm (Fig. 1.24). In this way, implantations and decays can be spatially correlated within a given pixel. The absolute time of each event was measured with a time stamping system providing a resolution of 25 ns.

The technical complexity related to the active stopper lies in the wide energy range necessary to identify both, the implanted nuclei and the subsequent α-decays. Whereas a fragment implantation may deposit more than 1 GeV when it is stopped in the middle of the DSSSD, an emitted α-particle deposits around

6 MeV. The difficulty was addressed by the use of logarithmic pre-amplifiers coupled with high-gain shaping amplifiers [Kum09]. The *Mesytec* MPR-32 [Mes11] is a logarithmic pre-amplifier with 32 input channels used for the 16 horizontal and vertical strips of a single DSSD. The MPR-32 pre-amplifier is characterized by a linear response in the low energy range (0-10 MeV) followed by a logarithmic amplification at higher energies (10 MeV-3GeV). The linear response recorded the position coordinates (x,y) and the energy deposited from the α-particles. The logarithmic part allowed for the determination of the implantation position. Due to the high energies involved in the slowing-down process, a cross-talk effect may be induced around the pixel of implantation, giving rise to signals (normally of lower energy) in the neighboring strips. In order to minimize the cross-talk effect due to the high energies involved during the implantation process, an implantation threshold has been set. Each MPR-32 pre-amplifier was combined with two *Mesytec* STM-16 NIM-powered amplifiers with 16 channels each. The analogue signals were digitalized using a peak-sensing ADC.

Energy calibration

The energy calibration of the linear range of the logarithmic pre-amplifier, has been performed placing a ^{207}Bi source in front and behind the box containing the DSSDs. A ^{207}Bi source emits monoenergetic conversion electrons due to K and L + M conversion electrons of the 570 keV (E2) and 1060 keV (M4) isomeric transition in ^{207}Pb (see Figure 1.25) [Mar93]. Considering the electronic binding energy, the most abundant electronic energies are 482 keV, 555 keV, 976 keV and 1049 keV, but to obtain the energy deposited in the detector the total energy loss in the different layers of matter (air, box window) $\Delta E \sim 20$ keV was subtracted (Table 1.1). Each peak of the 32 energy spectra of each DSSD detector was individually fitted with a Gaussian function. The resulting centroids were used to perform a linear fit of the energy values. The measured energy resolution was around 20 keV (FWHM) at 980 keV. As an example, the spectrum measured with the strip 7 in x direction (strip 7-X) is shown in Figure 1.26. In addition to this low energy calibration, we used the literature values of the most intense α-decay energies of implanted fragments as further calibration points in the energy range of interest (Fig. 1.27). The measured kinetic energies of the α particles are in excellent

γ energy (keV)	e^- energy (keV)	ΔE in matter (keV)	ΔE^* in Si (keV)
569.6	481.7 [K] 553.8-556.7 [L] 565.8-567.2 [M]	21.4	460.3 532.4-535.3 544.4-545.8
1063.7	975.7 [K] 1047.8-1050.6 [L] 1059.8-1061.2 [M]	19.6	956.1 1028.2-1031.0 1040.2-1041.6

Table 1.1: Calculation of the energy deposition in the silicon detector, from the conversion electrons emitted by the ^{207}Bi source. The emitted γ-rays may transfer its energy directly to one of the most tightly bound electrons causing it to be ejected from the atom (photoelectric effect). The kinetic energy of the emitted electrons depends from the absorbed γ-ray energy and from the electronic binding energy. The energy loss of the electron in the different layers of matter (air, box window) in front of the silicon detector is given.

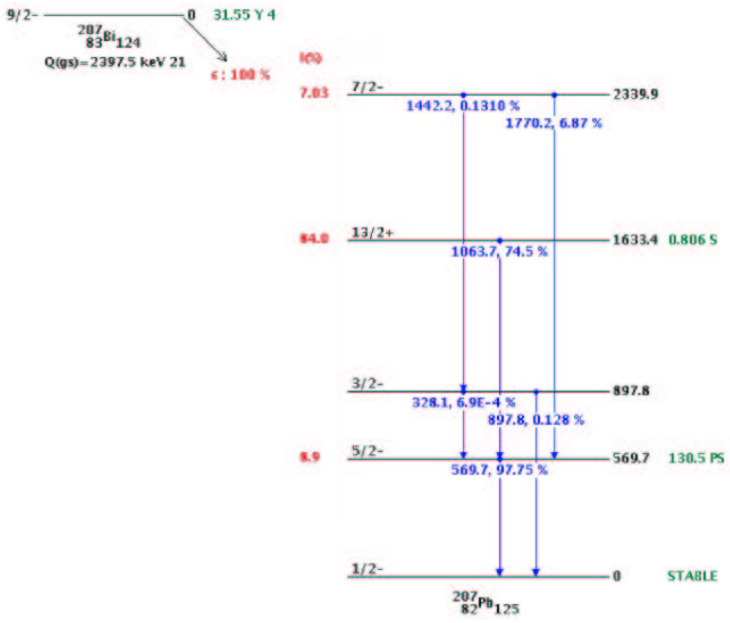

Figure 1.25: Decay scheme for ^{207}Bi nucleus [Mar93], which decays in ^{207}Pb by isomeric transition. The most abundant γ-ray energies are 569.7 keV and 1063.7 keV.

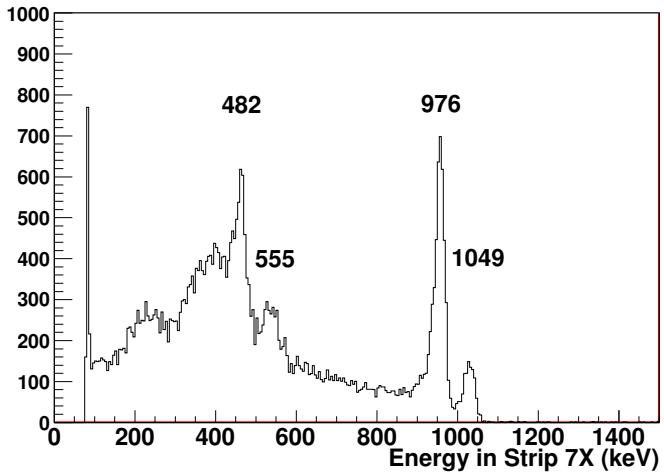

Figure 1.26: Example of the conversion electron spectrum of ^{207}Bi obtained with the strip 7-X of DSSD. The four peaks corresponding to the electron emission energies of 482 keV, 555 keV, 976 keV and 1049 keV were used to perform the energy calibration. The energy loss of the electrons in the different layers of matter (air, box window) in front of the detector was taken into account.

agreement with the well-known literature values, see comparison in Figure 1.29. Table 1.2 summarizes the fragments reaching the final focal plane of the FRS with α decay energy and branching ratio. The table lists also the daughters produced in the α decays. To investigate the response of the logarithmic part of the MPR-32 preamplifier, a pulser was used to simulated high-energy signals. Figure 1.28 shows the different energy range of the calibration method used. The kinetic energies of the α particles are in excellent agreement with the well-known literature values, see comparison in Figure 1.29. Table 1.2 summarizes the fragments reaching the final focal plane of the FRS with α decay energy and branching ratio. The table lists also the daughters produced in the α decays.

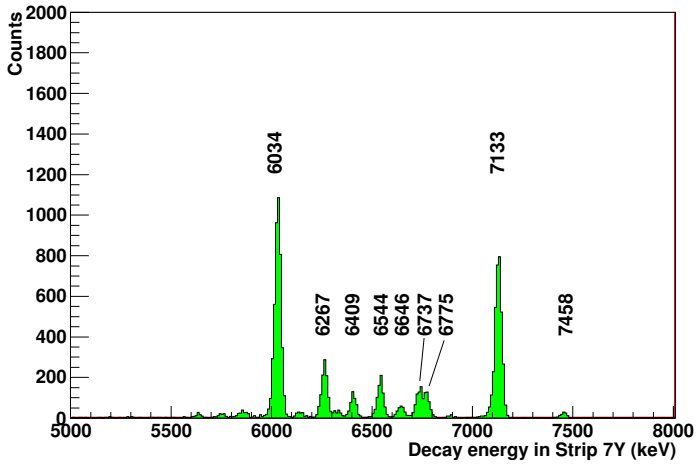

Figure 1.27: α-energy spectrum corresponding to the strip 7-X of DSSD measured for the ^{214}Ra setting. The most instense peaks identified were used in the energy calibration procedure.

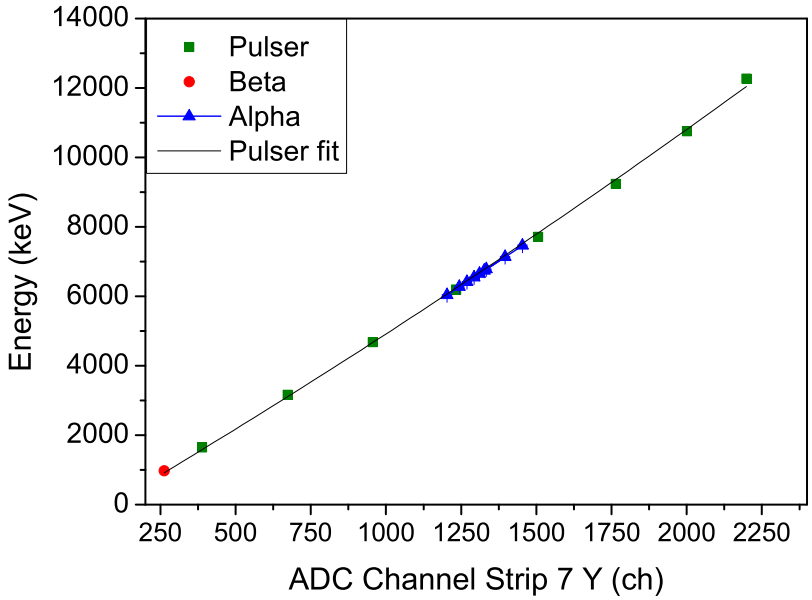

Figure 1.28: Energy calibration plot showing the calibrated points obtained using a ^{207}Bi β source and the literature values of α-decay energies of implanted fragments. The pulser allowed us to study the characteristic energy response of the linear and logarithmic ranges of the MPR-32 [Mes11] preamplifier.

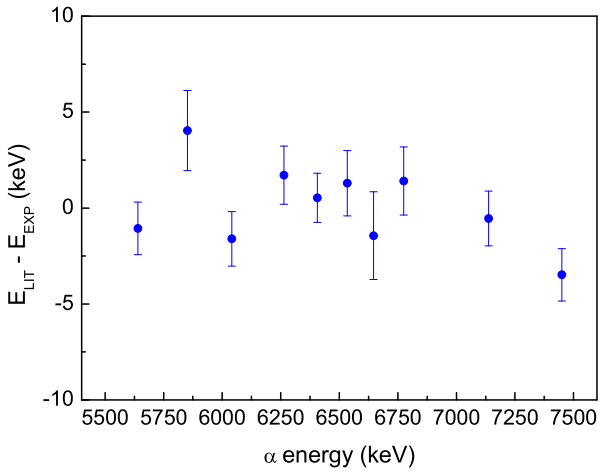

Figure 1.29: Measured kinetic energies of the α particles compared with the values in the literature [ENSDF].

Isotope	α-energy (keV)	Branching ratio (%)
^{210}Po	7450	98.89
	6891.5	0.557
^{209}At	5647	4.1
^{210}At	5524	0.053
	5442	0.05
	5361	0.049
^{211}At	5869	41.8
^{208}Rn	6140.1	62
^{210}Rn	6041	96
	5351	0.0054
^{211}Rn	5783.9	17.3
	5852	9.3
^{212}Rn	6264	99.95
	5583	0.05
^{211}Fr	6534	80
^{212}Fr	6262	16.3
	6383	10.3
	6406	9.4
	6335	4.4
	6343	1.32
^{213}Fr	6775	99.44
^{214}Fr	8478	50.9
	8547	46
	7708	1.1
^{214}Ra	7137	99.74
	6502	0.2

Table 1.2: Measured α decay energies of all implanted α-emitters without identification conditions on the mother fragments. The branching ratios are taken from [ENSDF]

Chapter 2

The New Isomer Tagging System

ITAG (Isomer TAGging detector) is a detector system developed at the FRagment Separator (FRS) for isotope identification by isomer tagging [Far10]. It is placed at the final focal plane of the FRS and detects γ-rays emitted from known isomeric states in fragments implanted into its stopper. By an on-line analysis, the gamma lines pattern are recognized, allowing to identify the isomers and then all the secondary fragments produced. The identification procedure based on isomers can confirm or supply the standard techniques based on the time of flight and the energy loss.

ITAG was successfully tested in March 2009 and was used during the proton scattering experiment (March 2010) and a cross-section measurement around ^{130}Cd (July 2010). ITAG is now available as a standard FRS detector.

2.1 Setup of ITAG

2.1.1 Construction

ITAG consists of two Germanium (Ge) detector electro-mechanically cooled, two plastic scintillators and an exchangeable passive stopper (see Fig. 2.1). The support is 50 cm long and 140 cm wide. A shielding made by 50 mm thick lead layer is foreseen to protect the Ge crystals from radiation coming from the beam line. The Ge crystals are mounted on moving tables to get as close as possible to the stopper maximizing the photopeak efficiency, that ranges from $\sim$ 0.4%

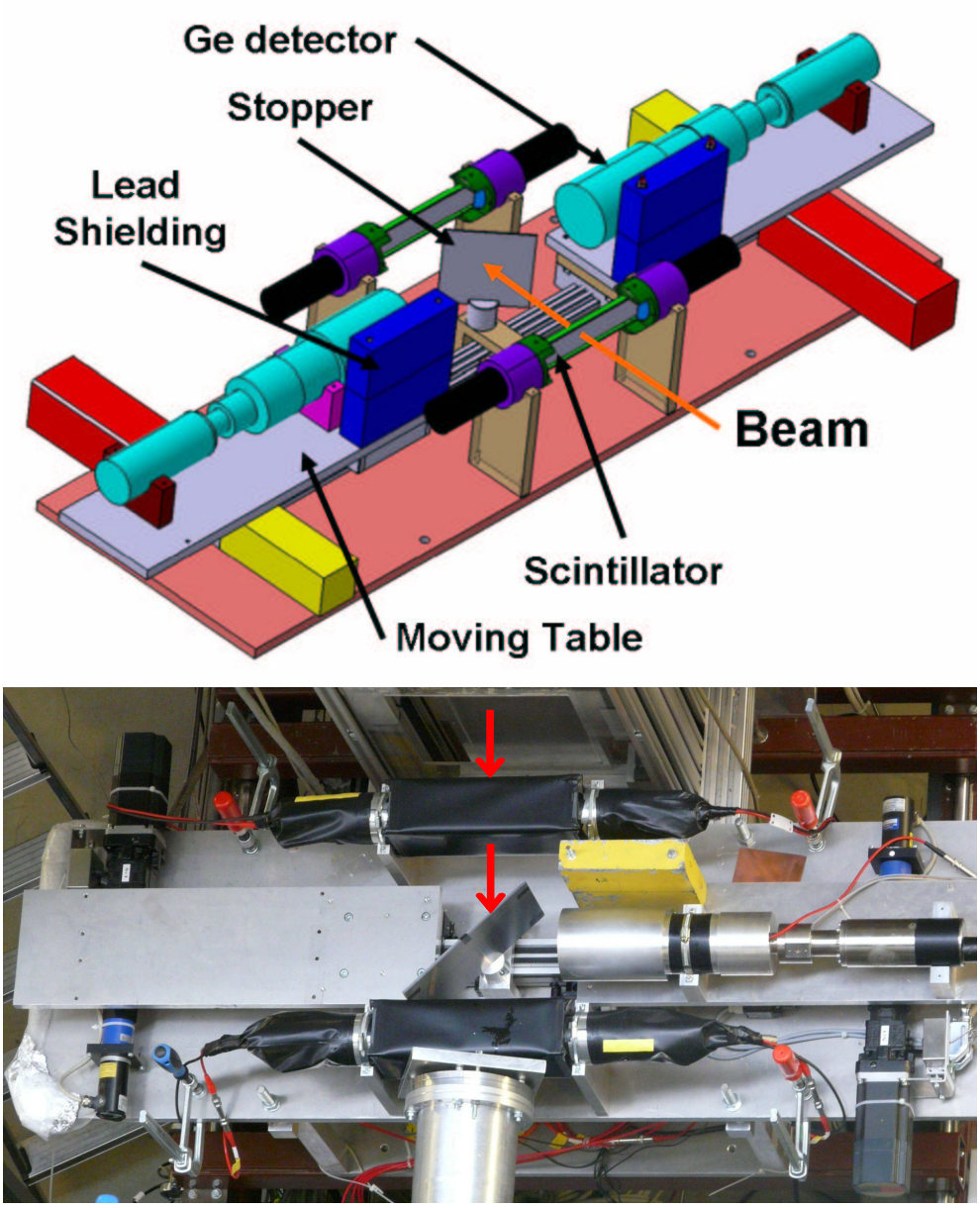

Figure 2.1: Schematic drawing (TOP) and picture (BOTTOM) of the ITAG detector. It consists of two Germanium (Ge) detectors electro-mechanically cooled, two plastic scintillators and an exchangeable passive stopper. The fragment beam passes through the first scintillator and stops inside the passive catcher. The Ge detectors measure the γ-rays emitted from the isomeric de-excitation of the implanted fragments. The Ge crystals are protected by a 50 mm thick lead shielding.

at 90 mm to 0.2% at 150 mm for measured γ-rays of 1.3 MeV (Fig. 2.6). Each Ge-crystal was installed in a specially developed cryostat [Koj08] (Fig. 2.2) which replaces PopTop adaptor [Ort11] (not suitable due to its weak thermal connection within the cold finger path) and improves considerably the heat transfer with the electromechanical cooling engine X-Cooler II produced by ORTEC [Ort11]. The cooling system was tested by scanning the whole volume of the crystal with collimated γ-sources. The energy resolution (FWHM $\approx$1.2 keV at 60 keV) was found to be constant and in good agreement with the expectation, proving the uniformity of temperature and sufficient cooling.
The plastic scintillators (BC420, 274 mm x 45 mm and 5 mm thickness) are used to count the particles and to control their implantation in the stopper. The second scintillator acts as veto detector.

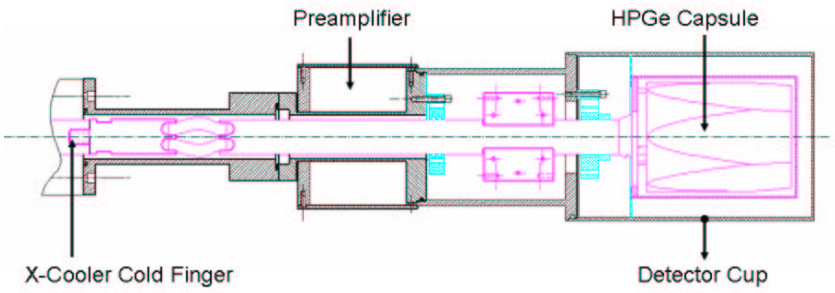

Figure 2.2: Schematic drawing of the cryostat [Koj08]. The encapsulated Ge crystals (HPGe) are installed in a vacuum cryostat, in thermal contact with the cold finger from the X-Cooler. The preamplifier is located near the crystal to minimize the capacitance.

2.1.2 Electronics

Each individual germanium detector has two parallel pre-amplifier outputs: one provides the energy signal and is sent to an amplifier and then goes directly to a peak-sensing ADC; the gate to the ADC is produced from the FRS accepted trigger. The energy signal is processed inside F4 area in order to preserve the energy resolution of the detector. The second output from the germanium pre-amplifier travels from F4 area to the FRS-Electronic Room and is sent to an analogue timing branch composed of a Time Filter Amplifier, a Constant Fraction

Discriminator and a Time-to-Amplitude Converter. The TAC measures the time interval between the arrival of a fragment (trigger signal from the fist scintillator) and the detection of a γ-ray. The TAC range is ~ 8 μs. The output of the CFD is also sent to a scaler. Each germanium detector needs a positive high voltage (the exact value depends on the encapsulated crystal installed and is written on the cryostat. Presently the operational high voltage value is +4000 V) and a preamp power supply. The block diagram of the germanium electronics is shown on Figure 2.3.

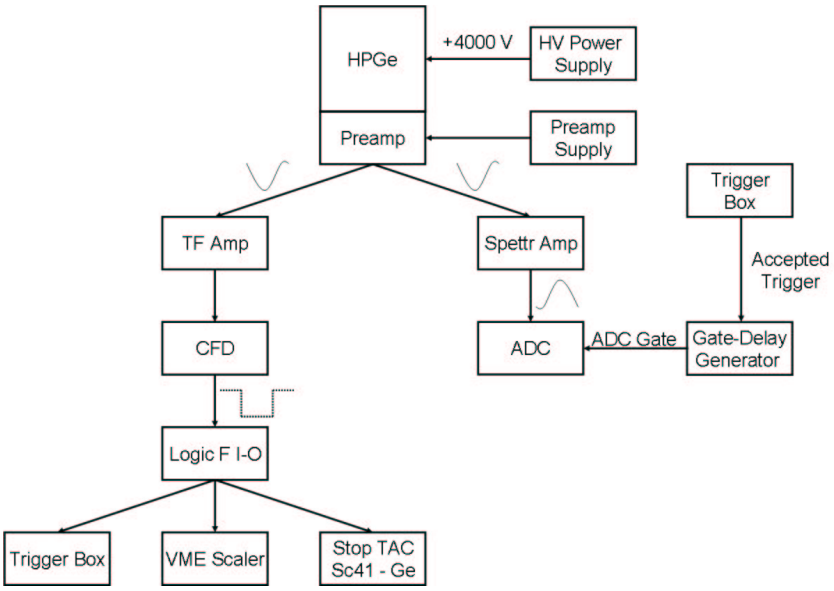

Figure 2.3: Block diagram of the germanium electronics. Each germanium detector needs a positive high voltage (HV) and a preamplifier power supply (preamp). The pre-amplifier outputs provide the energy signal, which is recorded with a peak-sensing ADC after suitable amplification in a Spectroscopy Amplifier (Spettr Amp) and the time signal, which is amplified in a Time Filter Amplifier (TF Amp) and after a Constant Fraction Discriminator is sent in a Time-to-Amplitude Converter (TAC) to measure the time difference between the arrival of a fragment and the detection of a γ-ray.

The electronics required for the scintillators is standard: a splitter divides the anodic signal from each photomultiplier tube, then the two signals travel to FRS-Control Room where one is attenuated, delayed and sent to a QCD to measure the energy loss in the plastic scintillator. The second signal is sent to a CFD,

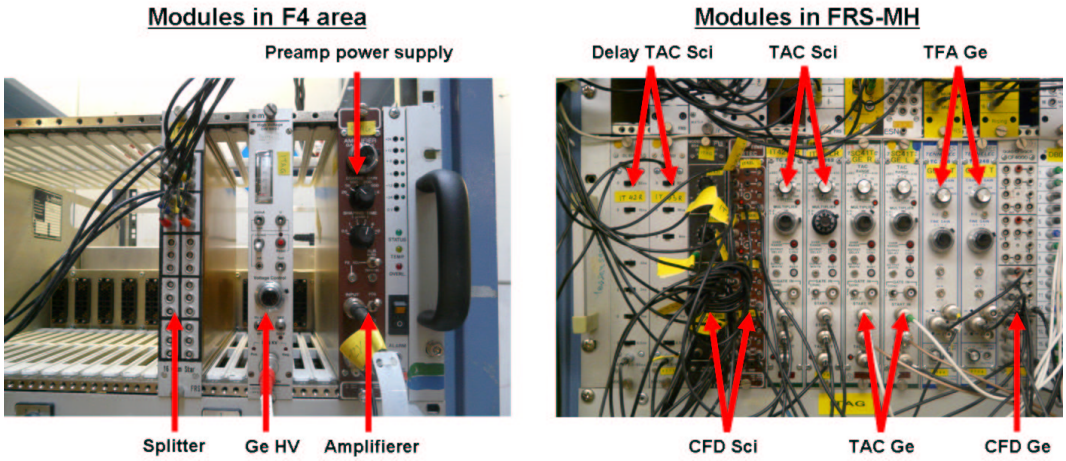

Figure 2.4: Electronic modules need for ITAG and located at the F4 area and at the FRS-Electronic Room.

its outputs produce the coincidence Left-Right. The block diagram of the first plastic scintillator is shown on Figure 2.5.

2.2 Measurements with ITAG

2.2.1 Efficiency

To determine the efficiency for detecting γ-rays, an absolute efficiency calibration of the Ge detector is needed. Due to the large size of the beam spot and the varying implantation depth, it is important to take into account the geometry of the setup and the absorption in the stopper material. Calibration spectra were recorded using ^{60}Co source with known activity placed at different positions along the x-direction of a 14 mm thick PVC stopper and then varying the distance detector-stopper (Fig. 2.6 left panel). The energy dependence of the efficiency was measured using a ^{152}Eu source with known activity. The results are shown in Fig. 2.6 right panel.

2.2.2 Commissioning experiment

During an FRS000 experiment, a primary $^{96}Ru^{42+}$ beam at an energy of 500 MeV/u and a maximum intensity of $\sim 10^5$ ions/s impinged on a 2.5 g/cm^2 Be

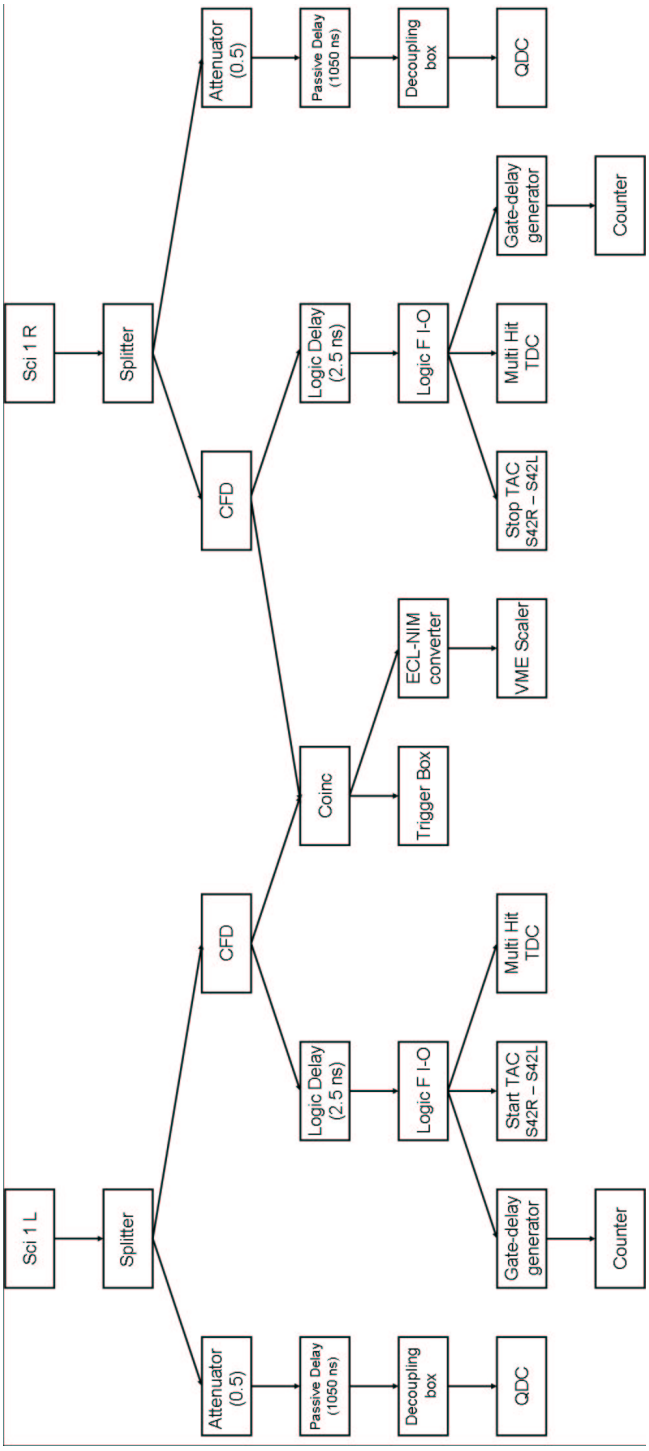

Figure 2.5: Block diagram of the electronic of the first plastic scintillator of the ITAG setup.

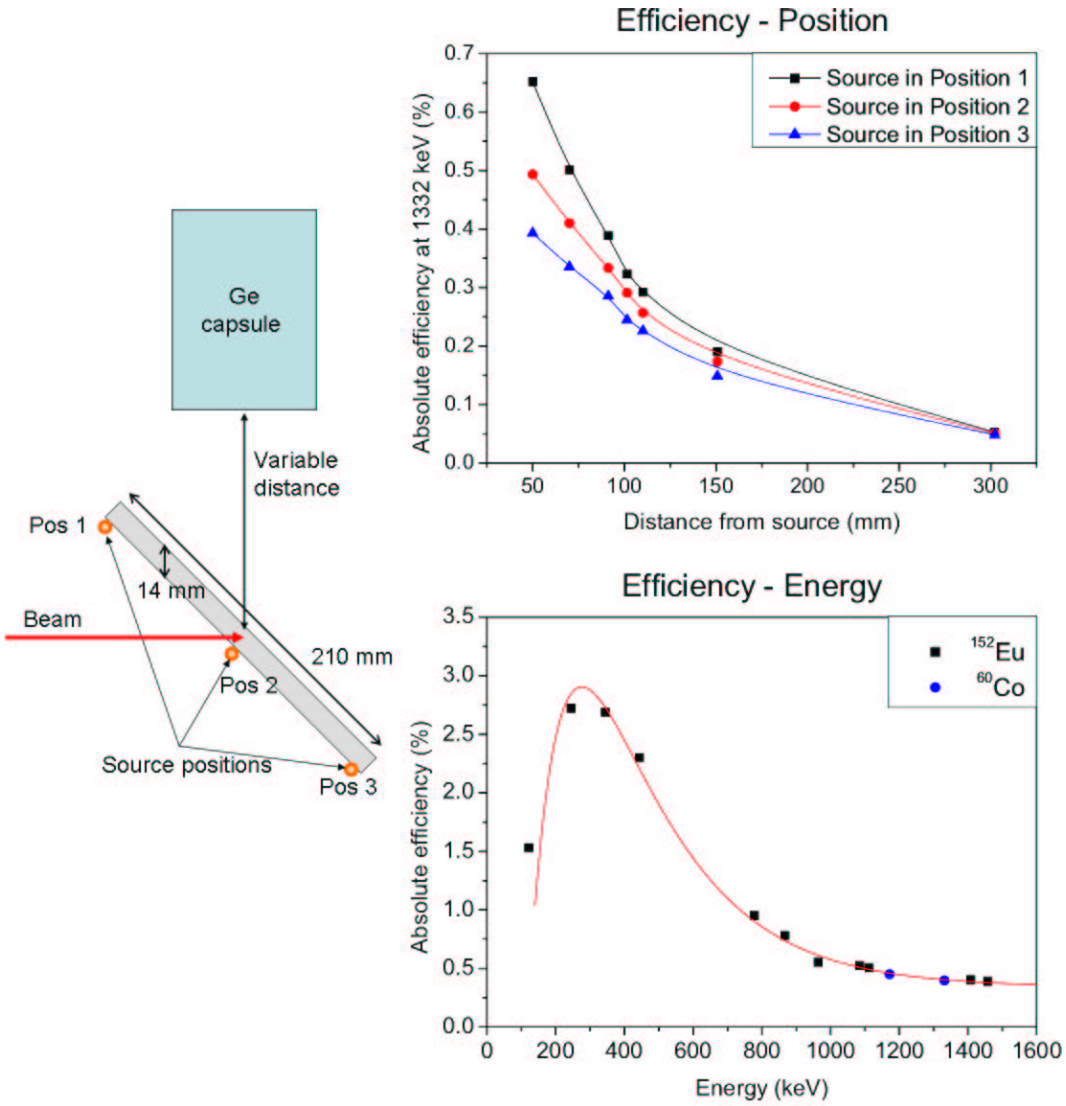

Figure 2.6: Setup for the efficiency measurement (left panel). The measured efficiency as a function of the position (top panel) and efficiency as a function of the energy at 50 mm from source (lower panel).

target. The FRS was used in achromatic mode and optimized for the transmission of ^{94}Ru ions. The ions were slowed down and implanted into the 3 mm thick Al stopper of ITAG. The identification of the reaction products was performed using the standard time of flight and energy loss techniques and the ITAG.

- Total counting rate at S2 : 4.5kHz
- Total counting rate at S4 : 2.0 kHz

Two isomers (^{90}Mo and ^{92}Tc) were identified using this procedure and the results are listed in the Table 2.1.

	Production	γ-counts	γ-lines (MeV)	$T_{1/2}$ (μs)
^{92}Tc	1.3×10^5	95	214.2 ± 2.9	1.04 ± 0.3
^{90}Mo	8.6×10^4	180	809.9 ± 3.0 947.7 ± 3.0 1053.9 ± 3.1	1.13 ± 0.16

Table 2.1: Measured γ-energy values measured in coincidence with the selected isotope. The half-life is obtained from the time difference between the implantation of the isomer and the detection of the γ-ray.

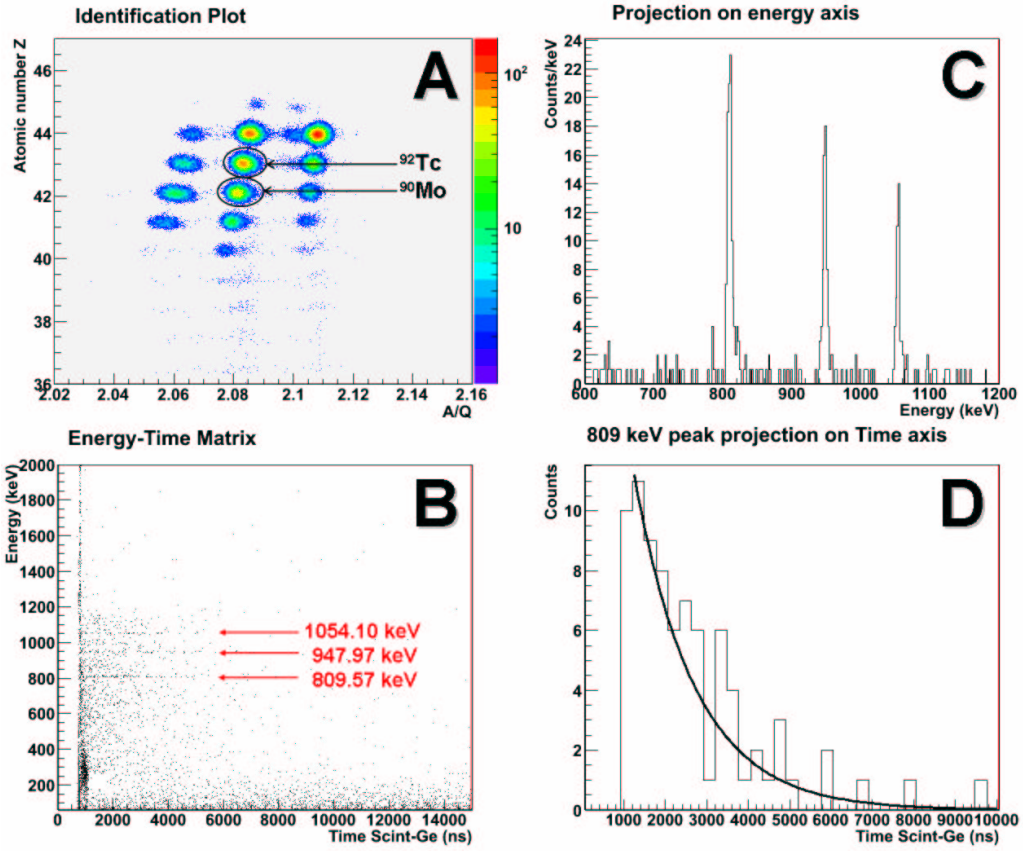

Figure 2.7: On-line analysis steps: measured identification matrix (A); ^{90}Mo γ-energy and time correlation matrix (B); ^{90}Mo gamma lines (C) and ^{90}Mo half-life (D).

Chapter 3

Discovery of 63 New Isotopes

In the recent years the fragmentation reactions have demonstrated to be a powerful tool for the production of radioactive secondary beams and studies of the most exotic nuclei. The new generation of in-flight radioactive beams facilities with a set of novel experiments have significantly extended the knowledge of nuclear physics. Several milestones of the nuclear physics have been achieved like the production of the doubly magic nuclei ^{100}Sn [Schn94], ^{78}Ni [Enge95] which are available in quantities suitable for more detailed spectroscopic studies [Hin10].

In the mid 90's, FRS experiments set the scientific frontiers for medium mass neutron-rich isotopes [Ber94]. In these experiments more than 120 new isotopes have been discovered, and with these achievements a new research activity for projectile fission studies was launched [Arm04]. The origin of heavy elements in the r-process is one of the outstanding problems in nuclear astrophysics [Cow06]. Its understanding requires improved nuclear physics data, like masses (Q-values) and half-lives.

Large progress have been achieved very recently with intense ^{238}U beam at the new Radioactive Beam Factory in RIKEN [Ohn10] and experiments at the FRS and ESR facilities [Kur06, Alv10, Che10]. In this work we report of the discovery of 63 neutron-rich new isotopes in the element range Nd-Au.

3.1 Experimental Setup

The experiment was performed at the SIS synchrotron, which delivered a 1 A GeV ^{238}U beam with spills characterized by 0.5-2 s extraction times and a repetition period of 2-4 s. The primary beam, with an intensity of about 2×10^9 ions/spill, impinged on a 1.6 g/cm^2 thick beryllium target placed at the entrance to the FRS (see Figure 1.7). The reaction products were separated by the FRS in an achromatic mode. The FRS spatially separates with two stages of magnetic selection (Bρ) and an atomic energy loss in two degraders located at the first (F1) and second (F2) focal plane. With detectors a full identification of reaction products in-flight was obtained with respect to their nuclear charge Z and mass A. The slowing down was performed in two aluminum degraders. However, to increase the yield of bare fragments, niobium and iron foil strippers were placed behind the first and second degrader, respectively. The time-of-flight measurement was performed between two pairs of plastic scintillator detectors, one located at the central focal plane and the other one at the final focal plane. The typical flight time was around 160 ns and the achieved resolution $\sigma_T \approx 30$ ps. Four TPC detectors, two placed at the central and two at the final focal plane, provided tracking information (position and angle of each detected ion). At the exit of the spectrometer, two ionization chambers (MUSIC) were mounted with a 104 mg/cm^2 copper strippers placed in front of each. The MUSIC detectors delivered the energy deposition signal of fragments, thus providing the identification of the atomic number. The implantation point located at the final focal plane was surrounded by the RISING germanium detector setup [Pie07]. The isomer tagging technique was applied in order to verify the identification of the reaction products. In this experiment several Bρ settings of the FRS were used, which were chosen to yield optimum beam intensities for neutron rich Dy, Os, Pt and At isotopes, see Figure 3.1. Other field settings were used to confirm the particle identification with known μs-isomers. The total time dedicated to each fragment setting and the total dose of primary beam achieved are given in Table 3.1.

Reference fragment	Measurement Time	Total Dose
$^{226}_{85}\mathrm{At}^{85+}$	24.5 h	$3.4 \cdot 10^{13}$
$^{224}_{85}\mathrm{At}^{85+}$	1.5 h	$2 \cdot 10^{12}$
$^{205}_{82}\mathrm{Pb}^{82+}$	10.5 h	$1.0 \cdot 10^{13}$
$^{207}_{78}\mathrm{Pt}^{78+}$	21.5 h	$2.5 \cdot 10^{13}$
$^{202}_{76}\mathrm{Os}^{76+}$	52 h	$7.5 \cdot 10^{14}$
$^{198}_{76}\mathrm{Os}^{76+}$	4 h	$5.0 \cdot 10^{12}$
$^{194}_{76}\mathrm{Os}^{76+}$	1.5 h	$2.3 \cdot 10^{12}$
$^{180}_{72}\mathrm{Hf}^{72+}$	4.5 h	$6.2 \cdot 10^{13}$
$^{167}_{72}\mathrm{Ho}^{72+}$	3 h	$3.6 \cdot 10^{12}$
$^{172}_{66}\mathrm{Dy}^{66+}$	15 h	$2.1 \cdot 10^{13}$
$^{170}_{66}\mathrm{Dy}^{66+}$	6 h	$6.5 \cdot 10^{12}$

Table 3.1: The different reference fragment settings investigated during the experiment. Most of the beam time was devoted to the production of neutron rich isotopes with Dy, Os, Pt and At settings. Other field settings were used to confirm the particle identification with known μs-isomers. The total time dedicated to each fragment setting and the total dose of primary beam achieved are listed in the table.

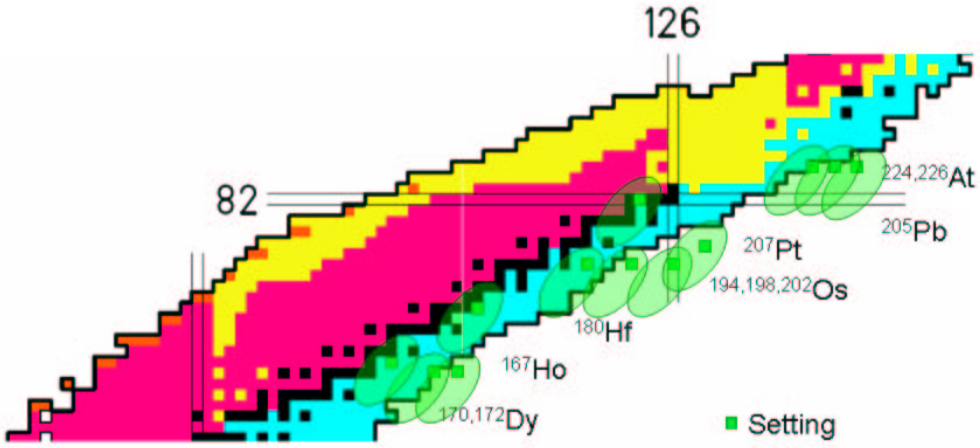

Figure 3.1: Part of the chart of nuclides indicating the regions covered by the present experiment. The search for the new isotopes was done using different field settings of the FRS: ^{170,172}Dy, ^{194,198,202}Os, ^{207}Pt and ^{224,226}At isotopes. The settings of ^{167}Ho, ^{180}Hf and ^{205}Pb verified the identification in-flight.

3.2 Identification of New Isotopes

The identification of heavy neutron-rich projectile fragments is a challenging task. Two issues have to be overcome to obtain an unambiguous identification:

- contamination due to charge states produced inside the FRS;
- loss in resolution in the energy-deposition measurements with the ionization chambers (MUSIC) due to stochastic changes of charge-states within the gas.

Both problems are mainly caused by the different ionic charge states populated by the heavy fragments. The charge state of the ion can change within the active region of the ionization chamber, and this effect contributes to the broadening of the energy-deposition signal. The use of a profiled aluminium degrader, placed at the central focal plane of the FRS, and the combined measurement of the energy deposition of the fragments in two MUSIC chambers with a copper stripper foil in front of each. The data recorded in each setting were processed by using

the combination of time-of-flight, position and energy-deposition described in Chapter 1. Figure 3.2 illustrates the correlation between the measured atomic number Z in the two MUSIC detectors for a setting of the FRS centered on ^{180}Hf. The probability of an ion being fully-stripped at least in one chamber was optimized with a stripper Cu foil (104 mg/cm^2) placed in front of each. The observed pattern for each spot in Figure 3.2 is due to the atomic charge changing measured in both chambers. For each element, the energy-deposition signal in the horizontal distribution corresponds to those ions which carry no electrons in the first chamber (MUSIC1). The corresponding vertical distributions represent the fully-stripped ions at the second chamber (MUSIC2). The overlap of both represents the fully-stripped ions in the two MUSIC chambers. A tilted line passing through the different cores corresponds to those events for which the same atomic charge was measured by the two chambers. The resolution for the nuclear charge $\sigma_Z = 0.24$ allowed to clearly all discriminate the different elements up to uranium (see Figure 1.15 left panel). Only ions showing a full energy deposition in both detectors were chosen for further analysis, thus rejecting ions with different charge states in both MUSIC detectors or reaction products created in the material of the detector. In the second step a distribution of the reconstructed nuclear charge as a function of the energy loss of the ions in the degrader located at the central focal plane was created. This allowed to determine the ionic charge state of a fragment within the FRS by the measuring the energy loss in the degrader, as described in in Section 1.4.1. Unambiguous identification of the transmitted nuclei required additional selection based on the analysis of the position of the fragments at the final focal plane. Figure 3.4 shows the selected isotopes of Hf for the magnetic setting of the FRS centered on ^{180}Hf.

Several redundant measurements of energy loss in matter, positions, and time-of-flights were performed to obtain an unambiguous isotope identification. This was possible also due to the good atomic mass resolution $\sigma_A = 0.17$.

In the particle identification plot (Fig. 3.5), all isotopes covered in the magnetic field settings centered on ^{172}Dy and ^{194,198,202}Os are displayed with the full statistics and all the separation criteria applied. The red solid line indicates the border of the discovered new isotopes. From this analysis, the measured counts for each isotopes is deduced for the cross-section determination described in the

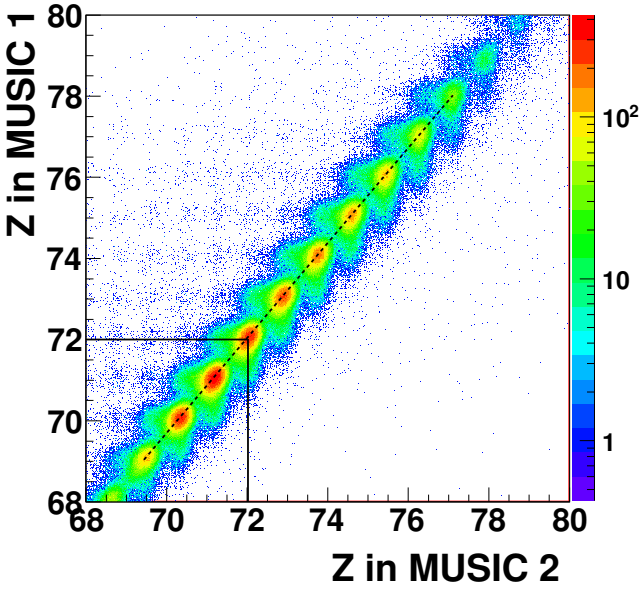

Figure 3.2: Correlation of the measured atomic number Z in the two ionization chamber for a field setting of the FRS centered on ^{180}Hf. The dashed line indicates the events with the same nuclear charge ($Z = q$) measured by the two chambers.

next Section. To demonstrate the number of new isotopes more clearly than seen in the two-dimensional scatter plot, for each element the projection on the A/q axis was done. Figures 3.6 and 3.7 display the isotopes measured during the field settings centered on ^{172}Dy and Figures 3.8 and 3.9 display the isotopes produced during the field settings centered on ^{194,198,202}Os. The mass of the hitherto unobserved isotopes is indicated on the plots. In total, 63 new isotopes have been unambiguously identified and their production cross-section measured.

The progress achieved with the discovery of 63 new isotopes in a relative short FRS experiment represents a wide potential for nuclear structure and astrophysics. In addition, this experiment has also confirmed the new isotopes reported recently. The results of the present experiment have been possible due to the improved separation and particle identification at the FRS where the γ-tagging technique had a significant contribution. Unambiguous fragment identification is a key for these investigations at the frontiers. The next step after the discovery phase is to investigate the basic properties of the the new nuclides. The first

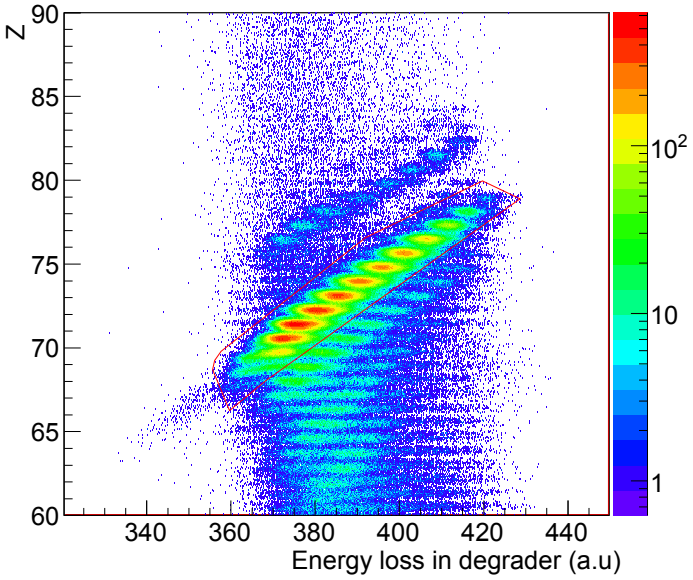

Figure 3.3: The selection done on the energy loss of the fragments in the degrader located at the central focal plane for a setting of the FRS centered on ^{180}Hf. The red line shows the selection of the bare fragments which are further analyzed.

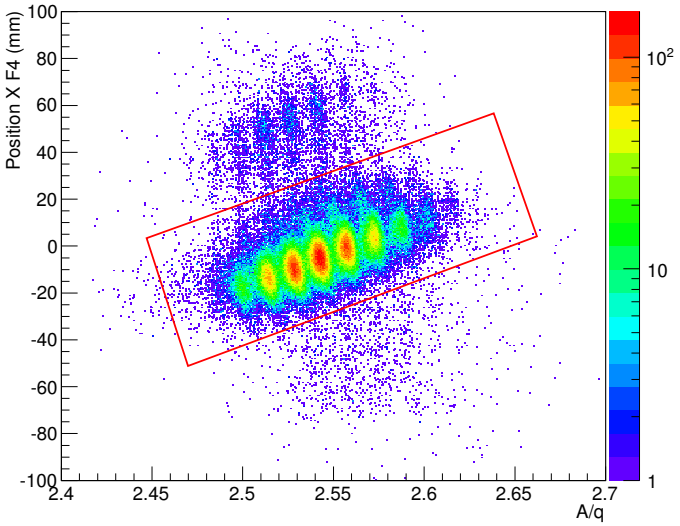

Figure 3.4: Horizontal position of the Hf isotopes at F4 as a function of their A/q ratio. The condition implemented to select the centered isotopes is shown by the red rectangle.

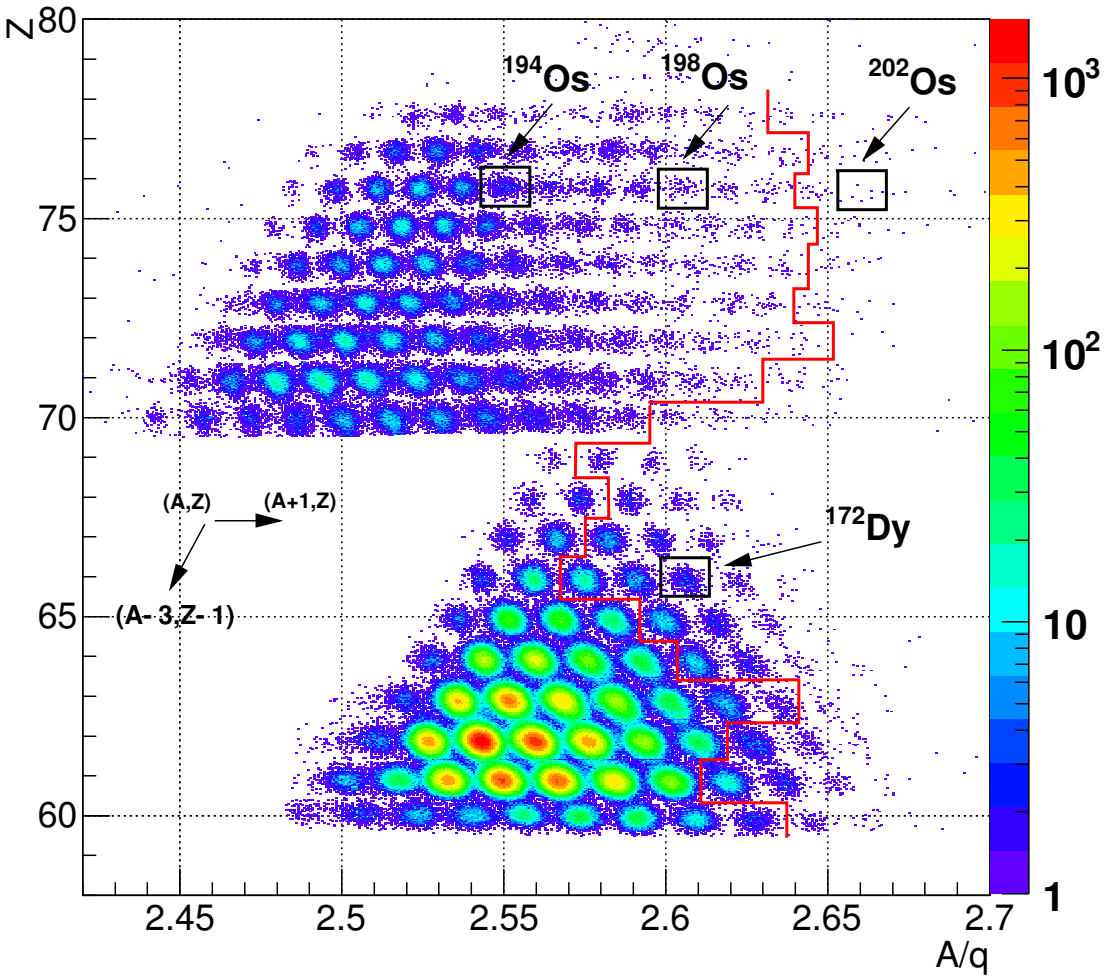

Figure 3.5: Particle identification (nuclear charge Z versus A/q ratio) for the full statistics recorded during the field settings centered on reference fragments $^{194}Os^{76+}$, $^{198}Os^{76+}$, $^{202}Os^{76+}$ and $^{172}Dy^{66+}$.

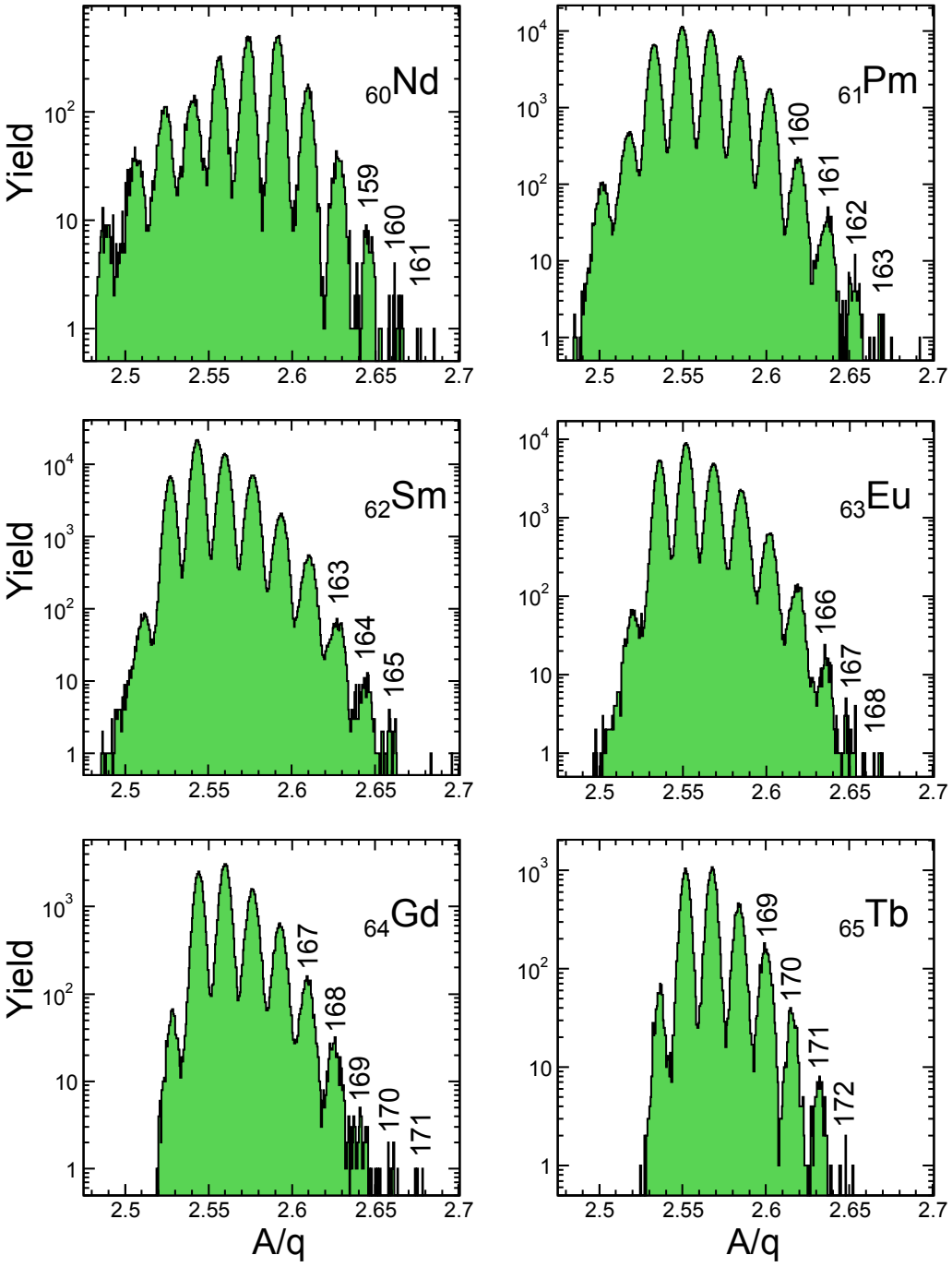

Figure 3.6: Projection on the A/q axis of the identification plot constructed by selection of a specific element from the range covered in the Bρ setting of the FRS centered on ^{172}Dy. The mass number of the hitherto unobserved isotopes is indicated. In total 39 isotopes have been discovered.

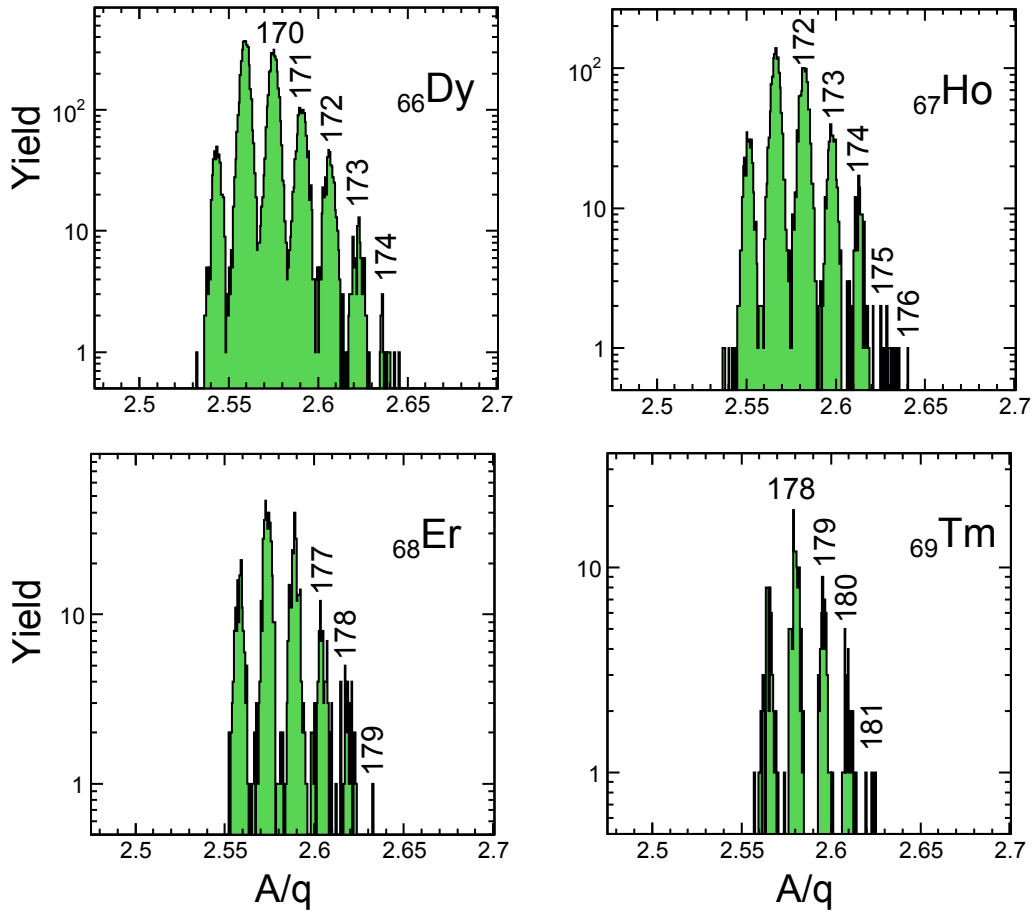

Figure 3.7: Projection on the A/q axis of the identification plot constructed by selection of a specific element from the range covered in the Bρ setting of the FRS centered on ^{172}Dy. The mass number of the hitherto unobserved isotopes is indicated. In total 39 isotopes have been discovered.

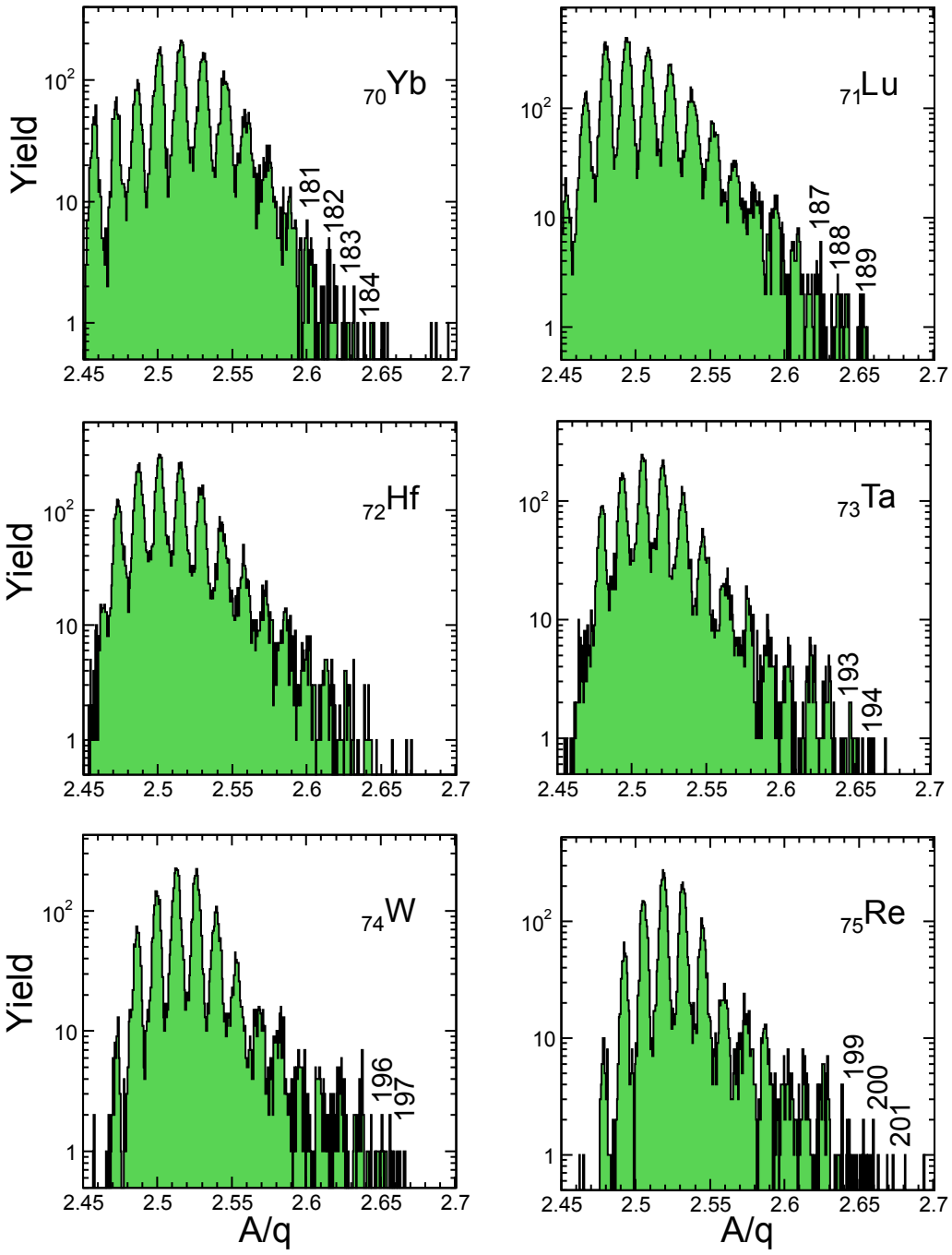

Figure 3.8: Projection on the A/q axis of the identification plot constructed by selection of a specific element from the range covered in the Bρ setting of the FRS. The results are the superposition of data recorded with field settings centered on ^{194}Os, ^{198}Os and ^{202}Os. The mass number of the hitherto unobserved isotopes is indicated. In total 24 new isotopes have been discovered.

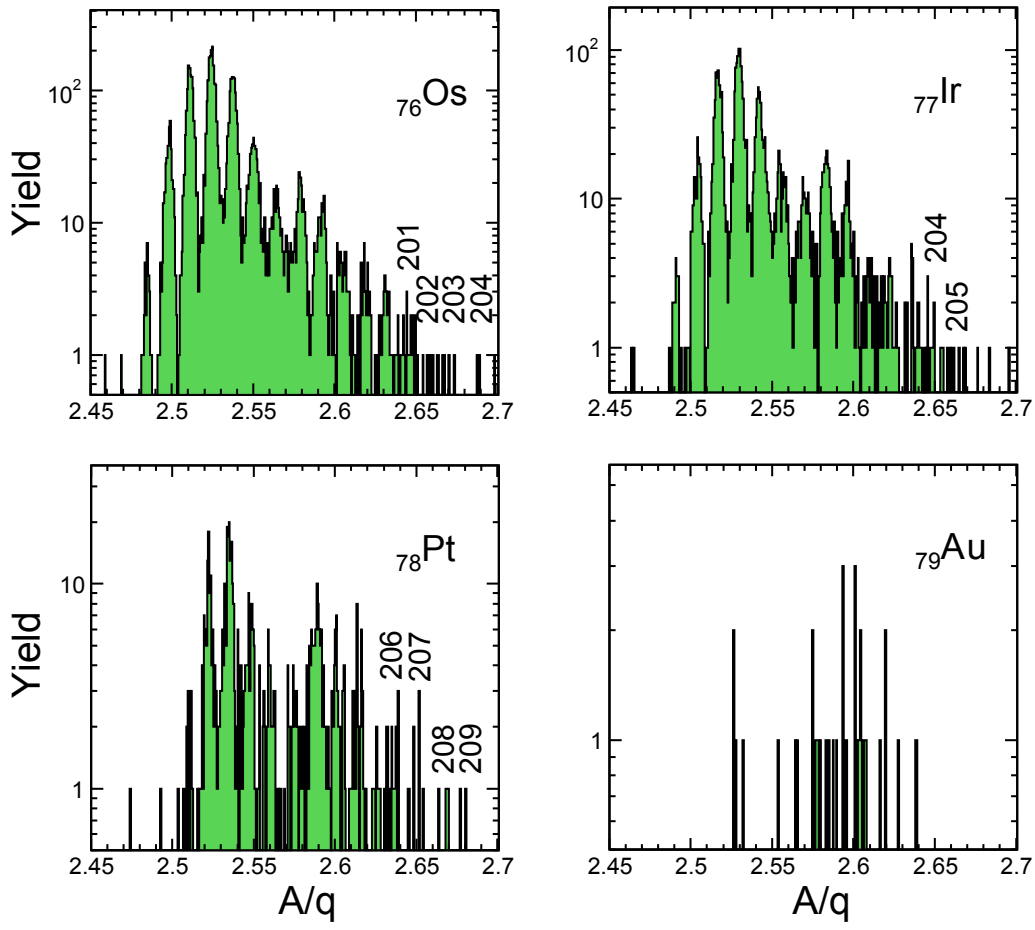

Figure 3.9: Projection on the A/q axis of the identification plot constructed by selection of a specific element from the range covered in the Bρ setting of the FRS. The results are the superposition of data recorded with field settings centered on ^{194}Os, ^{198}Os and ^{202}Os. The mass number of the hitherto unobserved isotopes is indicated. In total 24 new isotopes have been discovered.

property of importance is the determination of the production cross section. They are highly relevant to plan further studies with the field of discovered nuclei and contribute to the basic understanding of projectile fragmentation reactions.

3.3 Determination of the Production Cross-sections for the Discovered Isotopes

The production cross-sections σ_f are determined by several different experimental contributions: the measured yield N_f of single isotopes detected at the final focal plane, the primary beam intensity N_p, the number of atoms in the target N_t and correction factors due to the limited transmission, the dead-time of the data acquisition system and the secondary reactions in the matter (target, degraders and detectors) summarized with the term f_{corr}:

$$\sigma_f = \frac{N_f}{N_p \cdot N_t \cdot f_{corr}}. \tag{3.1}$$

The measured yield N_f are directly deduced from the identification matrices in the previous Section. They are shown for the different field settings and different isotopes in Figure 3.10, 3.11, 3.12 and 3.13.

The number of target atoms per unit area N_t is given by:

$$N_t = \frac{N_0 t}{A_t} \tag{3.2}$$

where N_0 is Avogadro number, t is the areal weight of the target and A_t is the mass number of the target material. The areal weight was measured with a microgram scale and with mechanical sensors. The target non-uniformity was controlled by a commercial target scanner [Tar11]. The areal weight of the applied target was 1627 ± 1 mg/cm^2.

The intensity of the primary beam is measured by means of the secondary electron transmission monitor (SEETRAM) which provides the number of projectiles for each spill. The principle of the SEETRAM detector is that the secondary electron yield is strictly proportional to the inelastic stopping power of the incoming ions [Rot90]. In reference [Rot90] this statement has been experimentally demonstrated for different projectiles, from proton to uranium, over four

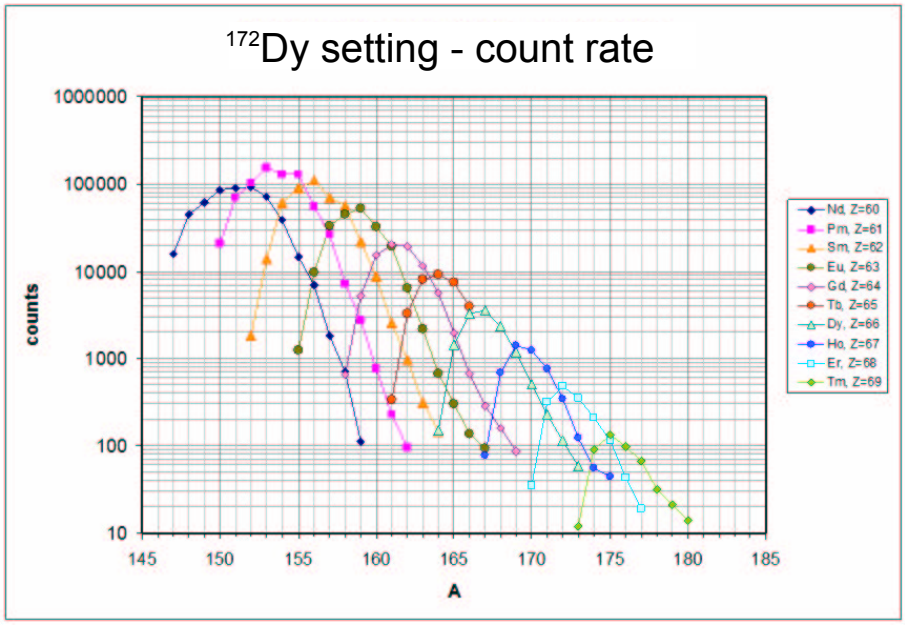

Figure 3.10: Measured yields of the different fragments obtained with the Bρ field setting of the FRS centered on $^{172}Dy^{66+}$ ions.

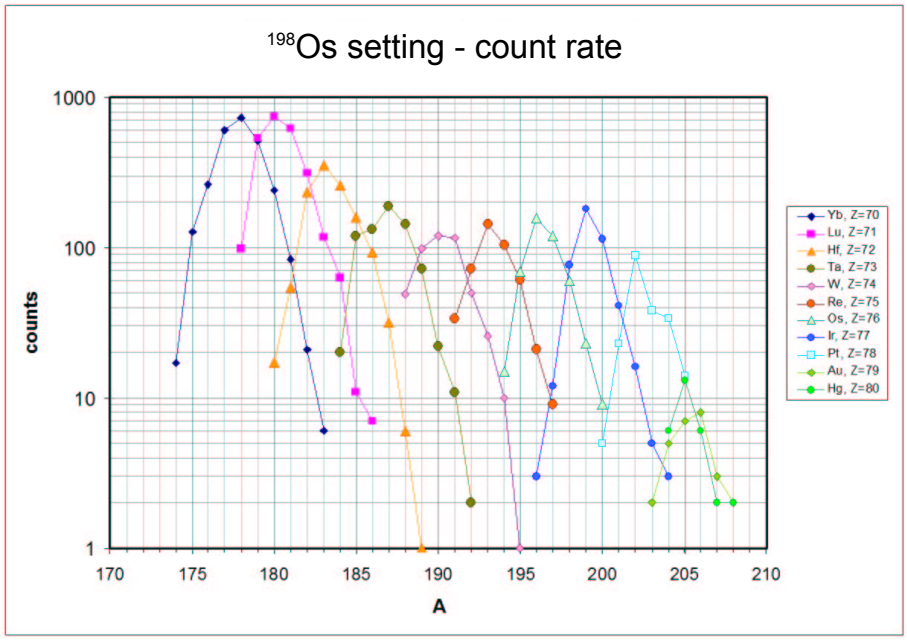

Figure 3.11: Measured yields of the different fragments obtained with the Bρ field setting of the FRS centered on $^{198}Os^{76+}$ ions.

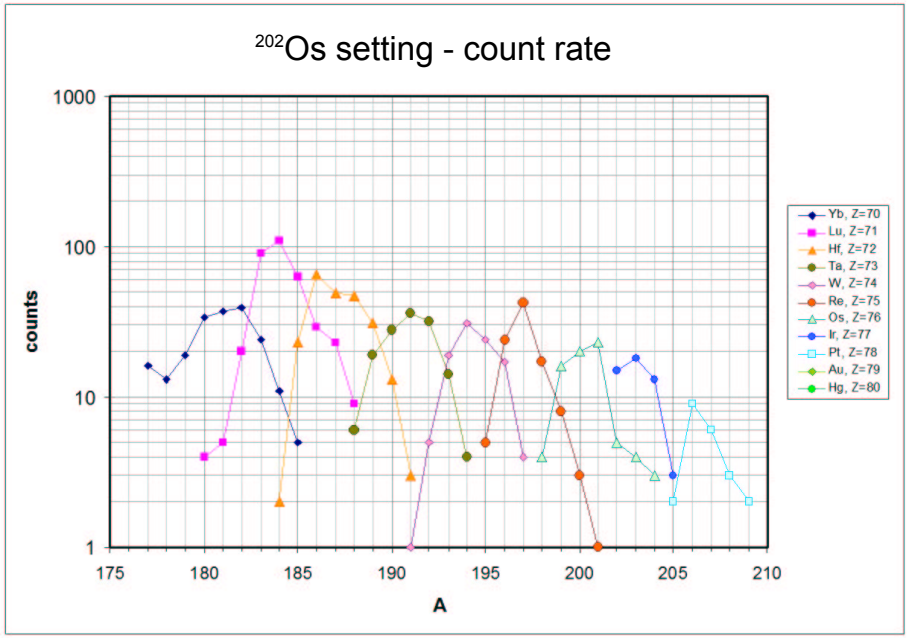

Figure 3.12: Measured yields of the different fragments obtained with the Bρ field setting of the FRS centered on $^{202}Os^{76+}$ ions.

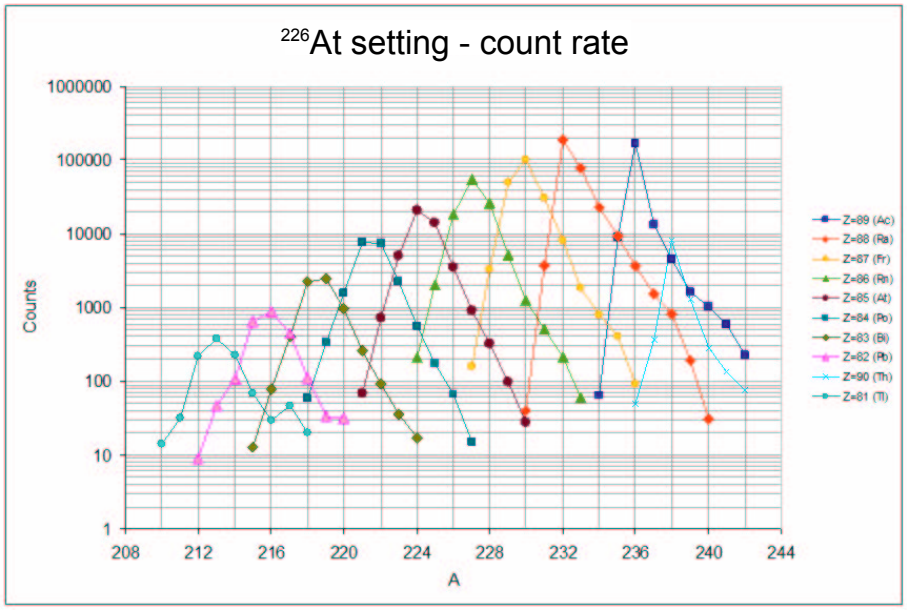

Figure 3.13: Measured yields of the different fragments obtained with the Bρ field setting of the FRS centered on $^{226}At^{85+}$ ions.

orders of magnitude. Nevertheless, the calibration of the SEETRAM detector has to be verified especially in experiments where precise cross-section measurements are performed. In this experiment the SEETRAM calibration was verified with a plastic scintillator (SCI1) detector in coincidence. Both detectors recorded the number of uranium ions entering the FRS. For this measurement, the beam intensity was strongly reduced and varied from a few thousands to $2 \cdot 10^6$ projectiles per spill. In this calibration measurement the maximum spill length of about 10 seconds was selected. In Figure 3.14 the counts of both detectors are shown. Over the operating range of the scintillator detector, both signals are linearly correlated, i.e., the slope yields the calibration factor.

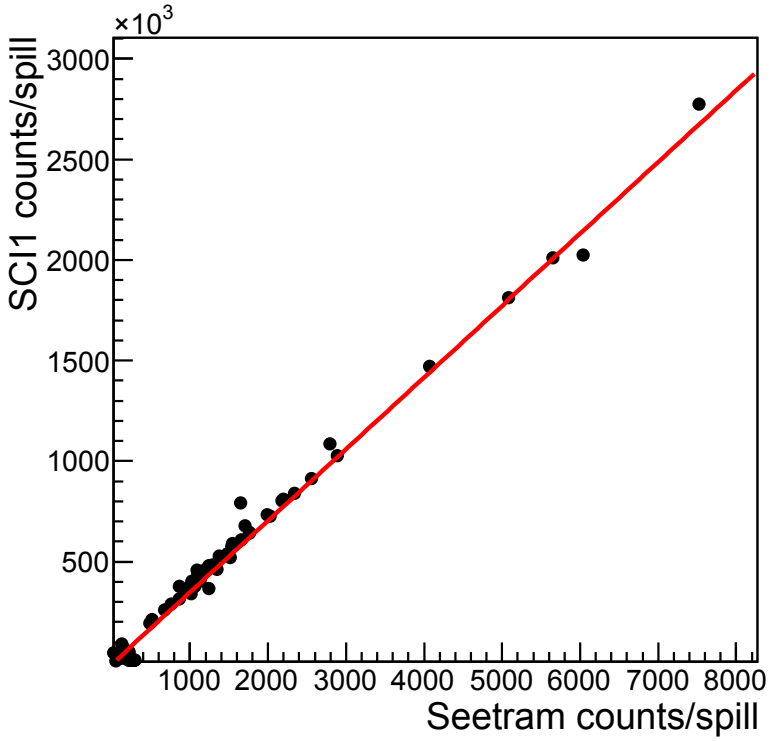

Figure 3.14: Number of ^{238}U ions measured with the scintillator in coincidence with the SEETRAM detector. Each data point corresponds to the counts accumulated during one spill. The full line represents a linear fit to the data.

Also for the measured rate N_f, the mentioned corrections have to be determined. The measured yields at F4 correspond only to fully-stripped ions. Therefore, the population of other charge states have to be included after each dipole stage of the FRS. In previous experiments, the charge states population

have been measured and the results were implemented in the computer codes GLOBAL [Sch98] and CHARGE [Sch98]. Based on the accurate measurements both programs are very reliable (few percent accuracy) in this energy range. Hence, the calculations of charge state distribution for the different fragments emerging from matter, were performed with these theoretical codes. The optical transmission through the FRS was taken into account by computer simulations using MOCADI [Iwa97] calculating the phase-space population of the fragment beam and the complete FRS setup including apertures, slits and matter. The transmission losses due to secondary reactions are also taken into account with MOCADI simulations.

The dead-time of the data acquisition and detectors is also an important correction for precise cross-section measurements. It is defined as the time elapsed after one event is registered by the detection system in which it is not able to record another incoming event. In each event readout we registered with scalers the number of 'free triggers' and the number of 'accepted triggers'. The free and accepted triggers represent all the events coming from the scintillator detector and the number of the fully-processed events including all hardware conditions, respectively. The ratio between these two numbers is the overall dead-time of the detection system. During the experiment the values of the dead-time ranged from 5% for the most exotic nuclides up to 30% for fragments produced with high rates.

The correction factor f_{corr} including all the discussed contributions has been separately determined for each isotope. The measured cross-sections for each element are presented in Figures 3.15, 3.16 and 3.17. In addition the experimental data from other experiment [Ber03, Ber06] are shown to demonstrate the smooth transition from the literature values to the new data. The experimental data are compared to the theoretical models ABRABLA [Gai91]. The agreement with the ABRABLA predictions is excellent in the region where theoretical values are available. The ABRABLA code is based on Monte Carlo methods which gives practical restrictions to low cross-sections. Note that we reached with our present experiment the sub-nanobarn level in the production cross-sections.

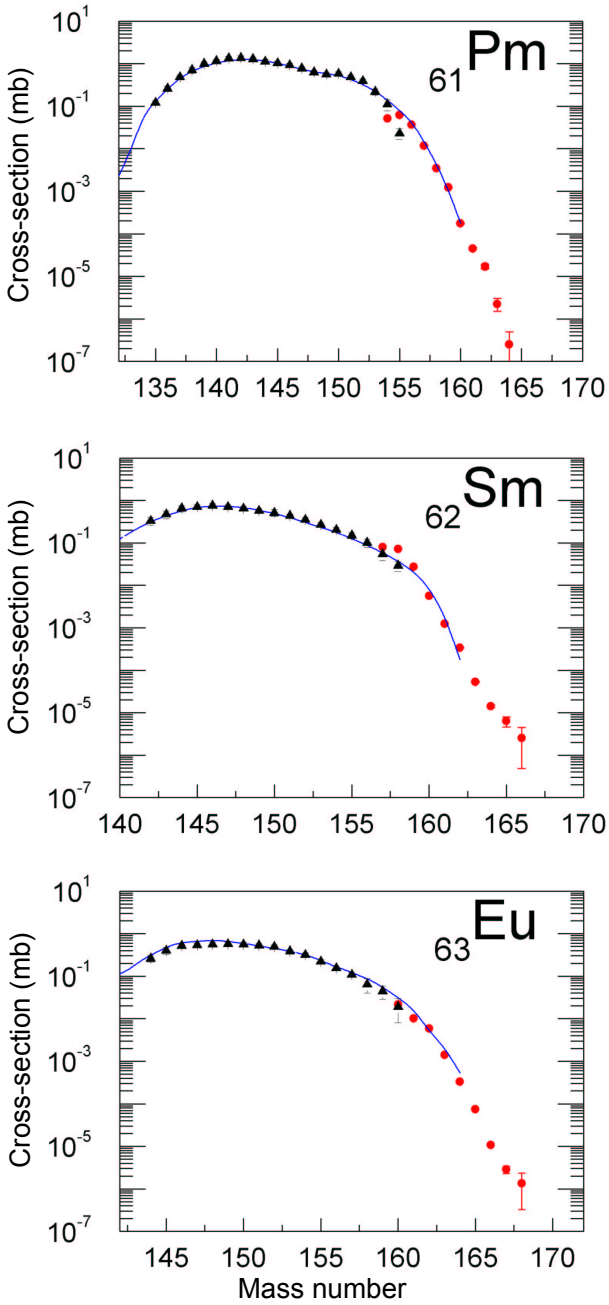

Figure 3.15: Measured production cross-sections of fragments produced in the reaction ^{238}U (1000 MeV/u) + Be (red circles), compared with the experimental results obtained by Bernas et al. [Ber03, Ber06] in the reaction ^{238}U (1000 MeV/u) + p (black triangles). The continuous line indicates the predictions of the ABRABLA model [Gai91].

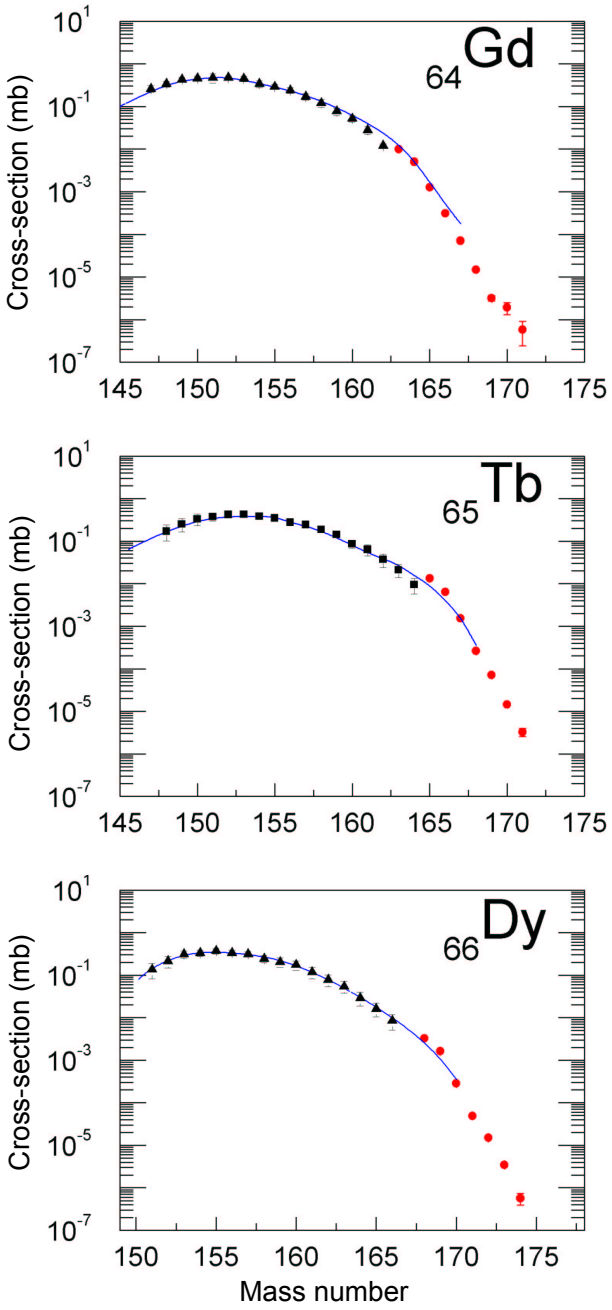

Figure 3.16: Measured production cross-sections of fragments produced in the reaction ^{238}U (1000 MeV/u) + Be (red circles), compared with the experimental results obtained by Bernas et al. [Ber03, Ber06] in the reaction ^{238}U (1000 MeV/u) + p (black triangles). The continuous line indicates the predictions of the ABRABLA model [Gai91].

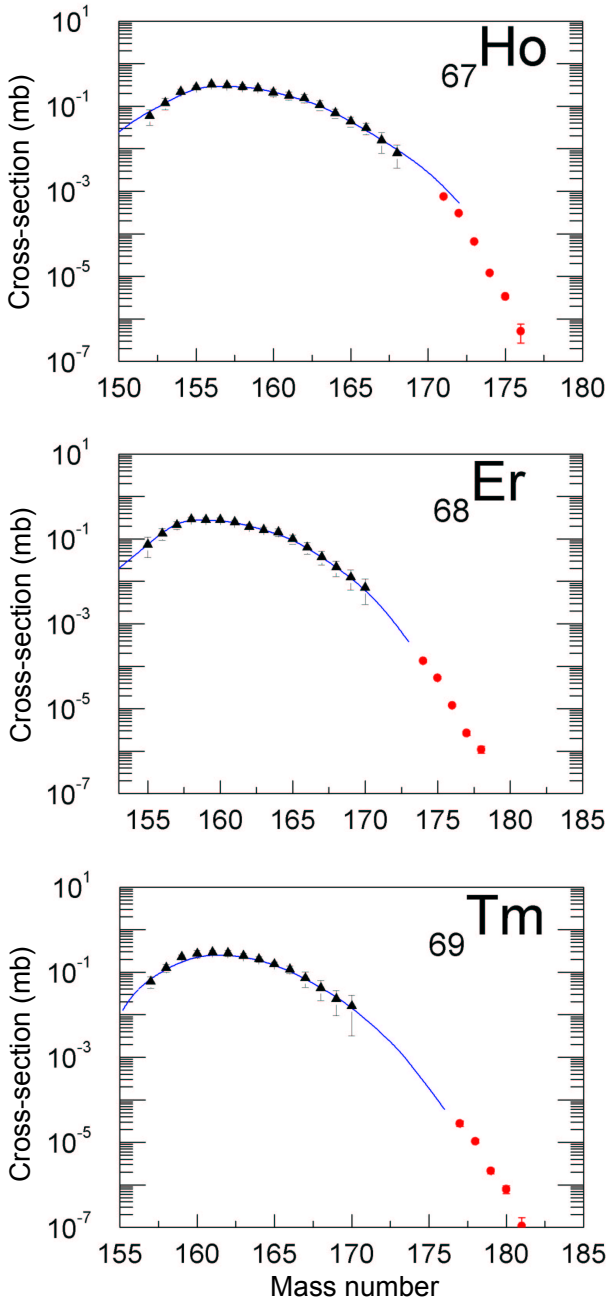

Figure 3.17: Measured production cross-sections of fragments produced in the reaction ^{238}U (1000 MeV/u) + Be (red circles), compared with the experimental results obtained by Bernas et al. [Ber03, Ber06] in the reaction ^{238}U (1000 MeV/u) + p (black triangles). The continuous line indicates the predictions of the ABRABLA model [Gai91].

Chapter 4

Investigation and Decay Measurements of Neutral and H-like ^{213}Fr Ions

Already in the pioneering experiments with the combination of the FRS and the ESR (see Fig. 4.1), Q-values and half-lives of bare and few electron projectile fragments have been measured for stored projectile fragments decaying via weak interaction [Irn96, Lit07, Win09]. The decay of stored mother and daughter nuclei can be measured in different experimental scenarios depending on the difference of their magnetic rigidities. If the half-lives of the selected α-emitters and their daughters are a few seconds or longer, the combination of stochastic [Nol04] and electron cooling [Ste04] can be applied. Both mother and daughter nuclei circulate in closed orbits in the ESR, where it is possible to perform a time-correlated Schottky analysis [Lit05]. In case the Bρ-difference of the mother and daughter nuclei exceed 2%, the daughter can be detected leaving the closed orbit at the next dispersive section [Gei92b].

It is our aim, with the present experiment, to start a campaign of measurements devoted to the investigation of α-decay properties of highly charged and bare nuclei [Erm57, Rub72, Zin06]. The decay of highly-charged ions is of importance in hot stellar plasmas and can now be investigated in the laboratory for the first time. Another open question in nuclear astrophysics is the influence of electron screening in nuclear reactions with light nuclei [Engs80]. As pointed out

by several authors [Ald71, Eng80, Str01, Bar02, Ass87, Pat08] screening can significantly affect the reaction rates at low energies. In fact, the α-decay constant λ, in the phase integral approximation (WKB), is proportional to the barrier penetration factor:

$$\lambda \propto Q \ \exp\left(\frac{2\sqrt{2m}}{\hbar}\int_{r_1}^{r_2}\sqrt{P(r)}\,dr\right), \tag{4.1}$$

where m is the reduced mass, Q is the sum of the kinetic energy of the α particle and the recoiling daughter nucleus, r is the distance between the α particle and the center of the daughter nucleus and r_1 and r_2 are the classical turning points for the equation $P(r) \equiv V(r) - Q = 0$. The difference of the barrier penetrability in the neutral ($P_N(r)$) and H-like (($P_H(r)$)) systems having atomic number Z can be written as:

$$P_N(r) - P_H(r) = -(\delta B(Z) - \delta B(1)) + (2V_e(Z,0) - 2V_e(1,0)) + (2\delta V_e(Z,r) - 2\delta V_e(1,r)). \tag{4.2}$$

The first two terms $\delta B(Z) \equiv B(Z,Z) - B(Z-2,Z-2) - B(2,2)$ are related to the electron binding energy and $B(Z,N_e)$ indicates the binding energy of N_e electrons in a field of the nucleus with Z protons. The second and third pairs of terms in equation 4.2 are the variation of the electron screening V_e at the site of the nucleus and at a distance r between the α particle and the center of the nucleus. To perform the calculation in equation 4.2 and obtain an estimation of the half-life from equation 4.1, several approximation are required. Precise calculations of the α-decay constant's shift for neutral and bare ^{213}Fr have been performed [Pat08] and the results provide a value of $\delta\lambda/\lambda = 2(\lambda_N - \lambda_B)/(\lambda_N + \lambda_B)$ on the order of few per mill.

With the combination of FRS and ESR we have for the first time the possibility to investigate this topic [Mus06]. In Figure 4.2, it is clearly demonstrated that by selecting an appropriate projectile energy and stripper medium, it is possible to inject bare and highly ionized α-emitters into the ESR.

The different phases of our experimental campaign are:

- lifetime measurements of neutral atoms at the FRS focal plane;
- Q_α-values and α-decay lifetimes measurement of bare and highly ionized α-emitters circulating in the ultra-high vacuum of the ESR.

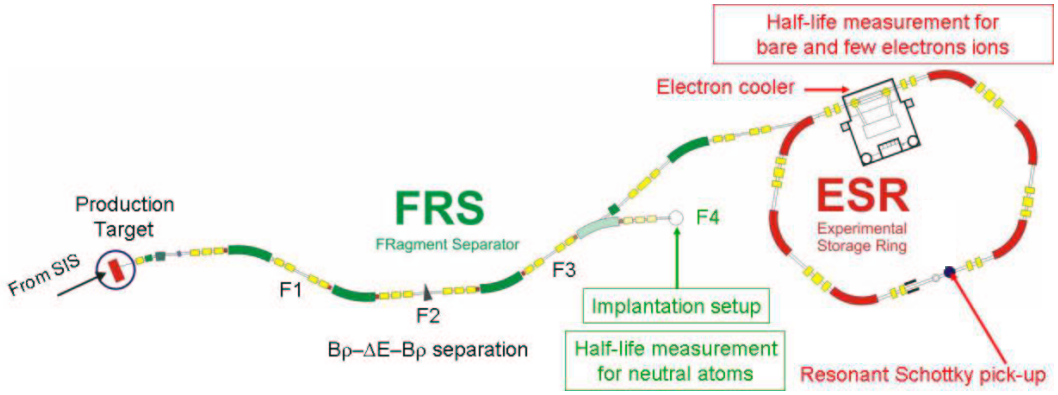

Figure 4.1: Setup for α decay studies of neutral and few-electron ions. The heavy projectile fragments are separated in-flight with the FRS. They reach the F4 area where they are implanted in a silicon detector for decay studies of neutral atoms. Alternatively, they are injected into the storage ring ESR for decay measurements of bare and H-like states.

^{213}Fr and ^{214}Ra nuclei have been selected as good candidates for such an investigation. These nuclei are known to be pure α-emitters and can be easily produced in uranium projectile fragmentation. Table 4.1 summarizes their known decay properties.

	$T_{1/2}$ (s)	α-branch (%)	Q_α (keV)
$^{213}Fr^{87+}$	34.82 (14)	99.44 (5)	6904.9 (18)
$^{214}Ra^{88+}$	2.46 (3)	99.941 (4)	7273 (4)

Table 4.1: Decay properties of the selected nuclei, ^{213}Fr [Bas07] and ^{214}Ra [Bro03].

4.1 Experiment for half-life determination of α-decaying neutral atoms

The main goal of the experiment was to determine the α-decay half-lives of two selected nuclei ^{213}Fr and ^{214}Ra. Their half-lives of several seconds are well suited for storage ring experiments applying electron cooling and Schottky spectrometry. For the implantation experiment at the FRS directly, the half-life restriction

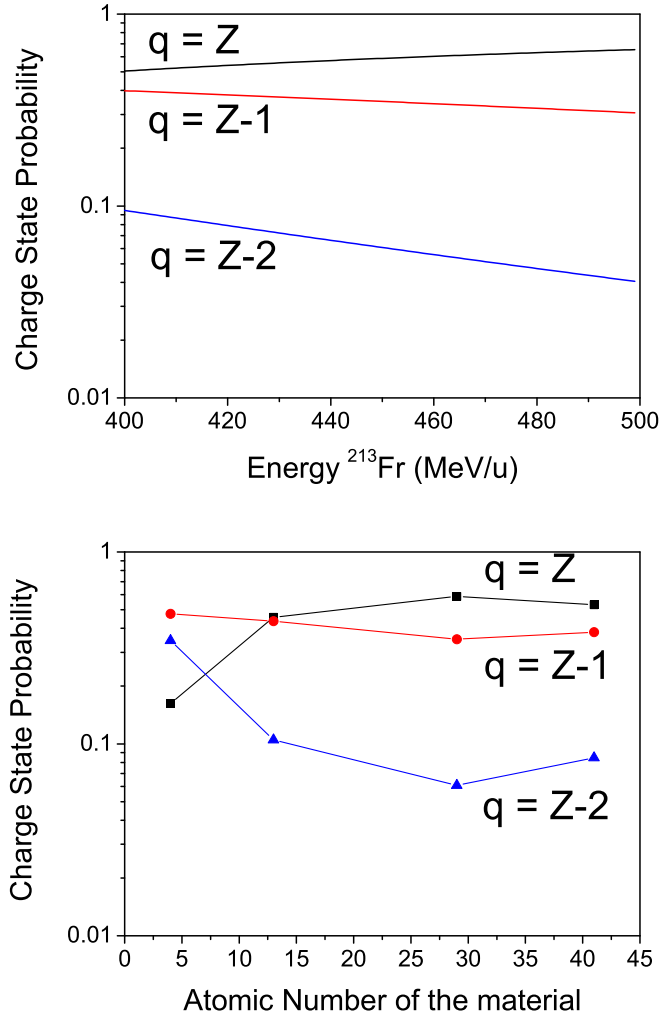

Figure 4.2: Upper panel: Calculated [Sch98] charge state evolution of the α-emitter ^{213}Fr in the energy range of (400 to 500) MeV/u at the exit of the copper stripper medium. Lower panel: Calculated [Sch98] charge state evolution of 500 MeV/u ^{213}Fr ions at the exit of different materials.

would be the flight time through the optical system, i.e., it should be longer than 200 ns.

4.1.1 Setup and measurements

An overview of the experimental setup is schematically shown in Figure 4.1, a zoom of the implantation area is shown in Figure 1.21. The experiment was performed at the FRS, by using a ^{238}U beam at 1 GeV/u impinging on a 2.5 g/cm^2 thick beryllium target with a Nb stripper backing. The beam intensity was reduced to about $5 \cdot 10^7$ ions/s. The nuclei of interest were ^{213}Fr and ^{214}Ra.

The selected fragments transmitted through the FRS reached the final focal plane at energies in the range of 500 to 600 MeV/u. In order to measure their decay half-lives, the selected nuclei were implanted into the active stopper, see Section 1.5.2. It serves as an implantation catcher and as a detector of the α activity. A degrader in the middle focal plane of the FRS was used for the separation of the reaction products in-flight. In order to implant the nuclei into the active stopper, another homogeneous variable aluminium degrader has been used to slow down the fragments in front of the active stopper. Two plastic scintillation detectors were placed both in front and behind the catcher to verify the correct implantation.

4.1.2 Data analysis and results

The analysis procedure consisted of several steps:

- in-flight identification including verification with μs-isomers;
- implantation in the active stopper (see Section 1.5);
- decay measurements during the beam-off period;
- measurement of the half-life of the selected fragments.

The identification of the fragments reaching the final focal plane was performed using the time-of-flight and energy deposition technique described in Chapter 1. The identification pattern was verified by measuring in coincidence γ-rays from known μs-isomers. For this verification a dedicated field setting of the

FRS was used for the reference fragment ^{212}Rn. In Figure 4.3 the identification plot together with the measured γ spectrum and the half-life of ^{212}Rn isomer are shown. The three γ peaks correspond to the γ cascade transitions ($6+ \rightarrow 4+$), ($4+ \rightarrow 2+$) and ($2+ \rightarrow 0+$) with an half-life of 0.91 ± 0.03 μs [Bro05]. In the same FRS setting, several other known isomers ^{211}Rn, ^{209}At and ^{210}At were included to redundantly verify the identification matrix. The additional identification procedure is illustrated in Figure 4.4 taking into account the secondary reactions in the F4 matter. The correlation of the two MUSICs signals allowed us to select the bare Fr ions. Then, the position measurement at F4 combined with the A/q information provides the isotopic separation see Figure 4.4 central part. The degrader in front of the active stopper caused about 40% secondary reactions which have been removed from the analysis by Z selection using the energy deposition in the scintillator SCI2.

In order to correlate in position and time the implantation and decay events, the multiplicity of the implantation events during the spill was kept around 1 per pixel. This condition was achieved with a reduced implantation rate of about 100 Hz. The multiplicity is defined as the number of individual strips participating in one implantation or decay event in the silicon detector. Figure 4.5 shows the implantation (left panel) and decay (right panel) multiplicity per pixel averaged over the total number of spills. The beam extracted from SIS-18 had a spill structure, with a spill length varying from 1 to 4 s and a cycle up to 180 s (Fig. 4.6). The half-life measurement was performed with the correlated implantation and decay events in the silicon detector. The signals from the silicon detectors gave information about the location where the identified α-emitters were implanted. The decay events represent the kinetic energy of the emitted α particle. The atomic range of the emitted α particles in the silicon material is about 0.05 mm, therefore this event comes from the same strip as the implanted mother ion. The absolute time of each event was measured via precise time stamping with a resolution of 25 ns.

After the identification for each selected fragment the spill number and the coordinates (strip x and strip y in the silicon detector) of the implanted ions were recorded. The full identification with all the conditions discussed above, was applied to record the α-decay spectrum in coincidence. The results of this correlation

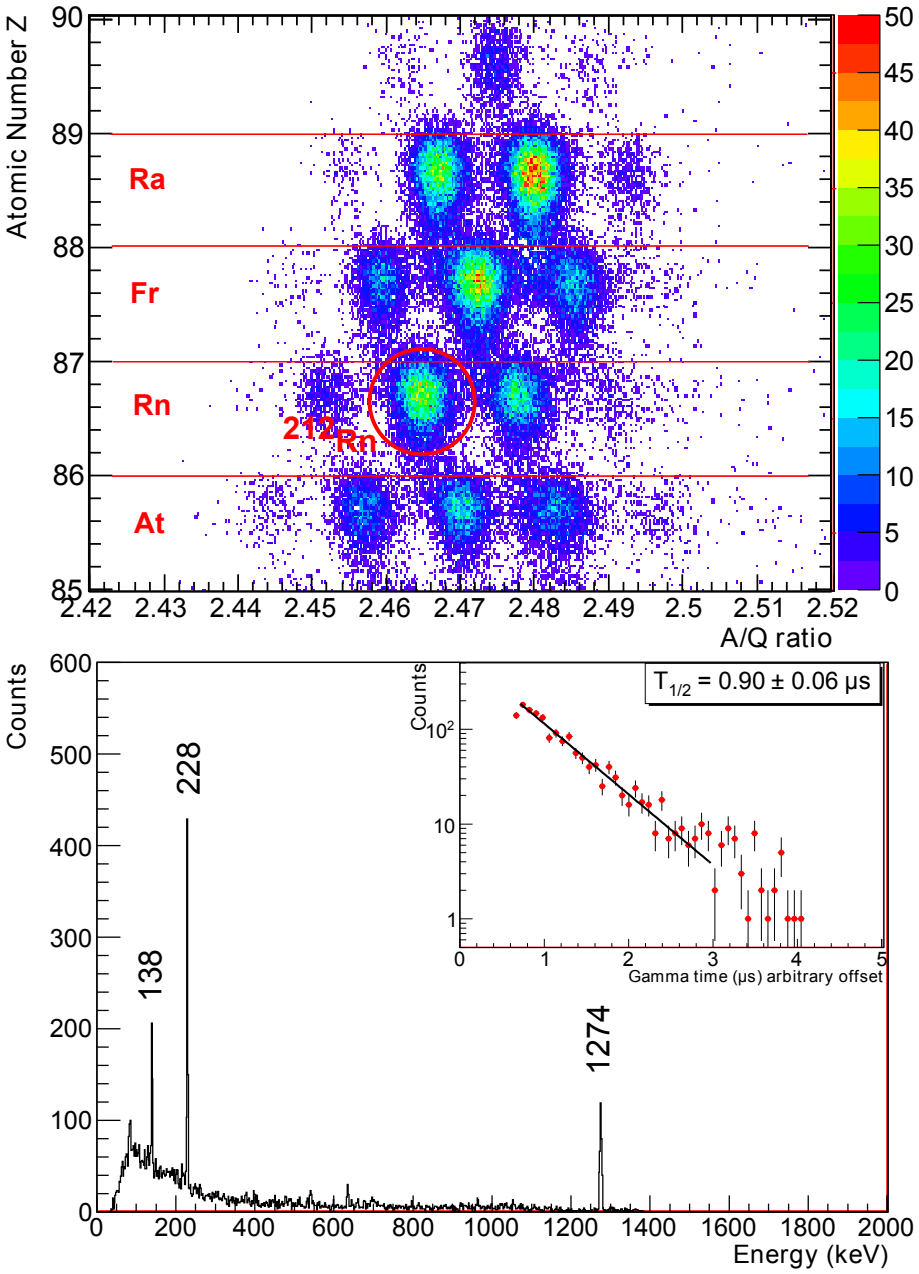

Figure 4.3: Experimental verification of the identification matrix via the coincidence measurement of the known μs-isomer ^{212}Rn. TOP: Measured particle identification for the FRS setting for fully stripped ^{212}Rn. BOTTOM: Measured γ-ray energy spectrum gated on the selection of the ^{212}Rn fragment. The inset shows the half-life of the isomeric decay. The measured γ energies and half-life are in good agreement with the literature values [Bro05].

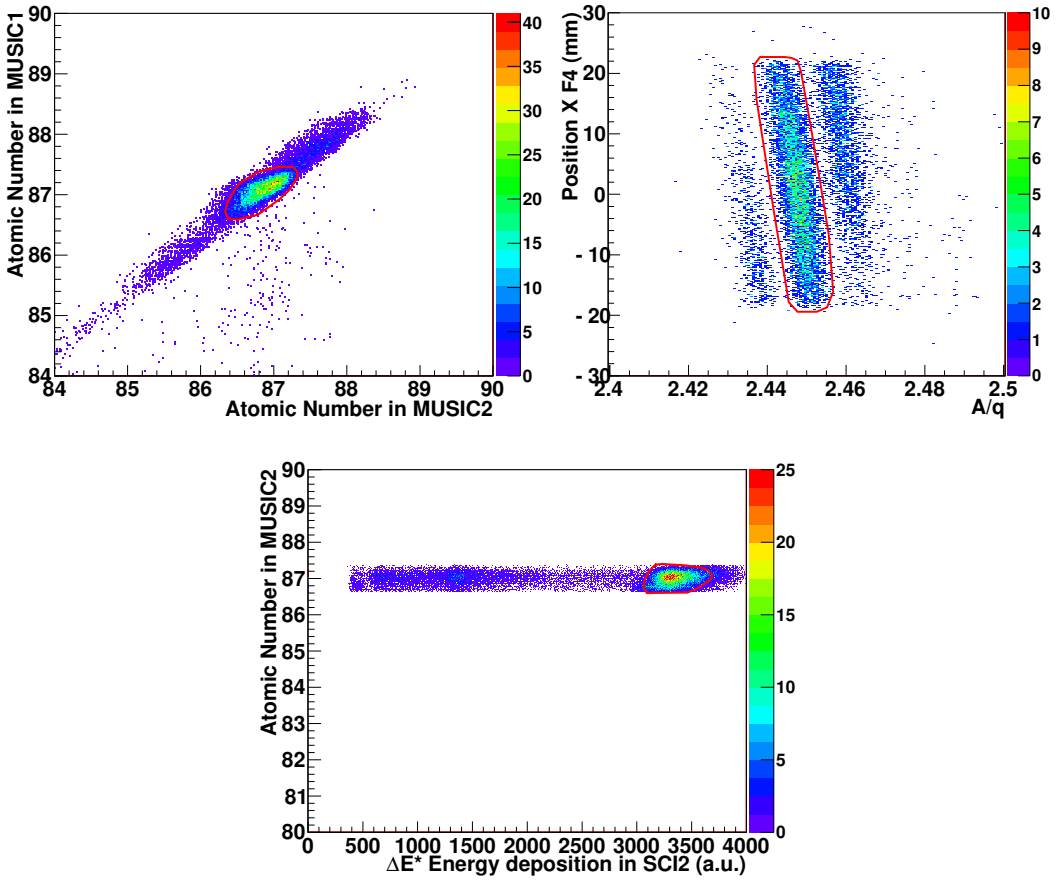

Figure 4.4: Rejection of secondary reactions in the matter at F4. Left panel: The Z information extracted from the two ionization chambers placed at F4. The condition shown in red selects the bare Fr isotopes which did not undergo nuclear charge-changing reaction. Right panel: Horizontal position of the Fr isotopes at F4. ^{213}Fr is selected by choosing the corresponding A/q. Lower panel: The secondary reactions in the degrader in front of the active stopper have been removed from the analysis via selecting the energy deposition signal of the SCI2 directly behind the degrader.

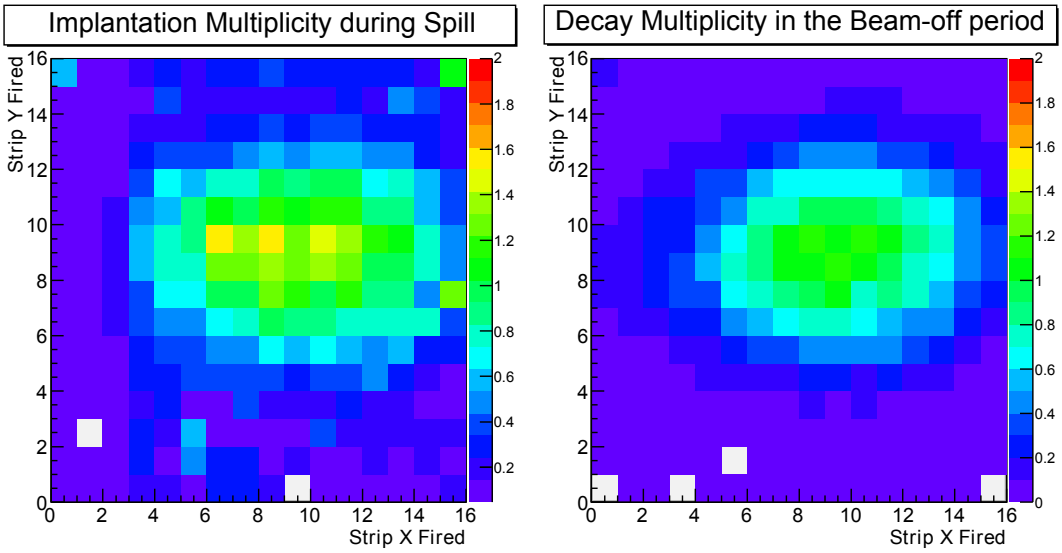

Figure 4.5: Measured implantation (left panel) and decay (right panel) multiplicities averaged over the total number of spills for ^{213}Fr with beam-off period of 180 s and an implantation rate of about 100 Hz. Note that the goal of multiplicity 1 has been achieved.

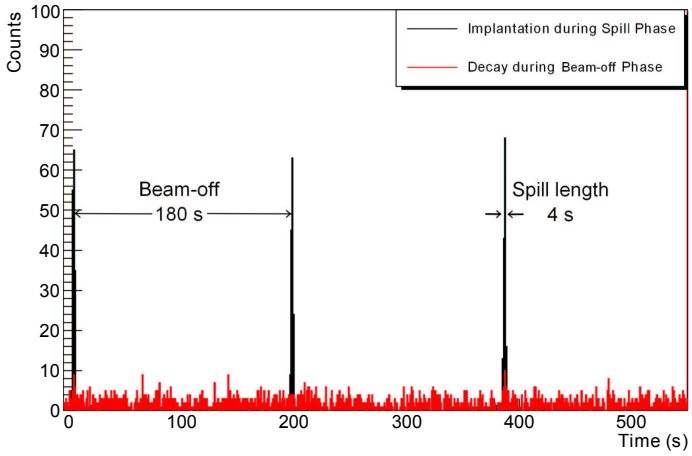

Figure 4.6: Selected spill structure of the implantation experiment at F4. The implantation events during the spill (black line) and the decay events during the beam-off period (red line) are indicated for ^{213}Fr^{87+}.

method is a clean energy spectrum measured with the silicon detector, see Figure 4.7 upper and lower panel for ^{213}Fr and ^{214}Ra, respectively. For comparison the corresponding α-decay spectra without any conditions are also shown in the same pictures. Despite of the applied identification conditions, there is an inevitable back-ground due to random coincidences with the radioactivity accumulated from previously implanted ion species in the detector. Therefore, an energy selection window was applied to the characteristic α-line of ^{214}Ra and ^{213}Fr. The energy window has a width of $\pm 3\sigma$ of the peak. Table 1.2 summarizes the measured α decay energies of all implanted α-emitters without identification conditions on the mother fragments. The table lists also the daughters produced in the α decays. The kinetic energies are in excellent agreement with the well-known literature values, see comparison in Figure 1.29. Thus this measurement provides another complete and independent identification pattern of the implanted α-emitters. The latter method has been successfully applied for the identification of super-heavy elements at GSI and several other laboratories [Hof00].

Half-life determination

For all the decays which fulfilled the identification and position correlation conditions, the time differences between each α-decay event and the end of the previous spill phase have been determined. These events were accumulated in a histogram to obtain a decay curve. The radioactive decay is described by:

$$\frac{dn}{dt} = -n\ \lambda\ e^{-\lambda t} \tag{4.3}$$

where dn is the number of decays between the time t and $t+dt$, n is the total number of counts and $\lambda = \ln 2/T_{1/2}$ is the decay constant. The decay curve was then fitted using an exponential function implemented in the MINUIT package within the ROOT software environment [ROOT]. The fitted range of the decay curve was truncated to the largest common beam-off period. The fit parameters provide the half-life and the corresponding uncertainties. The reduced $\chi_r^2 = \chi^2/NDF$ of the fit results are shown in Table 4.2. Example of the decay curves with the fitted curves for ^{213}Fr (180 seconds beam-off) and ^{214}Ra are shown in Figure 4.8 from top to bottom respectively.

The measured weighted mean value of the half-life for ^{213}Fr in this experiment

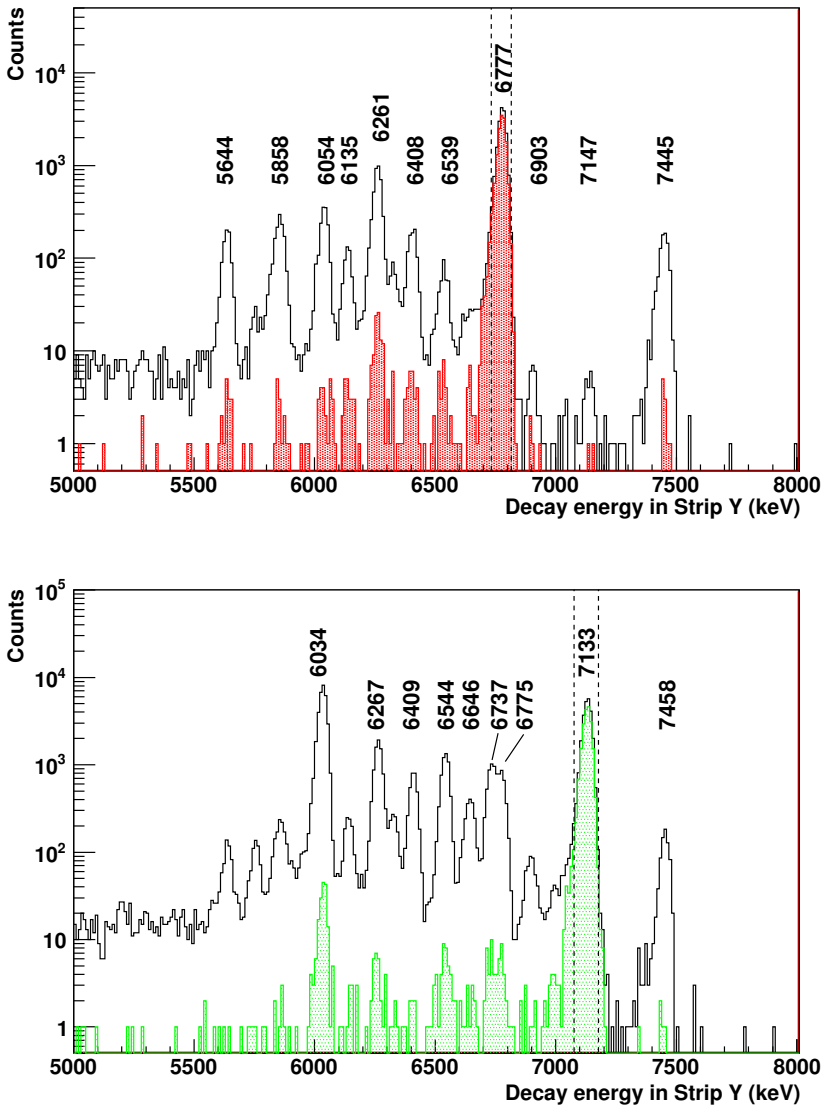

Figure 4.7: α-energy spectra measured during the FRS field setting for the separation of ^{213}Fr (upper panel) and ^{214}Ra (lower panel). The black peaks represent the α-decays recorded without any additional identification condition. The red shaded spectrum (^{213}Fr) and the green one (^{214}Ra) were obtained under the condition of particle identification in-flight for ^{213}Fr and ^{214}Ra, respectively, in coincidence with the implantation position in the silicon detector and excluding secondary reactions in the material at F4. The half-life measurements of ^{213}Fr and ^{214}Ra have been performed using the events inside the indicated energy window of the characteristic α-line.

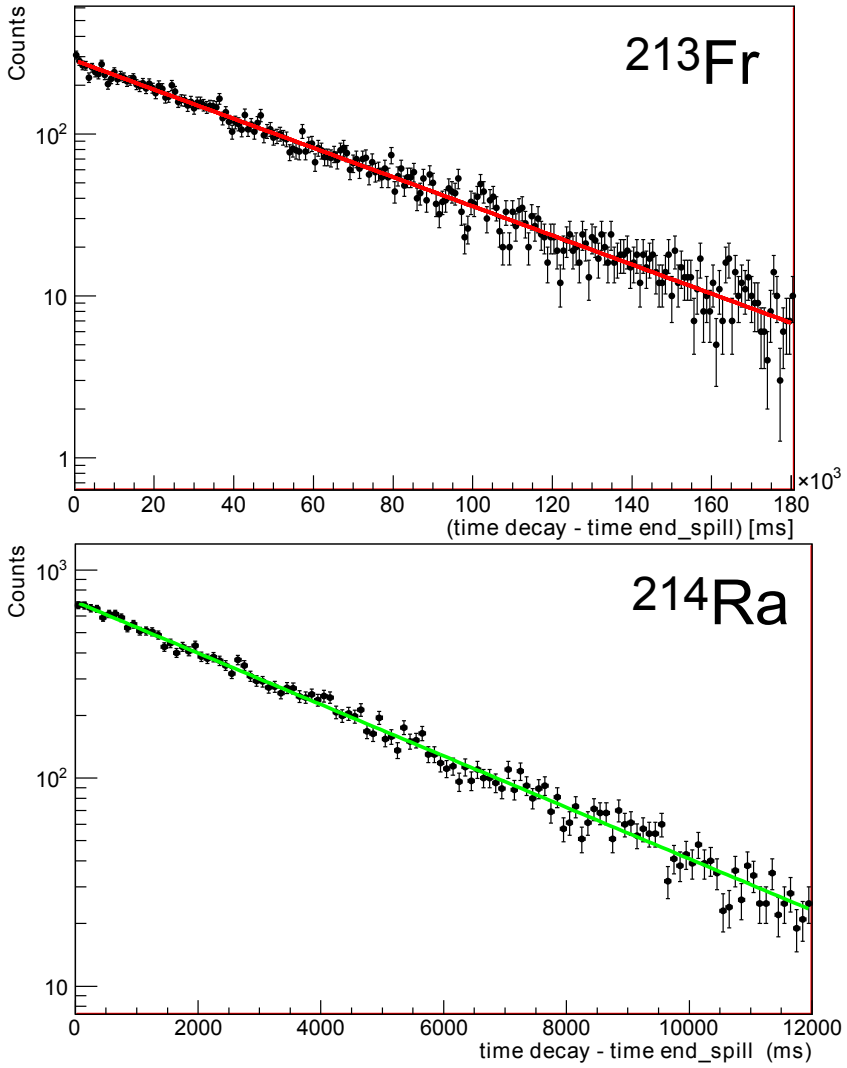

Figure 4.8: Decay curves of the neutral ^{213}Fr (upper panel) and neutral ^{214}Ra atoms (lower panel). The decay curves were obtained from the α-decays correlated with the implanted fully identified fragments (correlation method). The data points are shown with a bin size of 0.5 s and 0.1 s for ^{213}Fr and ^{214}Ra, respectively. The lines represent the results of the exponential fit functions.

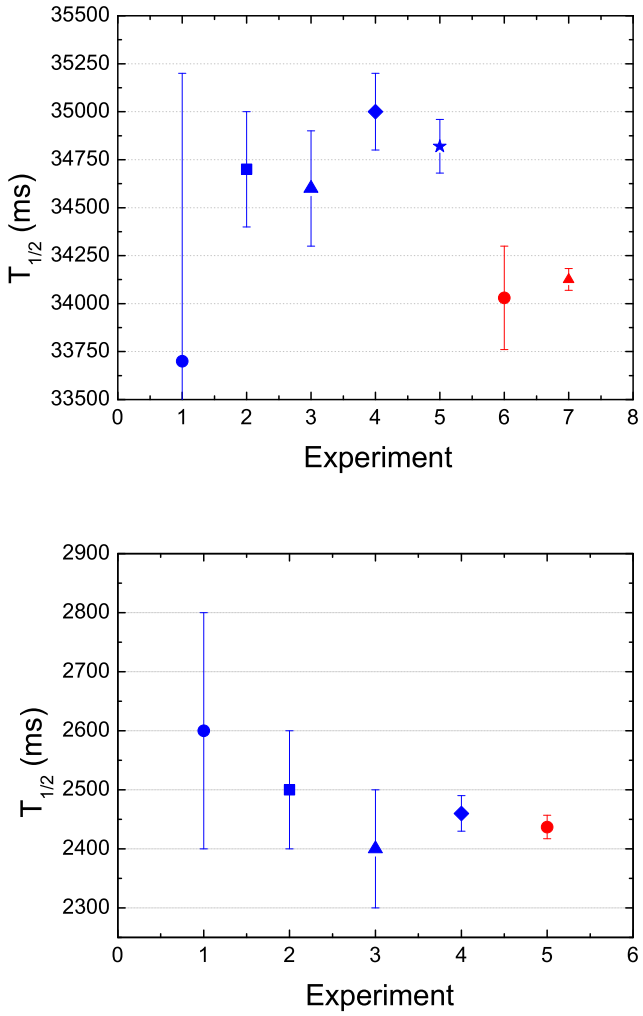

Figure 4.9: Comparison of measured half-life of ^{213}Fr (upper panel) and ^{214}Ra (lower panel) neutral atoms with the literature values. Upper panel: experiments from 1 to 4 corresponding to the references [Gr64, Va67, Ho74, Bo82], respectively. Experiment number 5 is their weighted average according to reference [Bas07]. The value number 6 represents the results from the FRS experiment and number 7 represents the results from our experiment performed in Catania with fusion evaporation residues. Lower panel: experiments from 1 to 4 corresponding to the references [Val67, Lob68, Hor74, Bem73], respectively. The value number 5 represents the results from the FRS experiment.

^{213}Fr			
Beam-off period (s)	Decays counts	$T_{1/2} \pm \sigma_T$ (s)	χ^2_r
180	16188	34.0 ± 0.3	1.18
60	20697	34.2 ± 0.7	0.94
weighted mean value		34.03 ± 0.27	
^{214}Ra			
Beam-off period (s)	Decays counts	$T_{1/2} \pm \sigma_T$ (s)	χ^2_r
12	23064	2.441 ± 0.021	1.11

Table 4.2: Results of the half-life measurements of neutral ^{213}Fr and ^{214}Ra atoms. The values of the half-life and the corresponding uncertainties have been obtained from the fit parameters. The number of degree of freedom and the values of the reduced χ^2_r are also listed.

was determined to be 34.03 ± 0.27 s. Comparing this result with the values from the literature [Gr64, Va67, Ho74, Bo82, Bas07] it appears to be lower than the corresponding values from the previous experiments. This comparison is shown in the upper panel of Figure 4.9. However, our half-life measurement for ^{214}Ra ($T_{1/2} = 2.441 \pm 0.021$ s) is in excellent agreement with the literature values [Bas] especially with the experiment with the highest accuracy. To investigate the issue of the half-life of ^{213}Fr, we performed another experiment with fusion evaporation residues at Laboratori Nazionali del Sud in Catania. The result of the Catania experiment is $T_{1/2} = 34.126 \pm 0.056$ s, which is in excellent agreement with the GSI experiment. The value of the Catania experiment is also depicted in Figure 4.9 upper panel [Mus11].

4.2 Experiment for half-life determination of α-decaying H-like ions

4.2.1 Setup and measurements

^{213}Fr ions have been produced via projectile fragmentation of 455 MeV/u $^{238}U^{73+}$ ions with an intensity of $\sim 10^9$ ions/spill. Using the fast extraction mode of the

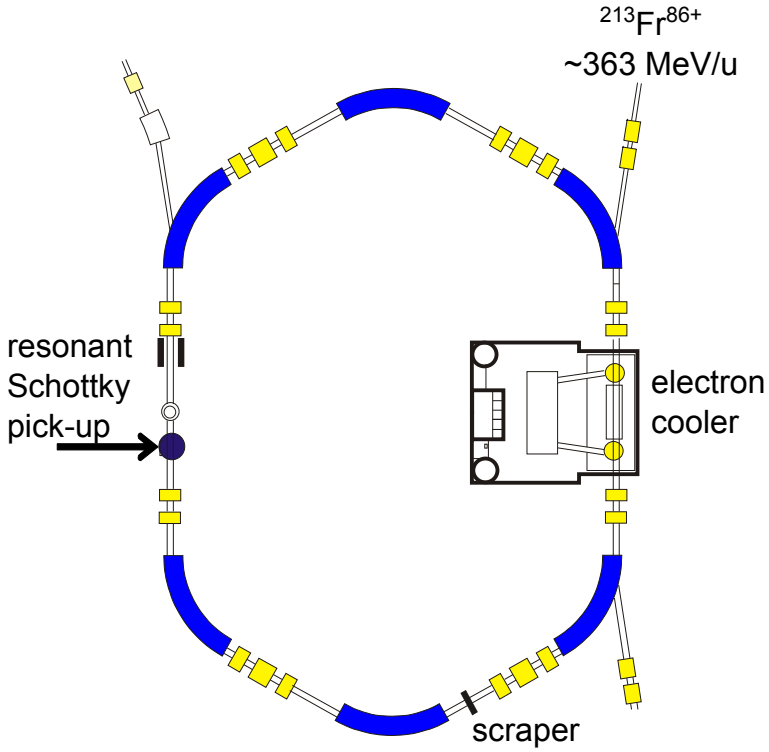

Figure 4.10: Layout of the ion storage-cooler ring ESR [Fra87]. The circumference of the ring is about 108.4 m. The beam circulates clockwise in the ring. The positions of the electron cooler, the resonant Schottky pick-up and the scraper are indicated.

SIS, the projectiles impinged on the production target (1.03 g/cm^2 thick beryllium) placed at the entrance of the FRS (Fig. 4.1). The H-like ^{213}Fr ions were separated in-flight by means of the Bρ-ΔE-Bρ method at the FRS and subsequently injected into the Experimental Storage Ring (ESR) [Fra87]. The different isotopes injected and circulating in the ring were identified by means of their revolution frequency. A pure ^{213}Fr ion beam was cooled and stored to perform precise half-life measurements. Possible contaminants were removed from the closed orbit with suitable mechanical slits (scrapers) before the decay measurement started. The decay of H-like ^{213}Fr ions was measured by applying time-resolved Schottky Mass Spectrometry (SMS) [Fra08, Lit10].

The revolution frequency is directly proportional to the mass-over-charge ratio, particular if the velocity spread (Δv/v) is negligible. The relation between

the revolution frequency (f) and the mass-over-charge (m/q) ratio is given by:

$$\frac{\Delta f}{f} = -\alpha_p \frac{\Delta(m/q)}{(m/q)} + \frac{\Delta v}{v} \gamma^2 \left(\frac{1}{\gamma^2} - \alpha_p \right), \tag{4.4}$$

where α_p is the momentum compaction factor and γ is the relativistic Lorentz factor.

The projectile fragments have an inevitable velocity spread of a few percent due to their creation process. Therefore, we applied electron cooling which reduced the velocity spread to $\Delta v/v \approx 5 \cdot 10^{-7}$ for stored beams with low intensity [Ste96]. The cooling time in the ESR normally takes a few seconds which is the reason of the selected ^{213}Fr α-emitter with a half-life of about 34 s.

There are mainly two methods to measure half-lives of stored ions in the ESR with the Schottky pickup. The first one involves the change of the Schottky area under the frequency peak for many particles (many-particle method). The second one deals with very few stored particles and the decay is manifested by discrete jumps in the frequency intensity (single-particle method). This latter method has the advantage to be independent from the assumption of a strict proportionality of the Schottky area and the number of stored ions.

A new resonant Schottky pickup was used to measure the revolution frequency spectra [Nol11, San11]. The resonator has a factor 100 higher sensitivity than the parallel plate broad band old Schottky pickup. At our energies the stored ions circulate in the ESR typically with revolution frequencies of about 2 MHz. Figure 4.11 shows a block diagram of the resonant Schottky pickup [Nol11]. The RLC circuit is an equivalent of the pick-up cavity with the coupling loop. The low noise amplifier (LNA) is mounted directly on the flange of the coupling loop. The LNA is a wide-band amplifier. Therefore the following band-pass filter is necessary to prevent intermodulation in the following amplifiers due to the wide-band noise from the LNA. The amplifiers A2 and A3 amplify the signal to a level which is sufficient to transport it through a long coaxial line to the Fast Fourier Transform (FFT) spectrum analyzer in the main control room.

The resonator signal is mixed with the direct signal from a local oscillator to shift the signal to the operating domain of the spectrum analyzer. To obtain a more accurate Fourier analysis, the multitaper analysis has been applied instead of the Hanning windowing [Per93].

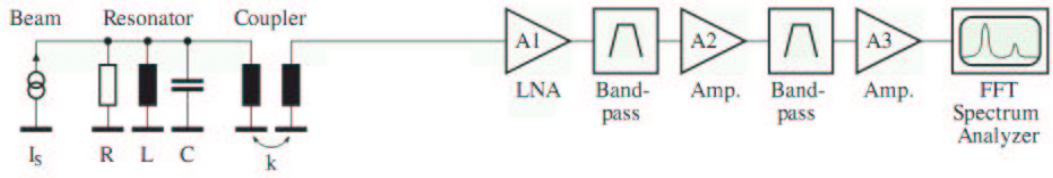

Figure 4.11: The signals of the resonator are processed and which noise sources appear [Nol11]. On resonance, the noise spectrum is dominated by the unavoidable thermal 300 K noise from the resonator. The preamplifier (A1) are special low-noise devices. The bandpass filters in the processing chain are needed to prevent overloading the broad band amplifiers A2 and A3.

4.2.2 Data analysis and results

The analysis has been performed with the Schottky signals recorded with a real-time spectrum analyzer (Tektronix RSA3303B). In order to improve the signal-to-noise ratio, the Schottky frequency spectra have been created by averaging FFT spectra over several blocks. The value of the number of averages $N_{av} = 25$ has been chosen considering the expected half-life of the ^{213}Fr ions. The corresponding integrated time bin was 0.8 s. The relative error $\sigma_{I_{Schottky}}$ associated to the area determination of the Schottky noise power density spectrum $I_{Schottky}$, is given by [Schl97]:

$$\frac{\sigma_{I_{Schottky}}}{I_{Schottky}} = \frac{1}{\sqrt{N_{av}}}. \tag{4.5}$$

Several files were recorded with circulating H-like ^{213}Fr ions for 300 seconds after the injection. A presentation of the obtained frequency spectra versus the time after injection is illustrated in Figure 4.12 (top) and the corresponding Schottky frequency spectra at different times after injection are displayed at the bottom panel. For each recorded file, the frequency interval corresponding to the trace of ^{213}Fr ions was selected and the noise power density projected to the time axis. All the measured projections were accumulated to create a decay histogram. For each file, the error bars associated to the noise power density were calculated according to equation 4.5. The accumulated histogram plotted in Figure 4.13 was fitted with the function:

$$N_{Fr}(t) = N_{Fr}(t_0)e^{-\lambda t}, \tag{4.6}$$

where $N_{Fr}(t)$ and $N_{Fr}(t_0)$ are the number of parent ions at the time t after the

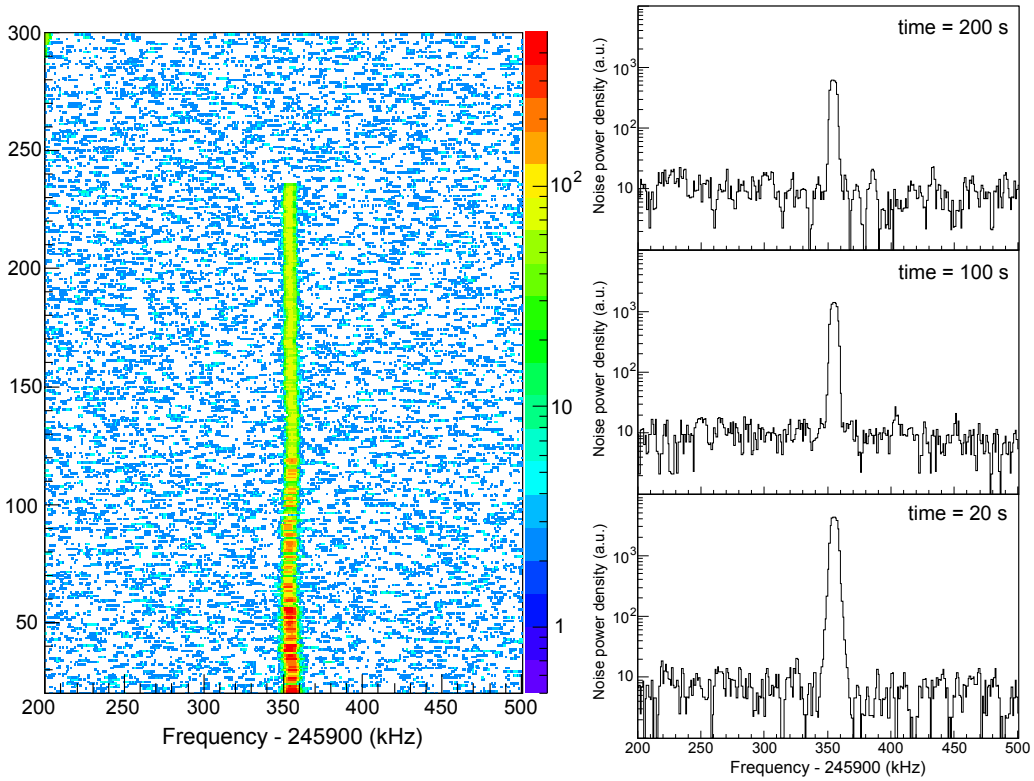

Figure 4.12: Left panel: Schottky frequency spectra as a function of the time after injection into the ESR. The time increases from bottom to top. The area under the frequency line is assumed to be proportional to the number of stored ions (many particles method). Right panel: The corresponding Schottky frequency spectra at 20, 100, 200 s after injection.

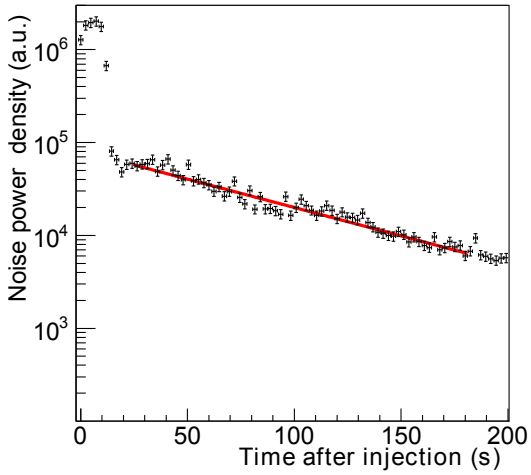

Figure 4.13: Decay spectrum deduced from the Schottky area of H-like ^{213}Fr ions (many-particle method). The data points correspond to the integrated frequency peak of $^{213}Fr^{86+}$ and are shown in the laboratory frame with a resolution of 2.4 s. The error bars associated to the noise power density were calculated according to equation 4.5. The line represent the fit according to the exponential decay function.

injection and t_0 the time of injection and λ is the decay constant in the laboratory frame. The fitting range has been chosen to exclude the cooling phase at $t \leq 20$ s and to exclude $t > 180$ s where only few H-like ^{213}Fr ions were left. The fit parameters, calculated with the MINUIT package within the ROOT software [ROOT], provided the half-life and the corresponding uncertainty. The half-life value obtained corresponds to the laboratory frame. With the known velocity from the electron cooler the Lorentz factor $\gamma = 1.39$ transforms the fitted results to the rest frame:

$$T_{1/2}^{Lab} \equiv \gamma \, T_{1/2}, \tag{4.7}$$

where $T_{1/2}$ represents the half-life in the rest frame of the decaying particle. The half-life in the rest frame deduced with the many-particle method amounts to $T_{1/2}(^{213}Fr^{86+}) = 34.4 \pm 1.6$ s. The value of the reduced χ_r^2 proved the good quality of the fit. The half-life in the rest frame and the χ_r^2 values are shown in Table 4.3.

Applying the single-particle decay method [Bos06, Fra08] only a few ions were injected into the ESR, because the Schottky mass spectrometry is sensitive down

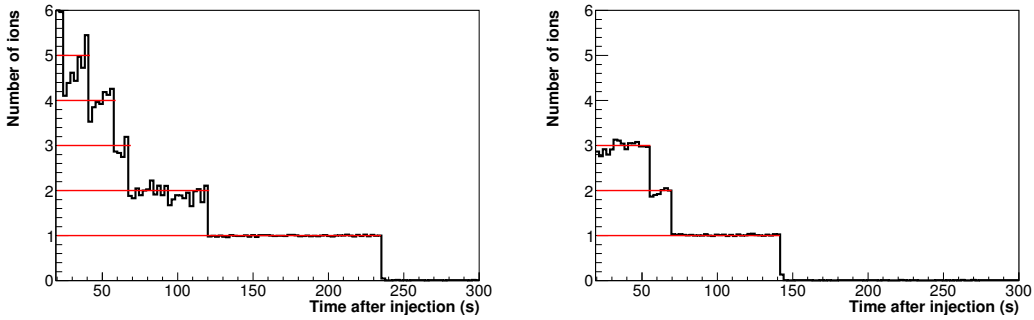

Figure 4.14: Examples of single-particle decay spectra for H-like ^{213}Fr ions. The number of stored ions (5 in the left panel spectrum and 3 in the right one) has been calculated from the noise power density.

to single stored ions. The steps of the decay could be identified only for 3-5 stored and cooled ions, see Figure 4.14. In the Schottky spectra, the disappearance of the mother nuclei have detected and the decay time measured. The time resolution for the decay time assignment was about 100 ms.

In total 36 single-particle decays have been unambiguously identified and measured. The deduced time was inserted in a spectrum with a logarithmic time-scale. In this presentation the exponential decay is converted to a distribution with a universal shape independent of the half-life [Sch84]. The frequency distribution of the decay time can be, thus, written as a function of the logarithm of time $\theta = \log_e(t)$ as:

$$\frac{dn}{d\theta} = n\lambda e^{\theta} e^{-\lambda e^{\theta}}. \tag{4.8}$$

Two free parameters, the number n of counts and the half-life $T_{1/2} = log(2)/\lambda$, determine the height and the position of the peak, respectively. The most probable value of this distribution is the logarithm of the life time ($\tau = 1/\lambda$). Figure 4.15 shows the spectrum of the time intervals between the decay and the injection into the ESR. The solid line represents the fit to data with the function given in equation (4.8). The fitting range was chosen between 20 and 300 seconds in order to exclude the cooling time. The dashed line is the extension of the fit function outside the considered range. The deduced half-life in the rest frame amounts to $T_{1/2}(^{213}Fr^{86+}) = 34 \pm 6$ s. The relatively big χ^2_r of 3.5 indicates the low statistics of this pilot experiment.

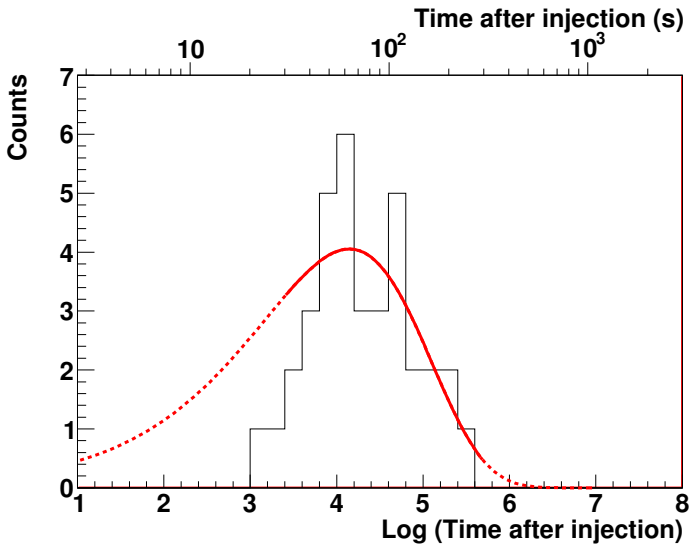

Figure 4.15: Spectrum of the time interval between the decays and the injection into the ESR. The horizontal axis represents the logarithm of the time after injection. For orientation the upper part of the horizontal axis shows the time after the injection in seconds. The solid line represents the best fit of the data with the function presented in equation (4.8). The fitting range was set from 20 to 300 seconds due to the cooling time. The dashed line is the extension of the fitting function outside the considered range.

Table 4.3 summarizes the measured α-decay rates in the rest frame of the ions for neutral and H-like ^{213}Fr ions.

neutral ^{213}Fr			
	Decay events	$T_{1/2} \pm \sigma_T$ (s)	χ_r^2
FRS	36885	34.03 ± 0.27	/
LNS	∼ 620000	34.160 ± 0.058	0.98

H-like ^{213}Fr			
	Decay events	$T_{1/2} \pm \sigma_T$ (s)	χ_r^2
ESR many-particle method	∼ 500	34.4 ± 1.6	1.7
ESR single-particle method	36	34 ± 6	3.5

Table 4.3: Comparison of the results for the half-life measurements of neutral and H-like ^{213}Fr ions. The half-life ($T_{1/2}$) of neutral ^{213}Fr has been measured at the Fragment Separator at GSI and at the Laboratori Nazionali del Sud in Catania. The measurements of H-like stored ^{213}Fr ions have been performed at the FRS-ESR facility at GSI. The values of the reduced χ_r^2 are also shown for comparison.

The results from our experiments with neutral and H-like ^{213}Fr clearly demonstrate that both half-lives are in agreement within the error bars. This result contradicts to the previous theoretical work of [Erm57] which predicts a difference of the half-lives of about 40%. We achieved an accuracy for neutral ^{213}Fr atoms of 0.8% and 0.2 % in our experiments at GSI and Catania, respectively. The errors are larger, (more than 4%), for our pilot experiment with the FRS-ESR. According to a more realistic model [Pat08, Zin06, Typ11] we expect for neutral and H-like ^{213}Fr a difference in the sub-percent region. For a more conclusive experimental contribution in this expected much smaller difference we plan future experiments with the FRS-ESR facility with much higher statistics.

Summary

The research of exotic, short-lived nuclei is a main contribution of modern nuclear physics to improve the knowledge of the strong interaction and to understand the synthesis of elements in stellar media. Nature is still ahead of the laboratories since in the astrophysical r-process very neutron-rich nuclides are continuously created which we just barely reach or which still have to be discovered.

For this challenge new powerful accelerators and experimental tools have been developed to expand the frontiers of discovered nuclides. Besides a high intensity primary beam efficient and very sensitive in-flight separators are needed to access new nuclides in this field. To exploit the full discovery potential also the applied particle detectors and especially the unambiguous identification have to be steadily improved and extended in the experiments.

In the presented work Uranium projectile fragmentation and fission have been used to discover new neutron-rich nuclides in the Z-range above 60 at the FRS. In this region of heavy nuclides most radioactive beam facilities have clearly strong limitations.

A 1000 MeV/u ^{238}U beam impinged on the 1.6 g/cm^2 thick beryllium production target at the entrance of the FRS with an intensity of 2×10^9 ions/spill. The reaction products were separated by the FRS in an achromatic ion-optical mode. The spatial isotopic separation in flight was obtained with two stages of magnetic selection (Bρ) and atomic energy loss in two degraders located at the first and second focal plane of the FRS. With detectors a full identification of reaction products in-flight was obtained with respect to their nuclear charge Z and mass A.

The particle identification is even at these high energies a challenge because a small fraction of the separated ions is still carrying several bound atomic elec-

trons emerging from the layers of matter placed at the different focal planes, i.e., the magnetic rigidity and the energy deposition measurements could lead to ambiguous isotope identification. This experimental problem has been solved with a new implantation setup viewed by efficient gamma-detectors. This so-called ITAG setup, developed and applied in the framework of this doctoral research, has the task to identify implanted fragments by measuring the gamma-radiation emitted by well-known μs isomers. This isomer tagging technique was applied in order to verify the identification of the reaction products.

The major result of this experimental efforts were the discovery of 63 new isotopes in the relative short FRS experiment. This progress represents a wide potential for nuclear structure and astrophysics. In addition, this experiment has also confirmed the new isotopes reported in the literature recently. The results of the present experiment have been possible due to the improved separation and particle identification at the FRS where the isomer tagging technique has a significant contribution. Unambiguous fragment identification is a key for these investigations at the frontiers.

The first measured property of the discovered isotopes was the determination of the production cross sections. They are highly relevant to plan further studies with the discovered nuclei and contribute to the basic understanding of projectile fragmentation reactions. A comparison with theoretical model calculations show good agreement. However, for the most neutron-rich nuclei no predictions were available yet.

Another part of this doctoral work was to start a campaign of measurements devoted to the investigation of α-decay properties of highly-charged and bare ions compared to the conventional experiments with neutral atoms. The decay of highly-charged ions is of importance in hot stellar plasmas and can now be investigated in the laboratory for the first time.

In the first part of the decay experiment the main goal was to determine the α-decay half-lives of neutral ^{213}Fr and ^{214}Ra atoms. The selected fragments separated by the FRS reached the final focal plane at energies in the range of 500 to 600 MeV/u. In order to measure their decay half-lives, the selected nuclei were implanted into a position-sensitive Si detector. The measured weighted mean value of the half-life for ^{213}Fr in this experiment was 34.03 ± 0.27 s and for

^{214}Ra 2.441±0.021 s. The experiment with ^{213}Fr under completely different conditions to be sensitive to unknown systematic errors. The result of the Catania experiment was $T_{1/2} = 34.126 \pm 0.056$ s, which is in excellent agreement with the GSI experiment.

In the second part of the α-decay study a pilot experiment has been launched for a feasibility study. H-like ^{213}Fr ions have been separated in-flight with the FRS and subsequently injected ESR. The decay of the H-like ^{213}Fr ions was measured by applying Schottky Mass Spectrometry. The results from our experiments with neutral and H-like ^{213}Fr clearly demonstrate that both half-lives are in excellent agreement within the error bars. This fact is a strong experimental evidence against the previous results of the theoretical paper from Erma [Erm57] which predicts a difference of the half-lives of the about of 40%. According to a more realistic model [Pat08] we expect for neutral and H-like ^{213}Fr a difference in the 0.35 % range. For a more conclusive experimental contribution in this expected much smaller difference we plan future experiments with the FRS-ESR facility with much higher statistics.

Bibliography

[Ald71] K. Alder *et al.*, Phys. Lett. A **34**, 163 (1971).

[Arm04] P. Armbruster *et al.*, Phys. Rev. Lett. **93**, 212701 (2004).

[Ass87] H.J. Assembaum *et al.*, Z. Phys. A **327**, 461 (1987).

[Bar02] F. C. Barker, Nuclear Physics A **707**, 277(2002).

[Bas07] M.S. Basunia, Nucl. Data Sheets **108**, 633 (2007).

[Bem73] C.E. Bemis *et al.*, Phys. Lett. **31**, 647 (1973).

[Ber03] M. Bernas *et al.*, Nuclear Physics A **725**, 213 (2003).

[Ber06] M. Bernas *et al.*, Nuclear Physics A **765**, 197 (2006).

[Bet32] H. Bethe, Z. Phys. **76**, 293 (1932).

[Bic11] http://www.detectors.saint-gobain.com/document.aspx?docId=201922.

[Bos06] F. Bosch *et al.*, Int. J. Mass Spectrom. **251**, 212 (2006).

[Bro03] E. Browne, Nucl. Data Sheets **99**, 649 (2003).

[Bro05] E. Browne, Nucl. Data Sheets **104**, 427 (2005).

[Che10] L. Chen *et al.*, Phys. Lett. B **691**, 234 (2010).

[Cow06] J.J. Cowan and C. Sneden, Nature **440**, 1151 (2006).

[Enge95] C. Engelmann *et al.*, Z. Phys. A **352**, 351 (1995).

[Engs80] S. Engstler *et al.*, Phys. Lett. B **202**, 179 (1980).

[ENSDF] ENSDF database, http://www.nndc.bnl.gov/ensdf/ .

[Erm57] A. Erma, Phys. Rev. **105**, 1784 (1957).

[Far10] F. Farinon, *ITAG Manual (2010)*,
http://www-w2k.gsi.de/frs/technical/FRSsetup/detectors/itag.asp.

[Fol91] H. Folger *et al.*, Nucl. Instr. and Meth. A **303**, 24 (1991).

[Fra08] B. Franzkle *et al.*, Mass Spectrom. Rev. **27**, 428 (2008).

[Fra87] B Franzke, Nucl. Instr. and Meth. B **24**, 18 (1987).

[FRS11] http://www-wnt.gsi.de/frs/technical/FRSsetup/detectors/sci.asp.

[Gai91] J.-J Gaimard and K.-H Schmidt, Nucl. Phys. A **531**, 709 (1991).
[Gei02] H. Geissel *et al.*, Nucl. Instr. and Meth. B **195**, 3 (2002).
[Gei92] H. Geissel *et al.*, Nucl. Instr. and Meth. B **70**, 286 (1992).
[Gei92b] H. Geissel *et al.*, Phys. Rev. Lett. **68**, 3412 (1992).
[Gei97] H. Geissel, Nucl. Phys. A **616**, 316 (1997).
[Gol74] A.S. Goldhaber, Phys. Lett. B **53**, 306 (1974).
[Hin10] C.B. Hinke, *Spectroscopy of the doubly magic nucleus* ^{100}*Sn and its decay*, PhD. Thesis, Technische Universität, München, 2010.
[Hof00] S. Hofmann and G. Münzenberg, Rev Mod. Phys. **72**, 733 (2000).
[Hor91] P. Hornshoj *et al.*, Nucl. Phys. A **230**, 380 (1974).
[Irn96] H. Irnich *et al.*, Phys. Rev. Lett. **75**, 4182 (1996).
[Iwa97] N. Iwasa *et al.*, Nucl. Instr. and Meth. B **126**, 284 (1997).
[Jan11] R. Janik *et al.*, Nucl. Instr. and Meth. A **640**, 54 (2011).
[Koj08] I. Kojouharov *et al.*, GSI Scientific Report 2008, 235 (2008).
[Kum09] R. Kumar *et al.*, Nucl. Instr. and Meth. A **598**, 754 (2009).
[Kur06] H. Alvarez-Pol *et al.*, arXiv nucl-ex/1007.5506, (Jul 2010).
[Kur06] T. Kurtukian-Nieto *et al.*, Proceedings of the *IX Int. Symposium on Nuclear Astrophysics - Nuclei in the Cosmos*, PoS(NIC-IX)008 (2006).
[Lin96] J. Lindhard and A.H Soerensen, Phys. Rev. A **53**, 2443 (1996).
[Lit05] Yu.A. Litvinov *et al.*, Nucl. Phys. A **756**, 3 (2005).
[Lit07] Yu.A. Litvinov *et al.*, Phys. Rev. Lett. **99**, 2650 (2007).
[Lit10] Yu.A. Litvinov and F. Bosch, Rep. Prog. Phys. **73** (2010).
[Lob68] Y.V. Lobanov and V.A. Durin, Yadern Fiz. **8**, 849 (1968);
[Mar93] M.J. Martin, Nucl. Data Sheets **70**, 315 (1993).
[Mes11] http://www.mesytec.com
[Mic11] http://www.microsemiconductor.co.uk.
[Mor89] D.J. Morrisey, Phys. Rev. C **39**, 460 (1989).
[Mus06] A. Musumarra *et al.*, E073 experiment proposal, www.gsi.de/forschung/kp/kr/nuc-astro/E073_Musumarra.pdf .
[Mus11] A. Musumarra *et al.*, C073 experiment proposal.
[Nol04] F. Nolden *et al.*, Nucl. Instr. and Meth. A **532**, 329 (2004).
[Nol11] F. Nolden *et al.*, Nucl. Instr. and Meth. A in press.
[Ohn10] T. Ohnishi *et al.*, Journal of the Physical Society of Japan **79**, 201 (2010).

[Ort11] ORTEC, http://www.ortec-online.com.
[Pat08] Z. Patyk *et al.*, Phys. Rev. C **78**, 054317 (2008).
[Per93] D.B. Percival and A. D. Walden, *Spectral Analysis for Physical Applications*, Cambridge University Press, 1993.
[Pfü94] M. Pfüzner *et al.*, Nucl. Instr. and Meth. A **493**, 155 (2002).
[Pie07] S. Pietri *et al.*, Nucl. Instr. and Meth. B **261**, 1079 (2007).
[Pro11] A. Prochazka, *Nuclear Structure Studies Via Precise Momentum Measurements*, PhD. Thesis, Justus-Liebig Universität, Gießen 2011.
[ROOT] http://root.cern.ch/. CERN.
[Rot90] H. Rothard *et al.*, Phys. Rev. A **41**, 2521 (1990).
[Rub72] W. Rubinson and M. L. Perlman, Phys. Lett. B **40**, 352 (1972).
[San11] S. Sanjani, PhD. Thesis, J.W. Goethe Universität, Frankfurt, in preparation.
[Sch94] C. Scheidenberger *et al.*, Phys. Rev. Lett. **73**, 50 (1994).
[Sch96] C. Scheidenberger *et al.*, Phys. Rev. Lett. **77**, 3987 (1996).
[Sch98] C. Scheidenberger *et al.*, Nucl. Instr. and Meth. B **142**, 441 (1998).
[Schl97] B. Schlitt, *Schottky Mass Spectroscopy at the Heavy Ion Storage Ring ESR*, PhD. Thesis, Ruprecht-Karls-Universität, Heidelberg, 1997.
[Schn94] R. Schneider *et al.*, Z. Phys. A **348**, 241 (1994).
[Schn00] R. Schneider and A. Stolz, *Technical Manual Ionization Chamber MUSIC80 (2000)*, http://www-w2k.gsi.de/frs/technical/FRSsetup/detectors/music.asp.
[Ste96] M. Steck *et al.*, Phys. Rev. Lett. **77**, 3803 (1996).
[Ste04] M. Steck *et al.*, Nucl. Instr. and Meth. A **532**, 357 (2004).
[Str01] F. Strieder *et al.*, Naturwissenschaften **88**, 461 (2001).
[Tar11] http://www.gsi.de/informationen/wti/tl/Targetscanner_e.htm .
[Typ11] S. Typel, private comunication 2011.
[Val67] K. Valli *et al.*, Phys. Rev. **161**, 1286 (1967).
[Wei00] H. Weick *et al.*, Nucl. Instr. and Meth. B **164/165**, 168 (2000).
[Wil96] M. Wilhelm *et al.*, Nucl. Instr. and Meth. A **381**, 462 (1996).
[Win09] N. Winckler *et al.*, Phys. Lett. B **679**, 36 (2009).
[Zin06] N.Y. Zinner, arXiv nucl-th/0608049 v1, 21 August 2006.

Acknowledgments

I would like to devote the following few lines to express my warm thanks and gratitude to all those who have accompanied me during my PhD years at GSI.

First of all, Prof. Dr. Dr. h.c. Hans Geissel (Hans for the colleagues) who welcomed me in the FRS group at GSI. I am particularly grateful for his guidance during the writing and correction of this thesis. I have learned a lot (but clearly not enough!) from his precision, accuracy and aim to reach the highest scientific standards. I also thank Prof. Dr. Volker Metag for accepting to be the second evaluator as well as Prof. Dr. Werner Scheid and Prof. Dr. Christoph Scheidenberger for joining the examination committee.

It is a real pleasure to thank my daily supervisor Chiara for the patience, brilliant support and continuous help she provided me during the ITAG setup tests, with the analysis of the Francium experiment and during the many beamtimes. I fully enjoyed the (hopefully mutual) good company of the FRS team for four years and we shared a lot both in human and professional terms. The GSI Think Tank requires a special mention: the combined minds of Jan, Andrej, Ronja, Tanja, Alfredo and (Al)Brano produced many exotic ideas and much fun during lunches and coffee breaks.

I want to thank the many people who greatly contributed to the development of ITAG: Ivan, Stephane, Adolf, Karl-Heinz and Christos. I am grateful for the many interesting discussions on Francium decay with Agatino, MariaGrazia, Maria, Yuri and Nicolas. Particular thanks (and a deserved crate of Champagne!) to Zygmunt for the fastest calculation of the α-decay constant for H-like ^{213}Fr ions!

Marco and Prof. Dr. Cosimo Signorini set the basis for my permanence here in Germany. They may not know, but they have changed my life in a radical (and positive) way.

Barbara, Martino, Gianluigi, Giancarlo, Victor, Julio and the Gast Barracks have been real good friends and helped me surviving the first few months here; then I met Giovanna...my family :-)

My deepest thanks are dedicated to my wife: there are not enough words to express my gratitude and love (so I don't even try!). A tender welcome and a cuddle to the small Niccoló, who enjoys waking me up in the middle of the night. The same deepest thanks are devoted to my parents and my brother who have always supported and accompanied me, and they are still doing it.

Versicherung

Ich erkläre: Ich habe die vorgelegte Dissertation selbständig und ohne unerlaubte fremde Hilfe und nur mit den Hilfen angefertigt, die ich in der Dissertation angegeben habe. Alle Textstellen, die wörtlich oder sinngemäß aus veröffentlichten Schriften entnommen sind, und alle Angaben, die auf mündlichen Auskunften beruhen, sind als solche kenntlich gemacht. Bei den von mir durchgeführten und in der Dissertation erwähnten Untersuchungen habe ich die Grundsätze guter wissenschaftlicher Praxis, wie sie in der "Satzung der Justus-Liebig-Universität Gießen zur Sicherung guter wissenschaftlicher Praxis" niedergelegt sind, eingehalten.

Gießen, XXVIII Oktober, 2011

Fabio Farinon